

THESIS FOR THE DEGREE OF DOCTOR OF PHILOSOPHY

Towards Electrolyte free Li-ion Battery Waste

Utilizing supercritical CO₂ extraction and thermal treatment for electrolyte recycling

NILS ZACHMANN

Department of Chemistry and Chemical Engineering

CHALMERS UNIVERSITY OF TECHNOLOGY

Gothenburg, Sweden 2025

Towards Electrolyte free Li-ion battery waste
Utilizing supercritical CO₂ extraction and thermal treatment for electrolyte recycling
NILS ZACHMANN
ISBN 978-91-8103-205-5

Acknowledgements, dedications, and similar personal statements in this thesis, reflect the author's own views.

© NILS ZACHMANN, 2025.

Doktorsavhandlingar vid Chalmers tekniska högskola
Ny serie nr 5663
ISSN 0346-718X

Department of Chemistry and Chemical Engineering
Chalmers University of Technology
SE-412 96 Gothenburg, Sweden
Telephone + 46 (0)31-772 1000

Cover: Illustration of the supercritical carbon dioxide extraction process to recycle electrolyte from spent Li-ion batteries.

Printed by:
Chalmers Digitaltryck
Gothenburg, Sweden 2025

Towards Electrolyte free Li-ion Battery Waste

Utilizing supercritical CO₂ and thermal treatment for electrolyte recycling

NILS ZACHMANN

Industrial Materials Recycling
Department of Chemistry and Chemical Engineering
Chalmers University of Technology

Abstract

A significant challenge in the current recycling of batteries is the effective removal of electrolyte from e.g. Li-ion battery waste. Li-ion battery waste containing residual electrolyte is classified as hazardous waste, posing a financial burden for the recycling industry.

The aim of this work was to investigate potential options and finally suggest a favourable method to recover the electrolyte from spent Li-ion battery waste. The thesis is divided into three parts. In the first part, two promising approaches for the electrolyte separation from spent Li-ion battery pouch cells were investigated: low temperature thermal treatment and supercritical CO₂ extraction. The results showed that low temperature thermal treatment at 130°C under N₂ atmosphere is suitable for the separation of the electrolyte solvents dimethyl carbonate, ethyl methyl carbonate, and ethylene carbonate. However, lithium hexafluorophosphate decomposed while releasing toxic gases hydrogen fluoride and phosphorous oxyfluoride. Using supercritical CO₂ extraction, the non-polar electrolyte solvents dimethyl carbonate and ethyl methyl carbonate were successfully extracted at 80 bar and 29°C, whereas the polar electrolyte solvent ethylene carbonate was only extracted in trace amounts. Analysis of the exhaust gas emissions and elemental analysis of the extract indicated that lithium hexafluorophosphate did not decompose during the process.

In the second part of the thesis, the solubility of ethylene carbonate in supercritical CO₂ was studied. The solubility of ethylene carbonate increased with increasing pressure from 80 bar to 140 bar at 40°C from 0.24 to 8.35 g/kg CO₂. In the third part, the previously obtained solubility results were applied to extract the remaining electrolyte in the LiB black mass. The volatile electrolyte components dimethyl carbonate, ethyl methyl carbonate, and diethyl carbonate were successfully extracted with an extraction yield exceeding 99% using 100 bar and 40°C. Raising the pressure to 140 bar led to high extraction yields of biphenyl, ethyl carbonate, and propylene carbonate with 98%, 95%, and 98%, respectively. The extraction curves of ethylene carbonate, propylene carbonate, and biphenyl indicated that the non-polar solvents dimethyl carbonate, ethyl methyl carbonate, and diethyl carbonate behaved as an entrainer for their extraction at 100 bar. An entrainer effect at 140 bar was not observed. The extraction rates of biphenyl, ethylene carbonate, and propylene carbonate at 140 bar and 40°C were determined to be 0.18 mg/g CO₂, 1.9 mg/g CO₂ and, 0.4 mg/g CO₂, respectively. The extraction of lithium hexafluorophosphate remained below 5%. The results of this thesis showcase the potential to utilize scCO₂ extraction to separate the electrolyte from Li-ion battery waste. This is a step forward into a safer battery recycling process.

Keywords: Li-ion battery; electrolyte; recycling; supercritical CO₂ extraction, thermal treatment

This thesis is based on the work contained in the following papers and manuscripts referred to by Roman numerals in the text:

Paper I

N. Zachmann, M. Petranikova, B. Ebin, Electrolyte recovery from spent Lithium-Ion batteries using a low temperature thermal treatment process, *J. Ind. Eng. Chem.* (2022). DOI: [10.1016/j.jiec.2022.11.020](https://doi.org/10.1016/j.jiec.2022.11.020)

Contribution: Main author, all experimental work and data analysis.

Paper II

N. Zachmann, Robert V. Fox, M. Petranikova, B. Ebin, Implementation of a sub-and supercritical carbon dioxide process for the selective recycling of the electrolyte from spent Li-ion battery, *Journal of CO₂ Utilization* (2024). DOI: [10.1016/j.jcou.2024.102703](https://doi.org/10.1016/j.jcou.2024.102703)

Contribution: Main author, all experimental work and data analysis.

Paper III

N. Zachmann, C. Cicconardi, , B. Ebin, Exploring the solubility of ethylene carbonate in supercritical carbon dioxide: A pathway for sustainable electrolyte recycling from Li-ion batteries, *Batteries* (2025), DOI: [10.3390/batteries11030098](https://doi.org/10.3390/batteries11030098)

Contribution: Main author, main experimental work and data analysis.

Paper IV

N. Zachmann, M. Petranikova, B. Ebin, Supercritical CO₂ extraction behaviour of electorlyte solvents from Li-ion battery black mass, (Manuscript)

Contribution: Main author, all experimental work and data analysis.

Abbreviations and Definitions.

The following abbreviations and definitions are used throughout this thesis.

Abbreviations.	Definition
ATR	Attenuated total reflection
CO ₂	Carbon dioxide
DEC	Diethyl carbonate
DMC	Dimethyl carbonate
DMFP	Dimethyl fluorophosphate
DTG	Differential thermogravimetric
EC	Ethylene carbonate
EMC	Ethyl methyl carbonate
EMFP	Ethyl methyl fluorophosphate
FEC	Fluoroethylene carbonate
FTIR	Fourier-transform infrared spectroscopy
GC-MS	Gas chromatography coupled with mass spectroscopy
GWh	Gigawatt-hours
HF	Hydrofluoric acid
HNO ₃	Nitric acid
IC	Ion chromatography
ICP-OES	Inductively coupled plasma optical emission spectroscopy
LA	Lewis acid
LB	Lewis base
LiB	Lithium-ion battery
Lif	Lithium Fluoride
LiPF ₆	Lithium hexafluorophosphate
LVE	Liquid-vapor equilibrium
NMC	Lithium Nickel Manganese Cobalt Oxide
PC	Propylene carbonate
PF ₅	Phosphorous pentafluoride
POF ₃	Phosphorous oxyfluoride
scCO ₂	Supercritical carbon dioxide
TG	Thermogravimetric
TGA	Thermogravimetric analysis
VC	Vinylene carbonate
wt%	Weight percent
XRD	X-ray diffraction

Table of Contents

1. Introduction.....	1
2. Background	3
2.1. EU Directive for batteries and waste batteries.....	3
2.2. Lithium-ion battery components and their composition.....	3
2.3. State-of-the-art LiB recycling strategies	7
2.4. The challenge in the recycling of (non-aqueous) electrolyte	7
2.5. Processes to recycle the electrolyte from spent LiBs.....	8
3. Theory	13
3.1. Solvation characteristics of supercritical carbon dioxide.....	13
3.2. Chrastil model	14
3.3. Modelling of scCO₂ extraction curves.....	14
3.4. LiPF₆ decomposition	18
3.5. Formation of inorganic phosphates by hydrolysis of POF₃.....	18
4. Experimental	19
4.1. Materials and Chemicals	19
4.2. Electrolyte recovery from untreated LiB cells using thermal treatment and scCO₂ extraction	19
4.2.1. Sample preparation	19
4.2.2. Characterization of the electrolyte composition.....	19
4.2.3. Low temperature thermal treatment process.....	20
4.2.4. Sub- and scCO₂ extraction process.....	22
4.3. Solubility of ethylene carbonate in scCO₂.....	23
4.4. ScCO₂ extraction behavior of electrolyte solvents from LiB black mass	23
4.5. Formula and calculation protocols.....	24
4.6. Analytical methods.....	25
5. Results	29
5.1. Electrolyte recovery from untreated LiB cells using thermal treatment and scCO₂ extraction	29
5.1.2. Low temperature thermal treatment	30
5.1.3. Sub-and sc-CO₂ extraction.....	37
5.2. Solubility of ethylene carbonate in scCO₂.....	42
5.3. ScCO₂ extraction behavior of electrolyte solvents from LiB black mass	45
6. Discussion.....	53

6.1. Electrolyte recovery from untreated LiB cells using thermal treatment and scCO₂ extraction	53
6.2. Solubility of ethylene carbonate in scCO₂.....	56
6.3. ScCO₂ extraction behavior of electrolyte solvents from LiB black mass.....	56
7. Conclusion	59
Future Work.....	61
Acknowledgments	62

1. Introduction

A significant milestone in battery technology was marked in 1991 with the release of the first commercially available rechargeable Li-ion battery (LiB) by Sony and Asahi Kasei. Their combination of high energy density, and relatively long lifespan, was crucial in enabling the development of portable electronic devices, electric vehicles, and large-scale energy storage systems [1,2].

The demand for LiBs grew rapidly in the last years, which was particularly driven by the transition of the automotive industry towards electrically powered transportation. To keep up with the demand, the battery manufacturing has reached a capacity of 2500 gigawatt-hours (GWh) in 2023, which is an increase of 25% compared to 2022. In 2030, the total global battery manufacturing capacity is estimated to exceed 9000 GWh [3]. To translate this, 1 GWh corresponds to approximately 5000 tons of materials considering a pack-level density of 200 Wh/kg. As the LiB demand for EVs and portable electronics continues to grow, the expected accumulation of spent LiBs necessitates comprehensive waste management and recycling solutions.

Developing proper recycling processes for spent LiBs is critical for several reasons. Firstly, LiBs are classified as hazardous waste due to their content of a variety of hazardous elements [4,5]. Improper disposal of spent LiBs can lead to significant environmental damage, including contamination of the ground water and soil. In the unfortunate event of a fire, toxic gases will be released into the environment [6–9]. Secondly, recycling is an important source of raw materials as the reserves for LiB materials are finite. In example, lithium, cobalt, natural graphite and phosphorous are listed as critical raw materials meaning their demand is forecast to overtake the supply in the near future [10]. Furthermore, the EU is highly dependent on its geopolitical relations for the supply of LiB raw materials as they are mined and produced outside of Europe, in countries such as DR Congo, China, Chile, Russia, South Africa, and Australia [11]. Lastly and most importantly, recycling of spent LiBs is mandatory on the EU level. According to the newest regulation, 70% of the LiB by average weight must be recycled from 2030 onwards [12].

The recovery of the electrolyte from spent LiBs remains a major challenge in the state-of-the-art recycling process. Due to the volatile nature of the electrolyte solvents and the thermal instability of the conductive salt, lithium hexafluorophosphate (LiPF_6), the electrolyte is prone to evaporate and decompose resulting in hazardous gas emissions [13–15]. A concentrated toxic atmosphere can be quickly formed under the release of small amounts of electrolyte which becomes a serious threat for the work safety in recycling plants as irreversible health effects are very likely [5]. Literature suggests vacuum distillation, thermal treatment, organic solvent extraction or supercritical carbon dioxide (scCO₂) extraction as promising approaches for the recovery of electrolyte from spent LiBs [16–18]. However, extended research on these approaches is still limited.

The aim of the thesis was to investigate possible options and finally suggest a favorable method to recycle the electrolyte from Li-ion battery waste. Therefore, two approaches - low temperature thermal treatment and scCO₂ extraction - were selected and tested on spent LiB pouch cells (Paper I and Paper II). Then, the most promising approach was studied in more detail (Paper III). Finally, the approach was tested further on Li-ion battery black mass (Paper IV).

2. Background

2.1. EU Directive for batteries and waste batteries

Batteries and waste batteries have been regulated at EU level under the Batteries Directive (2006/66/EC) since 2006 [19]. Directive 2006/66/EC was replaced by a new regulation in August 2023 in order to introduce comprehensive requirements covering the entire lifecycle of batteries, from production to reuse and recycling [12]. Among other measures in the design and production of batteries in terms of safety, carbon footprint, restriction of substances, performance and durability, targets and requirements for recycling efficiency, material recovery and recycled content will be phased in gradually.

The collection target for spent portable batteries will increase from 63% in 2027 to 73% in 2030 and for light means of transport batteries will increase from 51% by 2028 to 61% by 2031. Specific targets were not set for starting, lightning and ignition batteries, industrial batteries and electric vehicle batteries. However, producers are required to ensure separate collection of waste batteries free of charge to the end user. The overall targeted recycling efficiency of LiBs increases from 65% by average weight by 2025 to 70% by average weight in 2030. The targets for the recovery of materials are Co (95%), Ni (95%), Li (80%) and Cu (95%) by the end of 2031. Requirements concerning the treatment of spent batteries include, as a minimum, the removal of all fluids and acids.

2.2. Lithium-ion battery components and their composition

Electrically powered battery systems consist of multiple components. The heart of these systems are battery packs, which are composed of a set number of modules along with various control and protection systems. Each battery module, in turn, contains a fixed number of LiB cells, which are electrically connected and housed within a frame along with different battery management electronics. The LiB cell itself, the fundamental unit of this battery systems, come in four distinct shapes; cylindrical, prismatic, pouch, and coin [20–22]. Regardless of their different shapes, all LiB cells share a common structure comprising five key components; cathode (20-35 wt%), separator (4-10 wt%), anode (15-25 wt%), electrolyte (10-20 wt%), and casing (4-20 wt%) [20,23].

The manufacturing process of LiB cells involves layering the cathode, separator, and anode materials to form what is termed the electrode stack or jelly roll. A close-up version of one LiB cell layer is illustrated in Figure 1. The electrode stack/jelly roll is then inserted into a protective casing or shell. The final step involves injecting the non-aqueous liquid electrolyte into the assembly and hermetically sealing the case [21].

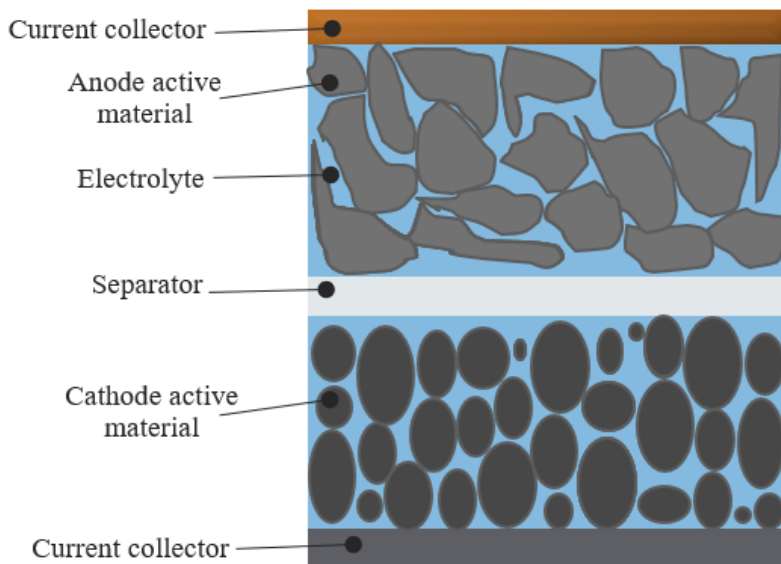


Figure 1. Illustration of one layer consisting of anode, separator, and cathode of a LiB battery cell.

2.2.1. Cathode

The cathode, or positive electrode, consists of a current collector, active cathode material and a binder. The polymeric binder adheres the active cathode material to the current collector. A variety of active cathode materials, with different chemical compositions, are commercially available, and new formulations continue to emerge. The most widely used active cathode chemistries are based on various transition metals and are the name-giver of the LiB cell. These include Lithium Nickel Cobalt Manganese Oxide (NMC), Lithium Iron Phosphate (LFP), Lithium Nickel Manganese Spinel (LMNO), Lithium Nickel Cobalt Aluminum Oxide (NCA), Lithium Manganese Oxide (LMO), and Lithium Cobalt Oxide (LCO). Thin aluminum foils are typically employed as the current collector material while the state-of-the-art polymeric binder material is polyvinylidene fluoride (PVDF) [1,20–22].

2.2.2. Anode

The anode, or negative electrode, consists of a current collector (typically thin copper foil), the active anode material, and a binder. The most used active material is high-grade graphite, although lithium titanium oxide ($\text{Li}_4\text{Ti}_5\text{O}_{12}$) is also used. The binder materials typically used in anodes include carboxymethyl cellulose (CMC), styrene butadiene rubber (SBR), and PVDF [1,20,22].

2.2.3. Separator

The separator prevents direct contact between the anode and the cathode while still allowing high permeability to the conductive salt. Separators are primarily made from polyolefins, such as polypropylene (PP) and polyethylene (PE). In some cases, the separator membrane can be ceramic or PVDF [24].

2.2.4. Electrolyte

The electrolyte facilitates the ion transfer between the anode and cathode during the charging and discharging process [25]. In general, there are three main types of LiB electrolytes, i.e., liquid, polymer and solid electrolytes, and several different electrolyte chemistries have been developed [26]. As battery chemistries evolve, so will new electrolyte formulations [27].

The most widely used electrolyte is the non-aqueous liquid electrolyte, which is a multi-component system composed of a Li-salt dissociated in a mixture of organic solvents and additives [28]. The exact composition and quantity of the electrolyte in the LiB cell can vary across manufacturers and is often unspecified. Typically, the electrolyte makes up about 10-20% of the total cell weight [20,23]. The electrolyte solvent usually constitutes the largest proportion of the electrolyte solution with 80 to 90%, whereas the additives typically account for up to 5%, and the Li-salt about 10% [29].

The most used Li-salt is LiPF₆ not because of any outstanding property but rather due to the lack of any significant disadvantage [28]. However, other Li-salts such as sulfonylimides (LiTFSI, LiFSI, LiBETI), borates (LiBF₄, LiBOB, LiDFOB), or lithium perchlorate (LiClO₄) are potential replacements [28,29].

A mixture of different carbonate esters such as ethylene carbonate (EC), propylene carbonate (PC), dimethyl carbonate (DMC), ethylene carbonate (EMC), and diethyl carbonate (DEC) are commonly used as electrolyte solvents. Attributed to its high-dielectric nature, EC is effective in dissociation of the Li-salt and enables the formation of a stable protective layer on the cathode interphase. To improve EC's high viscosity (as it is solid at room temperature) it is mixed with the linear, non-polar DMC, EMC, and/or DEC [25,26,28,29]. Various additives can be added to the electrolyte solvent mixture to address specific challenges, such as improving of the flammability resistance, enabling overcharge protection, enhancement of conductivity, and optimizing the performance of the battery [26,29]. Common additives include vinyl carbonate (VC), fluoroethylene carbonate (FEC), biphenyl, or tris(trimethylsilyl)phosphite (TMSPi) [30]. A detailed overview of the key components in the state-of-the-art non-aqueous electrolytes solution including their chemical and physical properties as well as hazard identification according to Classification, Labelling and Packaging Regulation (Regulation (EC) No. 1272/2008) can be found in Table 1 [5,28,31].

Table 1. Summary of the key components in non-aqueous electrolyte solutions including their structure, melting point (T_m), boiling point (T_b), vapor pressure (p_v), dielectric constant (ϵ), dipole moment, and hazard identification.

Compound	Structure	T_m [°C]	T_b [°C]	p_v^a [mmHg]	ϵ [25°C]	Dipole Moment [D]	Hazard
Dimethyl Carbonate (DMC)		4	90	55.36	3.1	0.76	
Ethyl Methyl Carbonate (EMC)		-55	110	32	2.9	0.89	
Diethyl Carbonate (DEC)		-74	129	11.5	2.8	0.97	
Ethylene Carbonate (EC)		36.5	248	0.0098	89.8	4.61	
Propylene Carbonate (PC)		-49	242	0.045	64.9	4.81	
Lithium Hexafluorophosphate (LiPF₆)		N/A	N/A	N/A	N/A	N/A	

^a Vapor pressure at 25°C. The vapor pressure of water is 23.8 mmHg at 25°C.

2.2.5. Case

The hermetically sealed case safeguards the electrode stack/jelly roll from external elements. The material used for the case depends on the shape of the LiB cell and can include metal foil, steel, aluminum or plastic.

2.3. State-of-the-art LiB recycling strategies

The state-of-the-art LiB recycling strategies employs two main approaches: pyrometallurgy, and hydrometallurgy [18,21,32].

The pyrometallurgy approach involves high temperature processing of entire (discharged) LiB cells or modules. A metallic alloy containing Co, Cu, Fe and Ni is formed during this process, which is then chemically processed to separate individual metals. Toxic and environmentally harmful gases such as HF are formed while the separator, binder material, electrolyte and graphite evaporates, decomposes, or gets burnt off [18,21]. The resulting slag contains Al, Mn, and Li, which are challenging to be individually separated using hydrometallurgical processes. Instead, the slag is often sold to other industries.

The hydrometallurgy process begins with a pre-treatment phase. LiB batteries are discharged, dismantled, sorted, crushed, shredded, and separated into a black mass containing a mixture of cathode and anode material. The black mass undergoes leaching, solvent extraction, ion exchange, and other processes to recover the valuable metals like Li, Mn, Ni, Al, and Co. Some recycling processes include thermal treatment to remove the electrolyte/ and or binder to prepare the black mass for the hydrometallurgy process by deactivating, liberating and reducing the active materials [4,18,21]. The pre-treatment processes are conducted in an inert atmosphere like N₂ to stabilize volatile electrolyte components by preventing reactions with air and moisture.

Both methods have their advantages and disadvantages. Pyrometallurgy is simpler but less selective, requires high energy input and requires additional treatment of the generated off-gases. Hydrometallurgy offers better recovery rates for specific metals but requires complex pre-treatment processes to achieve high recovery yields. Thus, many current recycling strategies use hydrometallurgy to maximise the material recovery yield while minimizing the environmental impact.

2.4. The challenge in the recycling of (non-aqueous) electrolyte

The electrolyte in spent LiBs poses significant challenges for the recycling industry and contributes to considerable safety concerns of the overall recycling process. The non-aqueous electrolyte solvents in use today are (very) volatile, hazardous and flammable [6]. When a battery cell is opened, these solvents can evaporate almost instantly owing to their high vapor pressure [33]. Small releases of electrolyte solvents can quickly create a concentrated toxic atmosphere that exceeds acute exposure limits – below 250ml in a room of 62m³ – leading to serious irreversible health risks [5]. Additionally, the flammable nature of these solvents increase the risk of fire or explosions in the recycling plants [34]. Thus, improper handling and treatment of LiB waste can have severe impact for both the work environment in the recycling plants and the broader environment.

Another significant challenge is the thermal instability and moisture sensitivity of LiPF₆. It is prone to decompose into highly toxic substances such as hydrogen fluoride (HF), phosphorus pentafluoride (PF₅), and phosphorous oxyfluoride (POF₃) [4,5,15,35–40]. These decomposition products not only represent major safety concerns but also react with electrolyte solvents to form various aging products throughout the LiB cycling life, or potentially in the electrolyte recycling process [17,41–44]. Thus, aged LiBs may contain a variety of

organophosphate-based and organic fluorophosphate-based products including dimethyl phosphorofluoridate (DMFP), ethyl methyl phosphorofluoridate (EMFP) and diethyl phosphorofluoridate (DEFP). PF₅ is known to facilitate transesterification involving electrolyte solvents. For example, it can lead to the formation of DMC and DEC from EMC. As a result of these chemical interactions and complex decomposition products, reclaimed electrolyte require purification before their reutilization [44].

Last but not least the composition and total amount of the electrolyte used in the battery production are often unknown, inhomogeneous, and can vary from producer to producer which adds a layer of complexity into the recycling process [16,27].

From an environmental perspective, the safe removal of electrolytes is crucial. Proper management of the electrolyte can significantly reduce the greenhouse gas emissions associated with its incineration and minimize the threats related to LiB waste. Moreover, it enhances the safety of the overall recycling process [44].

2.5. Processes to recycle the electrolyte from spent LiBs

A few research groups have proposed different approaches to recover the electrolyte from spent LiBs. The most promising techniques are vaporization processes, organic solvent extraction and supercritical fluid extraction [9,16,17,45,46].

2.5.1. Vaporization processes

Vaporization is a process in which a substance changes its physical state from a liquid or solid phase into a vapor phase. The transition requires sufficient kinetic energy to overcome the substances' internal molecular forces. The amount of energy/temperature required to initiate the vaporization is determined by the boiling point of the substance. The boiling point itself correlates with the external pressure. The boiling point decreases at lower external pressures. When the substance vaporizes below its boiling point, it is referred to as evaporation. The rate of evaporation depends on several factors such as the substance's vapor pressure and ambient temperature. Higher vapor pressure and temperature at constant external pressure lead to faster evaporation.

The concept of thermal vaporization has found practical applications in recycling electrolyte from spent LiB. Zhong et al. [45] demonstrated low temperature volatilization at 120°C to recycle the electrolyte, though they did not specify the composition of the recovered electrolyte or analysis of the exhaust gas emission. Stehmann et al. [47] used a vaporization process to thermally dry shredded LiBs at low pressure (<300mbar) to recover the electrolyte. The recycling company Duesenfeld has also reported the electrolyte removal from spent LiBs using vacuum vaporization [48]. Xu et al. [49] applied vacuum distillation at 130°C to recover the volatile electrolyte solvents DMC, and DEC, followed by precipitation with sodium carbonate to recover Li as lithium carbonate.

2.5.2. Organic solvent extraction

In the organic solvent extraction method, the LiB waste is immersed into an organic extraction solvent to dissolve the electrolyte. The electrolyte is then separated from the solvent using distillation processes based on the different boiling points of the electrolyte components [50]. He et al. [51] achieved an electrolyte extraction yield of 95.6% (PC, EC, LiPF₆) of cathode, anode, and separator material using a custom-made aqueous peeling agent. During the extraction process, LiPF₆ was converted into NaPF₆ and Li-salt. Zhu et al. [52] completely dissolved the electrolyte from electrodes in a DMC solution over 24 hours, followed up with further processing to convert LiPF₆ to calcium fluoride (CaF₂). Haas et al. [53] utilized a combination of DMC and H₂O in a multi-stage, cross-flow extraction system to successfully reduce the fluoride content in lab-scale experiments while extracting EC, DMC, and EMC from black mass. Shi et al. [54] used DMC to extract the electrolyte from electrodes, followed by vacuum distillation to recover the extractant, and water leaching to separate the electrolyte solvents from LiPF₆ in a form of LiF, CaF₂, and Ca₃(PO₄)₂. Du et al. [55] developed a method using DMC as the extraction solvent, and water leaching to extract the remaining LiPF₆ in form of stable metal fluoride and phosphate.

2.5.3. Supercritical fluid extraction

Supercritical fluid extraction is a technique which uses a supercritical fluid as the primary solvent to extract compounds from a material. A substance enters the supercritical state when its pressure and temperature exceed critical values, as illustrated in Figure 2. CO₂ has garnered particular interest due to its non-toxic, non-flammable nature, abundance, low cost, and recyclability. Supercritical CO₂ (scCO₂) can be easily achieved under mild conditions with a critical temperature (T_c) of 31°C and critical pressure (P_c) of 73.8 bar [56,57].

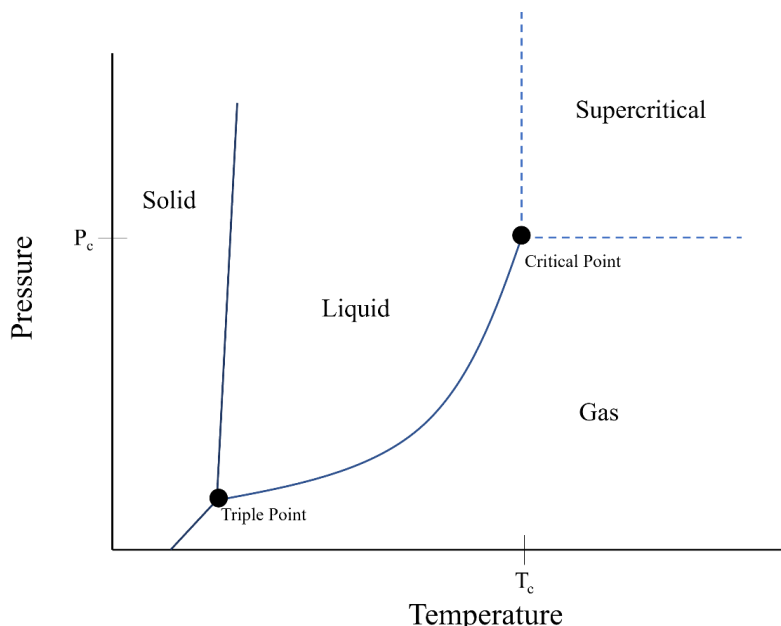


Figure 2. Illustration of the pressure-temperature phase diagram of CO₂.

In the supercritical state, CO₂ exhibits enhanced physicochemical properties, such as liquid-like density, gas-like compressibility, low viscosity, high diffusion coefficient, and negligible surface tension [58]. These properties can be finely adjusted by varying temperature and pressure conditions. Due to its excellent mass transfer characteristics, scCO₂ extraction offers several advantages over to the use of conventional extraction processes which often depend on toxic, flammable, hazardous and environmentally damaging solvents [56,59,60].

A typical scCO₂ extraction process is illustrated in Figure 3. The sample matrix to be extracted is filled in the extraction chamber. Then, scCO₂ is introduced into the chamber where it extracts the desired compound. The extraction process is dependent on the solubility of the solute in CO₂. High solute solubility in CO₂ is essential to transfer the solute into the CO₂ phase. The solubility of a solute is dependent on pressure, temperature, and consequently on the density of CO₂ [61]. The scCO₂, now carrying the extracted compound, passes through a pressure release valve into a separator unit. Due to the lower pressure in the separator, the extract separates from the CO₂. Gaseous CO₂ exits the separator, is liquefied, and is then recycled into a CO₂ tank for reuse in a closed-loop system. The extraction process can be carried out either in static or dynamic mode. In dynamic (flow-through) mode, CO₂ flows continuously throughout the extraction process while maintaining pressure and temperature conditions. The dynamic mode is preferred when the solvent and solute reach the equilibrium quickly [60,62]. In static extraction mode, the pressure and the temperature are kept steady, but no flow of CO₂ occurs. After the extraction time, the CO₂ is released from the reactor into the separator unit. Besides the solubility of solute in CO₂, the CO₂ flowrate is another critical factor in the extraction process. The higher the CO₂ flow rate, the faster is the extraction as the amount of solvent passing through the extraction material is increased. However, a too high flow rate may lead to a lower extraction rate. Even though CO₂ can dissolve the solute at the process conditions, the residence time of the CO₂ in the extraction chamber is too short to interact effectively with the material to transport the solutes to the solvent. In industrial processes often several separation units with different pressure conditions are connected to fractionate the extraction products [58]. In lab-scale processes the most common extraction collection techniques are solvent bubbling, collection on a sorbent material or cryogenic trapping [60].

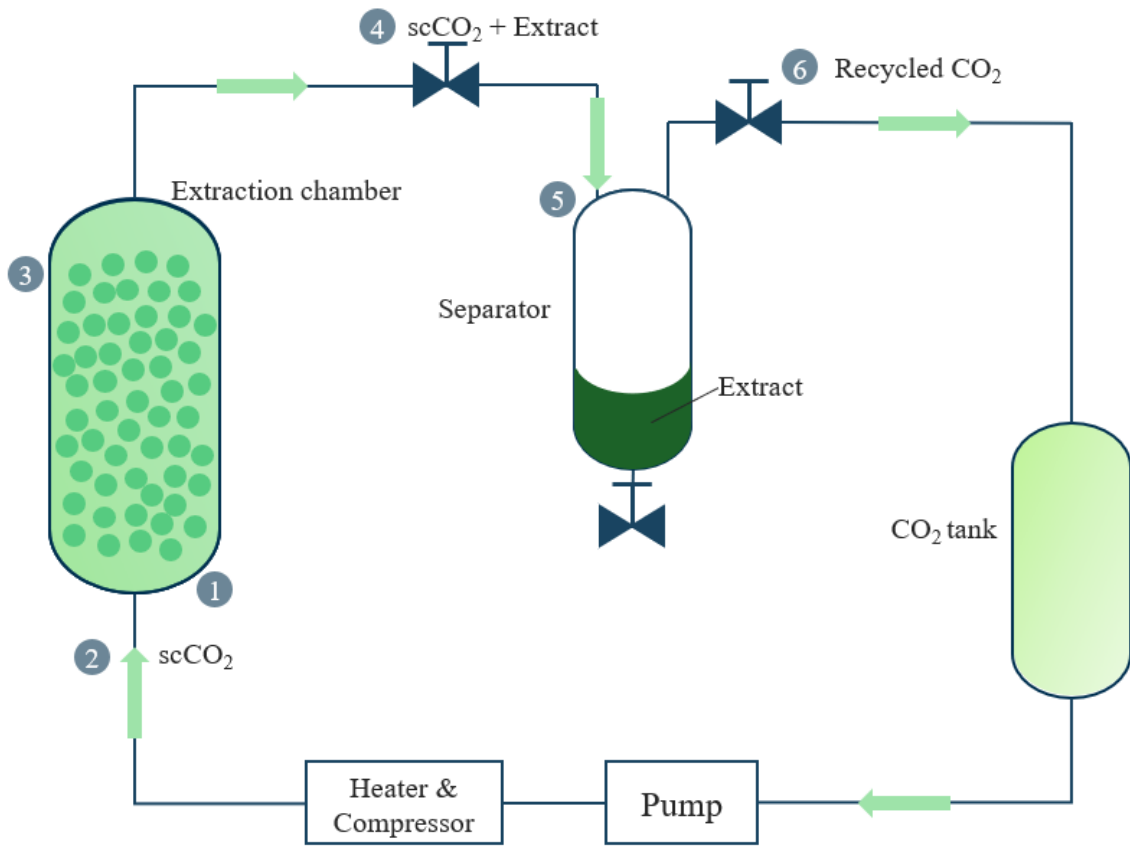


Figure 3. Schematic of a scCO₂ extraction process.

ScCO₂ extraction is employed in the pharmaceutical, cosmetic, dyeing, and food industry [58,63]. Several studies highlighted the potential implementation of sub-and scCO₂ extraction for the recovery of the electrolyte from separator materials and spent 18650 LiBs [42,64–70]. The extraction yields of different electrolyte solvents such as DMC, EMC, DEC, EC, and PC and LiPF₆ are influenced by process variables such as pressure, temperature and extraction mode. A combination of static and flow-through extraction has been found to improve the electrolyte extraction yield [65]. Changes in pressure (varying from 150 to 350 bar) and temperature (30–50 °C) showed a similar extraction trend for non-polar linear carbonates like DMC and EMC, which was attributed to their structural and polarity similarities [67]. Additionally, it was reported that the electrolyte extraction efficiency of spent LiBs nearly doubled when a co-solvent was added, compared to pure liquid (60 bar, 25°C) and supercritical (300 bar, 40°C) CO₂ extraction. In these cases, DMC, EMC were recovered quantitatively, while polar components (EC and LiPF₆) were recovered qualitatively [65].

3. Theory

3.1. Solvation characteristics of supercritical carbon dioxide

The CO₂ molecule is linear and centrosymmetric which results in a zero net dipole moment. As a result, scCO₂ is generally classified as a non-dipolar solvent, making it effective for dissolving many non-polar low-molecular-weight compounds. While CO₂ lacks a permanent dipole moment, it possesses a significant quadrupole moment generated by its bond dipoles. It is well-established that CO₂ can function as both a weak Lewis acid or base and can participate in both conventional and nonconventional hydrogen-bonding interactions [56,59,71]. Research has provided insight into the solvation of esters in scCO₂ at the molecular level and two distinct stable solvation configurations, referred to as Type I and Type II, have been identified [72,73]. In the Type I configuration, the carbonyl oxygen is solvated by the CO₂ molecule, whereby the C atom of the CO₂ molecule functions as a Lewis acid and the carbonyl oxygen as a Lewis base. In the Type II configuration, the CO₂ molecule is in vicinity of the ester oxygen, which acts as the Lewis base. Both solvation configurations can be strengthened through a cooperative hydrogen bond between the CO₂ molecule's oxygen atom and the hydrogen atom of a methyl group. On the other hand, functional groups such as phenyl groups attached to the ester oxygen induce steric hindrance, leading to reduced interaction energies. Illustrations of Type I and Type II interactions are shown in Figure 4.

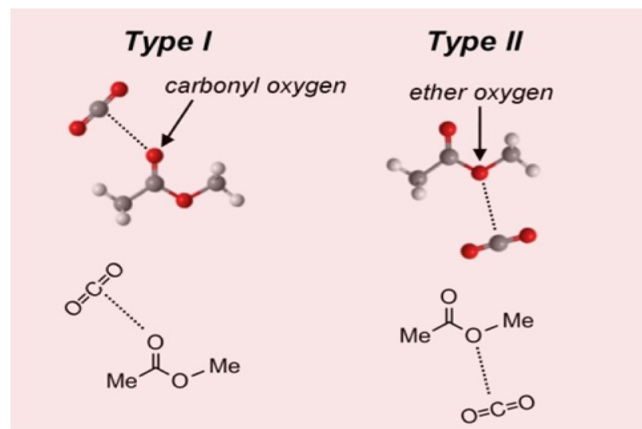


Figure 4. Illustration of the two different stable solvation configurations between CO₂ and esters [73].

In scCO₂ extraction, the solvation characteristics are closely related to the density of CO₂. As the mean molecular distance decreases with increasing density, the probability of solute-solvent interaction increases proportionally. The CO₂ density can be varied by adjusting pressure and temperature. At a constant temperature, increasing pressure raises the CO₂ density, thereby enhancing the solvation power. The temperature effect is more complex, particular for solid phase solutes. Several factors such as solvent density, solute vapor pressure and kinetic energy, compete. At a constant pressure, increasing temperature raises the solute vapor pressure and kinetic energy, but simultaneously reduces the solvent density, which lowers the probability of solute-solvent interactions. These competing effects are described by the cross-over effect. Below the cross-over pressure, the density effect dominates, and the solvation power of decreases with raising temperature at fixed pressure. Above the cross-over pressure, CO₂ density changes become less significant, and the vapour pressure and kinetic

effects take precedence. In this case, the solvation power increases with temperature at constant pressure [60,74].

CO₂ is not an effective solvent for high molecular weight polymers and ionic compounds of high polarity under readily achievable pressure and temperature conditions. Nevertheless, the solubility of such compounds in scCO₂ can be significantly enhanced by adding a co-solvent or modifier [60,61,75,76]. In this context, the role of scCO₂ is believed to mainly provide the supercritical phase, while the modifier-solute interactions contribute to the increased solubility increases of the polar compounds [72,76].

3.2. Chrastil model

A semi-empirical model was derived by Chrastil to correlate the solute solubility to temperature and density of the pure supercritical fluid solvent [77]. The model stated in Eq. (1) is valid for solute concentrations up to 200g/L.

$$S = \rho^k \exp\left(\frac{A}{T} + B\right) \quad (1)$$

The solubility of the solute (S) and the solvent density (ρ) are given in kg/m³, while the operating temperature (T) is measured in K. The parameters A, B, and, k are adjustable constants, which can be determined through linear regression of the experimental data, by plotting the natural logarithm of S against the natural logarithm of ρ . The constant A is related to the enthalpies of solvation (ΔH_{sol}) and vaporization (ΔH_{vap}), as well as the universal gas constant R, and is expressed as $A = (\Delta H_{sol} + \Delta H_{vap})/R$. Parameter B is a function of the average equilibrium association number (k) and the molecular weights of both solute and solvent.

3.3. Modelling of scCO₂ extraction curves

The rate of the scCO₂ extraction process depends on the solubility of the solute and the mass-transfer of the solute from the solid material to the bulk of the fluid. By plotting an extraction curve, the kinetics of the extraction process can be studied. An extraction curve is a plot of the cumulated extract versus the extraction time or the amount of consumed CO₂ during the extraction process. The extraction curve can be divided into three zones as illustrated in Figure 5 [78]. The initial part of the extraction curve, represented by a constant slope, is influenced by the solubility of the solute, while the second part, characterized by the curved line, is governed by mass transfer of the solute from the core of the particle to the bulk of the fluid. In Zone III, the extraction curve approaches a horizontal asymptote. This represents the total amount of solute in the substrate which can be extracted under the process condition.

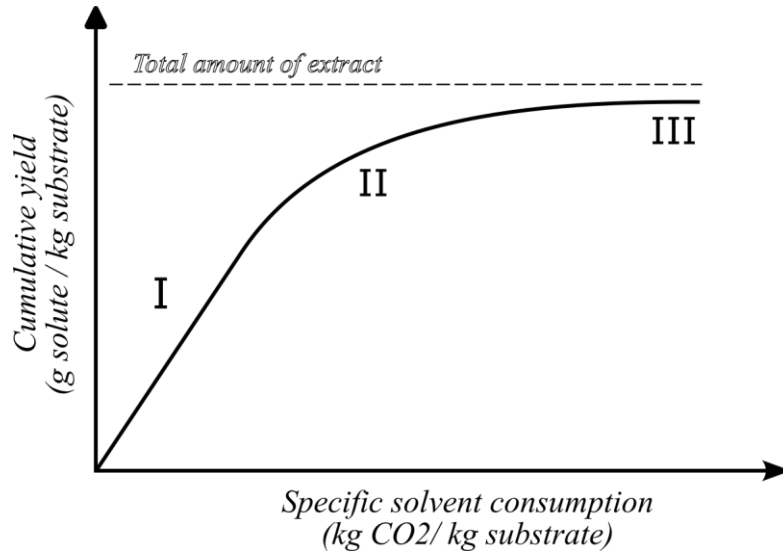


Figure 5. Representation of the main zones of a typical extraction curve. Zone I represents the solubility controlled extraction period, Zone II the mass transfer controlled extraction period, and Zone III represents the total amount of solute extractable under the process conditions.

Several different phenomenological models have been applied to model the extraction curves to get insights into the governed mass-transfer in scCO₂ extraction processes i.e, hot ball diffusion, desorption model, shrinking core model, broken and intact cell model, and hybrid models [79]. In this work, a general, versatile model able to fit different types of extraction curves was used [80]. The model was derived by Sovová based on the following assumptions:

- The solute is homogeneously distributed in the untreated solid.
- The solute particles contain an easily accessible solute fraction close to its surface and less accessible solute at its core.
- The less accessible solute first diffuses from the core to the particle surface, whereby the mass-transfer is characterized by the solid-phase mass transfer coefficient.
- The solute is assumed to be transferred directly from the surface to the fluid-phase and the mass transfer is characterized by the fluid-phase mass transfer coefficient.
- The fluid density is not affected by the dissolved solute as well as the surface area, void fraction and extraction bed characteristics.

The model categorizes the extraction curves into four distinct types, labelled A-D [80]. Type A extraction curves are independent of solute-matrix interactions and the straight part of the extraction curve equals the solubility of the solute. Extraction curves of Type B and C feature two straight sections, the first without and second with solute-matrix interactions. In Type D, solute-matrix interactions control the extraction process, and the linear relationship between solid and fluid phase equilibrium gives rise to the partition coefficient.

The first step to fit the retrieved extraction data is to identify the type of extraction curve. When the first part of the extraction curve consists of a single straight section, the extraction curve is either Type A or D. The type of extraction curve can be distinguished knowing the thermodynamic solubility of the solute. If the initial slope closely matches the solute solubility and there is a sharp transition between the first and second part of the extraction curve, it is Type A. Otherwise, it is Type D. If two straight sections are observed, it is of Type B, or C.

Type B and C can be differentiated based on the amount of solvent passed through the extraction bed at the intersection of the two straight sections. In a type C extraction curve, the second straight section starts later than in the Type B extraction curve.

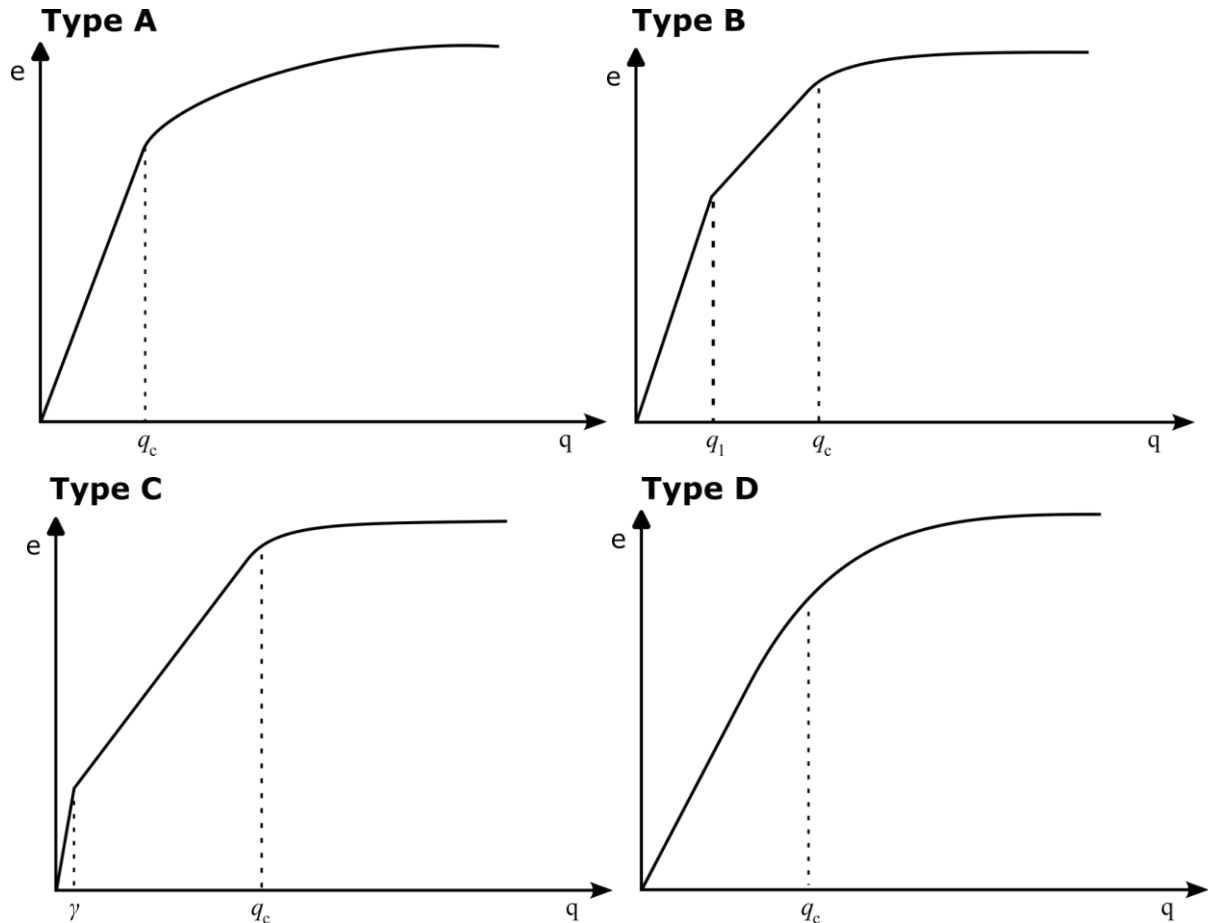


Figure 6. Illustration of the different extraction curve types (A-D) suggested by the Sovová's model.

Type A extraction curves are modelled by fitting a straight line to the first part of the extraction curve to Eq. (2) and the second part of the extraction curve using Eq. (3).

$$e = y_s q \text{ for } 0 \leq q \leq q_c \quad (2)$$

$$e = x_u [1 - C_1 \exp(-C_2 q)] \text{ for } q > q_c \quad (3)$$

whereas e is the extraction yield, y_s is the solubility, q is the relative amount of passed solvent, q_c is the co-ordinate of the crossing point of part 1 and part 2, x_u is the solute concentration in the untreated solid.

The model parameters C_1 and C_2 are then used to determine the fraction of easily accessible solute fraction, r , and solid-phase mass transfer coefficient, $k_s a_s$, according to

$$r = 1 - C_1 \exp\left(-\frac{C_2 q_c}{2}\right) \quad (4)$$

$$k_s a_s = \frac{(1-r)(1-\varepsilon)QC_2}{N_m} \quad (5)$$

where ε is the bed void fraction, Q is the solvent flowrate, and N_m is the amount of insoluble solid. N_m itself can be determined according to

$$N_m = (1 - c_u)N \quad (6)$$

where c_u is the solute share in the untreated solid ($\frac{x_u}{1+x_u}$), and N is the mass load.

Type B, C, and D extraction curves include solute-matrix interactions, and the linear part of the extraction data can be fitted using Eqs. (7) - (11).

$$\text{Type B: } e = y_s q \text{ for } 0 \leq q \leq q_1 = \frac{r(x_u - x_t) - \gamma K x_t}{y_s - K x_t} \quad (7)$$

$$e = y_s q_1 + (q - q_1)K x_t \text{ for } q_1 \leq q \leq q_c \quad (8)$$

$$\text{Type C: } e = q \frac{r(x_u - x_t)}{\gamma} = y_0 q \text{ for } 0 \leq q \leq \gamma \quad (9)$$

$$e = r(x_u - x_t) + (q - \gamma)K x_t \text{ for } \gamma \leq q \leq q_c \quad (10)$$

$$\text{Type D: } e = \frac{K x_u}{1 + K \frac{y_s}{\gamma}} q = y_0 q \text{ for } 0 \leq q \leq q_c \quad (11)$$

whereas x_u is the concentration in the untreated solid, x_t is the transition concentration, γ is the solvent-to-matrix ratio in the bed, K is the partition coefficient, and y_0 is the initial fluid phase concentration.

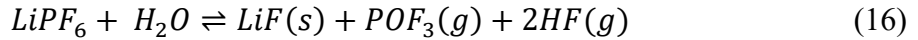
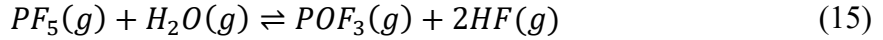
The easily accessible solute fraction, r , and solid-phase mass transfer coefficient are determined using Eq. (12) and (13).

$$r = 1 - C_1 \exp(-C_2 q_c) \quad (12)$$

$$k_s a_s = \frac{(1-r)(1-\varepsilon)QC_2}{N_m[1 - \left(\frac{(1-r)C_2}{K}\right)]} \text{ for } x_t > 0 \quad (13)$$

3.4. LiPF₆ decomposition

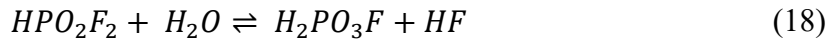
LiPF₆ is thermally and chemically unstable, and the decomposition pathway depends on the surrounding conditions [36–40,81]. In a dry, inert environment, anhydrous LiPF₆ typically decomposes thermally to solid LiF and gaseous PF₅ as shown in reaction 14. In the presence of moisture, PF₅ undergoes hydrolysis and produces POF₃, and gaseous HF as shown in reaction 15. However, when exposed to trace amounts of moisture or water, LiPF₆ can directly decompose endothermically, forming solid LiF, along with gaseous HF and POF₃ and HF as shown in reaction 16.



The onset decomposition temperature of LiPF₆ is debated in literature. Kock et al., [38] reported a decomposition onset point for anhydrous LiPF₆ at 134.84°C, while the hydrolysis reaction occurs at 114.46°C. However, LiPF₆ degradation products have been detected at temperatures below 90°C in the presence of the electrolyte solvents lime EC, EMC, DMC, and moisture [35,36,39]. Additionally, the hydrolysis degradation step was already observed at 87°C with 300ppm of H₂O [36].

3.5. Formation of inorganic phosphates by hydrolysis of POF₃

Inorganic phosphates are formed following these hydrolysis steps when POF₃ is in contact with water (Reactions (17)-(19)) [4,82]:



4. Experimental

The experimental, result, and discussion chapter are divided into three parts. The first part summarizes the findings of Paper I, and II. Two different processes to recover the electrolyte from spent LiB cells – low temperature thermal treatment and sub-and scCO₂ extraction are compared in this part. The second part contains the results of Paper III and presents the study of the solubility of EC in scCO₂. The third part is based on the findings in Paper IV. It studies the extraction behavior of the residual electrolyte solvents from LiB black mass.

4.1. Materials and Chemicals

The spent LiB pouch cells (NMC/graphite) used in Part I were produced for electrical vehicle applications and provided by an industrial partner. Further details about the LiB cell cannot be provided due to a non-disclosure agreement. The black mass (NMC-111) used in Part II was received from an industrial partner and used without any further treatment. The general steps performed by the industrial partner to produce the black mass contained pre-shredding, magnetic separation, air separation, vibration separation, and dust recovery to remove the casing, separator, and electrode materials.

Liquid CO₂ ($\geq 99.99\%$) was purchased from Air Liquid. Dry ice was provided by Cryotech. Nitric acid (HNO₃, $>65\%$), acetone ($>95\%$), acetonitrile ($>99.9\%$), ethylene carbonate ($>98\%$), ethyl methyl carbonate ($>99\%$), diethyl carbonate ($>99\%$), propylene carbonate (99%), and biphenyl ($>99\%$) were purchased from Merck Millipore.

4.2. Electrolyte recovery from untreated LiB cells using thermal treatment and scCO₂ extraction

4.2.1. Sample preparation

Discharged spent NMC/graphite LiB battery pouch cells were stored at -18°C for 2 days to minimize the evaporation of the electrolyte solvents during the opening process. The pouch cells were then opened, and the electrode stack was removed by slicing along the edges with a scalpel. Prior to each experimental run, rectangular pieces were cut from the electrode stack using a scalpel. The fixed dimension of the combustion boat and the extraction chamber set the maximum dimensions and weight of the sample. For the low temperature thermal treatment process the sample size was 9x1 cm (11.0 ± 0.9 g) and for the sub-and scCO₂ extraction process 14.7x0.5 cm (8.8 ± 0.7 g). Between the experimental runs, the electrode stack was kept inside a sealed plastic bag at -18°C.

4.2.2. Characterization of the electrolyte composition

The electrolyte amount and composition were analyzed using Fourier-transform infrared spectroscopy (FTIR) and thermogravimetric analysis (TGA). For TGA, one layer of the electrode stack (20.99 ± 0.01 mg), including cathode, separator, and anode, was placed into an alumina boat.

The FTIR measurements were conducted using electrode stack samples prepared by the method described previously. The sample was placed inside a combustion boat and inserted in a quartz tube. A constant N₂ flow (340 ml/min) was applied and the exhaust at room temperature (24 ± 2°C) was analyzed using FTIR in steps of 1 minute.

4.2.3. Low temperature thermal treatment process

The schematic presented in Figure 7 illustrates the set-up used for the low temperature thermal treatment process. A quartz tube with an inner diameter of 30 mm inner was placed inside a horizontal electrical tube furnace (RT 50-250/13, P330, Nabertherm). The furnace temperature was monitored using a thermocouple connected to a data logger (TC-08, Pico Technology). The N₂ flow (340 ± 20 ml/min) was controlled by a flowmeter. The quartz tube outlet was connected to two different configurations, Route A and Route B, depending on the type of analysis being performed. In route A, the exhaust gas was cryogenically trapped in a sample vial placed in a cold trap, consisting of a mixture of dry ice and acetone at -78°C. In route B, the exhaust gas was passed through a view cell, and FTIR spectra were monitored frequently over the entire process duration. A gas washing bottle containing 50ml of MQ water was connected in both routes before the exhaust was released to the environment.

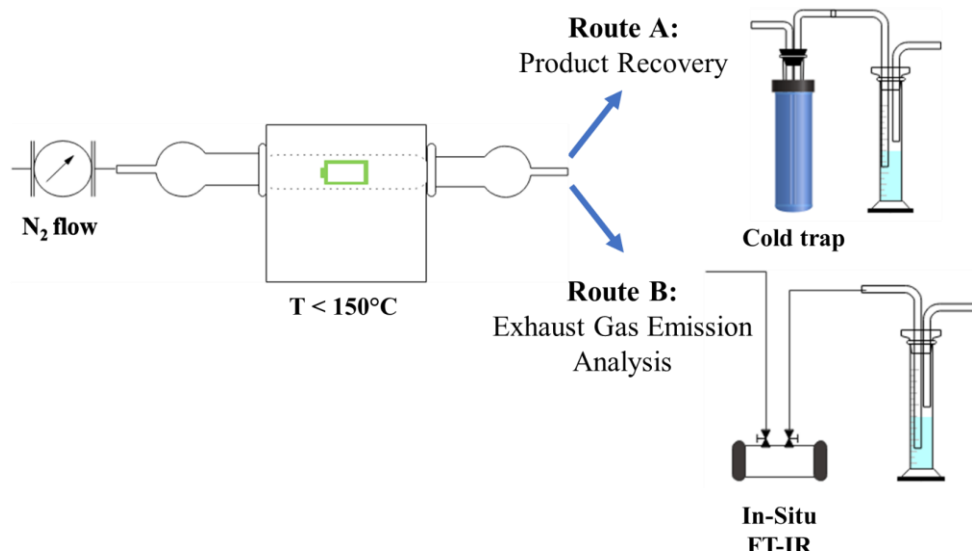


Figure 7. Schematic of the experimental set-up of the low temperature thermal treatment process.

A flowsheet summarizing the experimental procedure for the low temperature thermal treatment process, is shown in Figure 8.

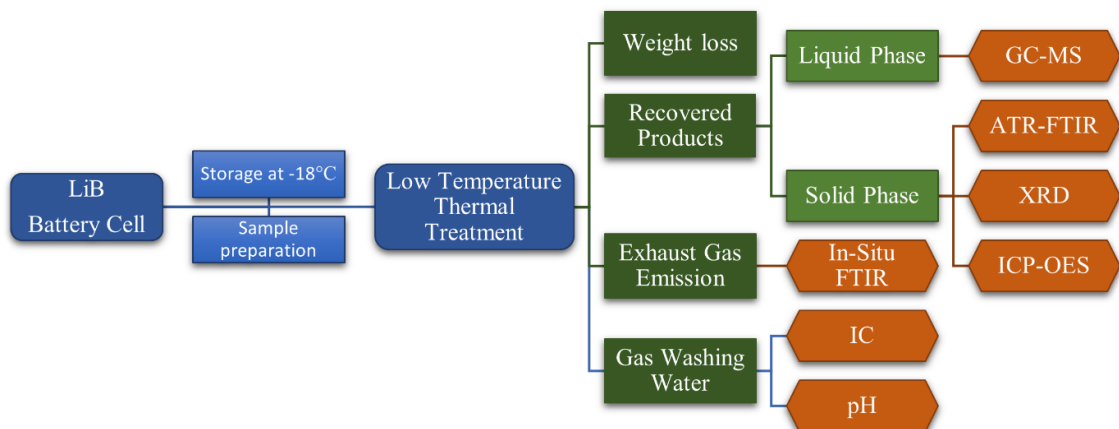


Figure 8. Flow-sheet of the experimental procedure of the low temperature thermal treatment process.

The low temperature thermal treatment process was conducted in triplicate for each temperature setting (90°C, 110°C, 130°C and 150°C) with the samples tested in random order. The LiB sample was placed inside a ceramic combustion boat (120 x 20 x 13 mm). To equilibrate the N₂ environment inside the quartz tube, the combustion boat was inserted into the quartz tube and positioned outside the hot zone of the furnace. After 5 minutes of equilibration, the combustion boat was moved into the center of the tube furnace under N₂ atmosphere. After 3 hours, the combustion boat was removed from the tube furnace and cooled down at room temperature (22 ± 2°C). The weight of the sample was measured with a high-precision scale both before and after the treatment, under ambient air.

Different analytical characterization techniques were performed after the thermal treatment process. The collected liquid product (Route A) was analyzed using gas chromatography coupled with mass spectroscopy (GC-MS), after dilution in acetonitrile with a dilution factor of 150.

A solid condensation product was collected from the walls of the quartz tube walls outside the hot zone of the tube furnace, once the setup had cooled. The collected solid sample was characterized by attenuated total reflection (ATR)-FTIR. Additionally, the sample was ground in a mortar for further analysis using X-ray diffraction (XRD) and inductively coupled plasma optical emission spectroscopy (ICP-OES).

The gas washing water was analyzed using ion chromatography (IC) and its pH was also measured. For the IC analysis, the samples were further diluted in MQ water with a dilution factor of 30.

4.2.4. Sub- and scCO₂ extraction process

The experimental set-up used for the scCO₂ extraction process is illustrated in Figure 9. A syringe pump (ISCO 260D, Teledyne ISCO) connected to an external thermostat (Model F10 & CM, Julabo) was used to provide compressed CO₂ at the desired pressure and temperature to the in-house made stainless-steel extraction chamber (7.5 ml). The extraction chamber was thermally stabilized using water circulation in a flexible hose connected to an external water bath (Model F12 & ED, Julabo). A thermocouple and manometer were used to monitor the temperature and pressure conditions within the extraction chamber. The CO₂ flow in the system was regulated using various shut-off valves and a meter valve. A stainless-steel filter (0.5 µm) was placed before the first shut-off valve. An electric temperature controller (W-510, Winkler) connected to electrical heated cables was whirled along the system outlet and set to 40 ± 5°C to avoid freezing the CO₂. For detailed information about the determination of the CO₂ flowrate and the collection of the extracts, see Paper II.

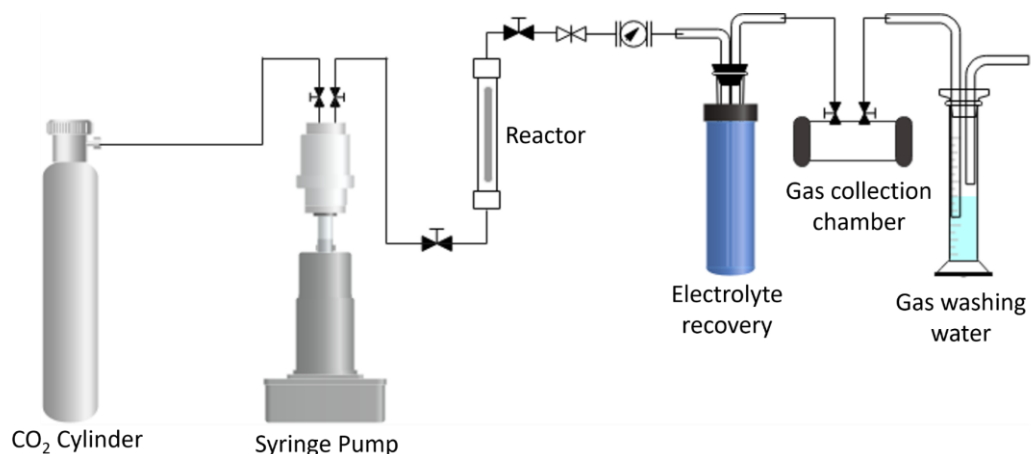


Figure 9. Illustration of the scCO₂ extraction process set-up.

The LiB electrode stack sample was placed inside the extraction chamber, which was then leak-tight closed using wrenches. Temperature-controlled water pipes were then whirled around the extraction chamber to maintain the desired process temperature (15°C - 55°C, with uncertainties of ±2°C). Next, the extraction chamber was pressurized to the experimental pressure (60 - 120 bar, with uncertainties of ±4 bar). A static equilibration period of 3 minutes was allowed to stabilize the system at the set temperature and pressure conditions. Then, a constant CO₂ flow was applied. After 30 minutes, the extraction chamber was depressurized, the chamber was opened using wrenches, and the electrode stack sample was retrieved. The sample mass was measured both before and after the extraction process using a high-precision scale. All experiments were conducted in triplicates. Throughout the process time of 30 minutes, the cold trap outlet exhaust was frequently monitored using FTIR spectroscopy.

The extracts were collected using a collection vial placed inside a cold trap, consisting of a mixture of dry ice and acetone at -78°C. The extract was then analyzed using ATR-FTIR, GC-MS and ICP-OES. For the ATR-FTIR analysis, 200 µl of each collected sample was used. GC-MS analysis was performed after the sample was diluted in acetonitrile with a dilution factor of 150. For ICP-OES, 50 µl of the collected extract was dissolved in 4.5 ml of 0.5 M HNO₃ and filtered.

4.3. Solubility of ethylene carbonate in scCO₂

An analogous experimental set-up was used as described in section 4.2.3. The major difference was the collection of the extracted samples. Two successive collection vials were used to maximize the collection yield of EC during the process. A detailed description of the set-up is provided in Paper III.

The solubility of EC in scCO₂ was studied isothermally (40°C, and 60°C) at different pressure conditions (80, 100, 120, 140, and 160 bar) using the gravimetric flow-through method. The equilibrium chamber was loaded with pure EC (1.00 ± 0.05 g) and was leak tight closed using wrenches. After stabilizing the temperature, the equilibrium chamber was pressurized using the syringe pumps to the desired pressure. An equilibration time of 7.5 minutes was used to stabilize the system, before initiating constant CO₂ flow using a metering valve. The flow rate (1500 ± 300 ml/min) referred to the flow at depressurized conditions at 1 bar and 22 ± 1 °C. The flowrate was as low as possible to achieve saturation in the equilibrium chamber. After 5 minutes of constant flow, the collection vials were weighed using a precision scale (resolution 0.01 mg and linearity ± 0.1 mg). Meanwhile, the equilibrium chamber was held in static mode for 5 minutes. The procedure was repeated multiple times until the collected EC amount closely matched the input weight. The experimental runs were conducted three times at all pressure and temperature conditions.

The solubility of EC in CO₂ was determined based on the slope coefficient of the linear regression of the data points within the linear range of the cumulative collected amount of EC (g) versus the amount of consumed CO₂ (g). The amount of consumed CO₂ was calculated based on Eq. (20).

$$m = V \times \rho \quad (20)$$

whereas V is the total volume of consumed CO₂ in ml during the extraction period of 5 minutes given by the syringe pump, and ρ is the density (g/ml) at the process condition taken from NIST Chemistry Webbook [83].

4.4. ScCO₂ extraction behavior of electrolyte solvents from LiB black mass

At first, the remaining electrolyte content in the LiB black mass was determined using a procedure adapted from Peschel et al. [84]. A sample of 3.00 ± 0.02 g of black mass was placed into a 50 mL vial, to which 5 mL of acetonitrile was added. After shaking the vial by hand for 5 minutes, the extraction solution was filtered and analyzed using GC-MS and ICP-OES. Prior to the analysis, the extraction solution was diluted by factors of 10 and 200, respectively. To assess the amount of remaining electrolyte in the black mass, 2.00 ± 0.02 g of the scCO₂-treated sample was processed using the same method.

The set-up for the scCO₂ extraction process was like the one described in Section 4.2.4. However, small adjustments were made. A bigger extraction chamber with a volume of 18 ml (length (15cm), inner (1.24 cm) and outer diameter (1.27 cm), frit filter (2 μ m)) was used. The collection system was also adopted. The extracts were absorbed into two consecutive collection vials placed in an ice-bath, each filled with acetonitrile. The first vial contained 5 ml and the second vial 25 ml of acetonitrile, respectively. After the collection vials, two gas washing

bottles were connected before the CO₂ was monitored using a mass flowmeter (red-y smart meter GSM, Vögtlin instruments). For detailed information about the set-up refer to Paper IV.

The extraction behavior of the residual electrolyte in the black mass was studied at different pressures (100 bar, and 140 bar) at 40°C. A mixture of black mass (3, 6, and 9g, with uncertainties of $\pm 0.05\text{ g}$) and glass beads ($d = 2\text{ mm}$) was charged into the extraction chamber. The glass beads were used to fill the voids in the extraction chamber and to prevent channeling effects during the extraction as the black mass is a fine powder with a particle size less than 0.4 mm. Then, the extraction chamber was pressurized and thermostated to the extraction conditions. After an equilibration time of 7.5 minutes, a constant flow rate of $1500 \pm 300\text{ ml/min}$, which was measured at depressurized conditions at $22 \pm 1^\circ\text{C}$ and 1 bar, was applied. For every 5 L of passed CO₂, the first collection vial was changed until a total CO₂ consumption of 65 L was reached. Then, the extraction chamber was depressurized. The CO₂ consumption was converted from L into g by multiplication of the calibration density of 1.977 g/L, which was provided by the mass flow meter software. Finally, the extraction chamber was depressurized and the black mass separated from the glass beads by sieving. The solution of the collection vials was quantitatively analyzed using GC-MS.

After the extraction process, parts of the scCO₂-treated black mass ($2.00 \pm 0.02\text{ g}$) were used to determine the remaining electrolyte content using the acetonitrile extraction method described previously and TGA. The collected solution in both collection vials were analyzed using GC-MS, and ICP-OES.

4.5. Formula and calculation protocols

The sample weight loss was determined in weight percentage (wt%) and was calculated according to Eq. (21):

$$\text{Weight loss} = \left(1 - \frac{m_{\text{after}}}{m_{\text{initial}}}\right) \times 100 \quad (21)$$

where m_{initial} is the initial sample weight and m_{afrer} is the sample weight after the electrolyte separation process.

The extraction yield was calculated according to Eq. (22).

$$E\% = \left(1 - \frac{m_{\text{after}}}{m_{\text{initial}}}\right) \times 100 \quad (22)$$

where E% is the extraction yield, m_{initial} is the initial electrolyte component, and m_{after} is the residual electrolyte component content. The electrolyte component content determination is described in Section 2.2.1.

The determined solubility (S , g/g) was converted into molar fraction solubility of EC (x_{EC}) using Eq. (23).

$$x_{EC} = S \frac{MM_{CO_2}}{MM_{EC}} \quad (23)$$

whereas MM_{CO_2} is the molar mass of CO_2 (44.01 g/mol) and MM_{EC} is the molar mass of EC (88.06 g/mol).

4.6. Analytical methods

4.6.1. Thermogravimetric analysis

Thermogravimetric analysis (TGA, Q500, TA Instruments) was conducted in a temperature range between 20°C and 300°C at a constant N_2 flow of 100 ml/min. The temperature was ramped with a rate of 5°C/min. In Part I of the thesis, the heating rate was automatically reduced and adjusted by the instrument based on the sample weight change using a high-resolution sensitivity of 4.0 and a resolution of 5.0.

4.6.2. Fourier-transform infrared spectroscopy

Fourier-transform infrared spectroscopy (FTIR, Spectrum Two, Perkin Elmer) was used to analyze gaseous, liquid, and solid samples.

FTIR spectra of gaseous samples were recorded in the range between 4000 cm^{-1} and 900 cm^{-1} with a resolution of 4 cm^{-1} and a total of 12 scans. The gas cell used for the analysis consisted of flat windows (CaF_2) and an optical path length of 10 cm.

For the FTIR analysis of the solid samples, the attenuated total reflection (ATR) method of the FTIR spectrometer was used. The sample was placed on the diamond of the universal ATR accessory and a sufficient force was applied using a pressure arm. The spectra were recorded in a range between 4000 cm^{-1} and 450 cm^{-1} with a resolution of 2 cm^{-1} .

4.6.3. X-ray diffraction analysis

A Bruker D8 Advance was used to perform the X-ray diffraction analysis (XRD) of the crystallographic structure of the collected solid phase product in the low temperature thermal treatment process. The diffraction pattern was recorded in the 2Θ range of 10 -55° using the characteristic K_α wavelength of 1.5406 Å provided by a Cu radiation source. The operating voltage and current were set to 40 kV and 40 mA, respectively. Prior to the analysis, the sample was ground with a mortar. For interpretation of the diffraction pattern the EVA software and PDF database were used.

4.6.4. Gas chromatography – mass spectroscopy

Gas chromatography coupled to mass spectroscopy (GC-MS) was used to analyze the separated electrolyte composition. The information about the instrument type and GC settings used in the different Parts of the thesis are stated in Table 2.

Table 2. Parameters for the GC-MS analysis.

	Thermal treatment (Section 4.2.3)	Sub-Supercritical CO ₂ Extraction (Section 4.2.4)	Extraction behavior (Section 4.4)
Instrument	7890A, Agilent Technologies	7890A, Agilent Technologies	GC-2030 NX, GCMS-QP2020 NX, Shimadzu
Column	Agilent HP-5MS 5% Phenyl Methyl Silox column (30 m x 250 µm x 0.25 µm)	Agilent HP-5MS 5% Phenyl Methyl Silox column (30 m x 250 µm x 0.25 µm)	ZB-5MS column (30 m x 250 µm x 0.25 µm)
Injection			
Carrier gas	He (1 ml/min)	He (1 ml/min)	He (1 ml/min)
Injection temperature	250°C	250°C	270°C
Split ratio	1:100	1:100	1:20
Purge flow	3 ml/min	3 ml/min	3 ml/min
Oven program			
Initial temperature	40°C, 1 min	40°C, 1 min	40°C, 1 min
Heating rate	30°C/min	20°C/min	20°C/min
Final temperature	230°C, 3 min	230°C, 2 min	260°C, 2 min
MS conditions			
Ionization	Electron impact	Electron impact	Electron impact
Filament voltage	70eV	70eV	70eV
Source Temperature	230°C	230°C	230°C
Mass range	15-300 m/z	15 – 300 m/z	30 – 300 m/z

For quantification, the integrated peak areas of ethylene carbonate (43 m/z), propylene carbonate (57 m/z), ethyl methyl carbonate, dimethyl carbonate (45 m/z), diethyl carbonate, and biphenyl (154 m/z) were used, whereas the quantification ions are given in brackets. Mixed standard solutions with concentrations of 10, 25, 50, 100, 200, 1000, and 2000 mg/L were prepared using acetonitrile.

4.6.5. Ion chromatography

Ion chromatography (IC, Metrohm 771 IC Compact, DX-100, Dionex) was used to characterize the gas washing water of the low temperature thermal treatment process. Anion analysis was conducted using a DionexIonPac column (AG4A- SC, 4 x 50 mm, ThermoFisher Scientific), and a carbonate buffer (1.7 mM NaHCO₃, 1.8 mM Na₂CO₃) as an eluent. The sample were diluted in MQ water (1:30), and the injection volume was 20 µl. The retention time of standards containing F⁻ and PO₄³⁻ were used to confirm the peaks.

4.6.6. Inductively coupled plasma – optical emission spectroscopy

Inductively coupled plasma – optical emission spectroscopy (ICP-OES, ThermoFisher Scientific, iCAP PRO) was used for elemental analysis. Standards containing Li, Ni, Co, Mn, Fe, Cu, Al, P, Na, S, Si, Cd, Ca, and Zn were prepared by dilution in 0.5M HNO₃ for the linear calibration range between 0.3 to 20 ppm. The approximate detection limit was 0.1 ppm. Prior to the analysis the samples were diluted in 0.5M HNO₃.

5. Results

The results chapter is divided into three parts. The first part summarizes the results published in Paper I, and II and compares two different processes to recover the electrolyte from spent LiB cells – low temperature thermal treatment and sub-and supercritical CO₂ extraction. Then, in the second part the solubility of ethylene carbonate in scCO₂ was studied (Paper III). Finally, the results were applied for the extraction of the residual electrolyte solvents in LiB black mass (Paper IV).

5.1. Electrolyte recovery from untreated LiB cells using thermal treatment and scCO₂ extraction

5.1.1. Characterization of the electrolyte composition

As a first step, the composition of the electrolyte of the LiB pouch cells was determined using FTIR analysis of its exhaust at room temperature ($24 \pm 2^\circ\text{C}$) under N₂ flow. The exhaust FTIR spectra of the exhaust monitored after 1, 3, and 5 minutes are shown in Figure 10. For reference, the gas phase spectra of pure DMC, EMC, and EC are also plotted. The vibrational peaks at 1780 cm⁻¹, 1463 cm⁻¹, and 1295 cm⁻¹ were associated with DMC [85], while the peaks at 1772 cm⁻¹, 1378 cm⁻¹, and 1370 cm⁻¹ were attributed to EMC [86]. The peaks at 1876 cm⁻¹, 1868 cm⁻¹, and 1860 cm⁻¹ correspond to EC in gas phase [87]. This indicated that the electrolyte solvents contained a mixture of DMC, EMC, and EC.

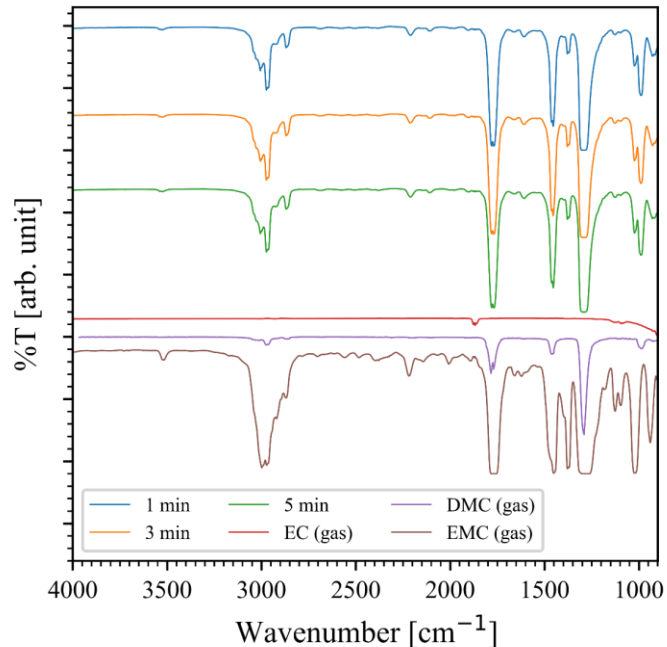


Figure 10. FT-IR spectra of the LiB sample exhaust gas at room temperature (24°C) after 1, 3, and 5 min. The gas phase spectra of DMC, EMC, and EC are plotted as a reference.

TGA was conducted to verify the electrolyte solvent mixture composition based on their boiling points. The thermogravimetric (TG) and differential thermogravimetric (DTG) curves of the electrode stack sample (20.99 ± 0.1 mg) within the temperature range of 20°C to 300°C is plotted in Figure 11. The determined weight loss was 9.34 wt%. Three distinct peaks at 96°C , 109.6°C , and 128.9°C were observed in the DTG curve, which align with the boiling points of DMC (90°C) and EMC (107°C). The peak at 128.9°C is attributed to the onset decomposition temperature of LiPF₆ (134.84°C) [21]. No peak was observed at the boiling point of EC (248°C), likely because EC evaporated along with the other components before reaching its boiling point. The DTG curve remained stable after 150°C . Consequently, the maximum temperature for the thermal treatment process was set to 150°C , and other temperatures to 90°C , 110°C , and 130°C based on the DTG peaks.

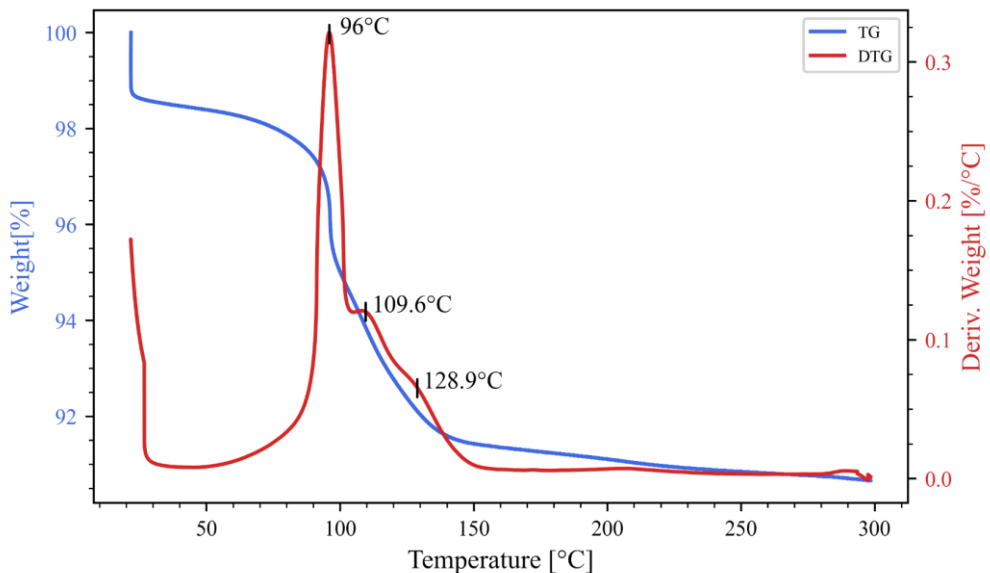


Figure 11. Thermogravimetric (TG, blue) and differentiate thermogravimetric (DTG, red) curves of the LiB electrode stack sample.

5.1.2. Low temperature thermal treatment

The effects of low temperature thermal treatment at various temperatures on the electrolyte separation, its exhaust and collected products were analyzed in the following. The sample weight loss, expressed as weight percent (wt%), at various process temperatures of 90°C , 110°C , 130°C , and 150°C is shown in Figure 12. At a temperature of 130°C , the weight loss stabilized at 13.9 ± 0.1 wt%. It can be observed that with raising temperature, the standard deviation of the triplicate measurements decreased.

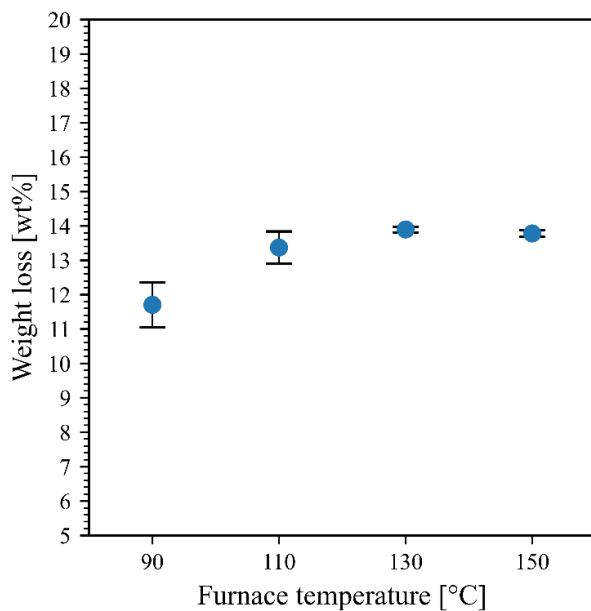


Figure 12. LiB sample weight loss given in weight percentage (wt%) after the low temperature thermal treatment for 3 hours under constant N_2 flow at various temperature conditions. The uncertainty bars in the plot represent the standard deviations (1σ) of the triplicates at each temperature.

Both liquid and solid phase products were collected after the electrolyte separation via low temperature thermal treatment. The liquid phase product composition was analyzed using GC-MS, and the resulting chromatographs are plotted in Figure 13. The peaks observed at retention times of 2.33 min, 2.81 min, and 4.59 min were identified as DMC, EMC, and EC, respectively, based on the NIST 08 library.

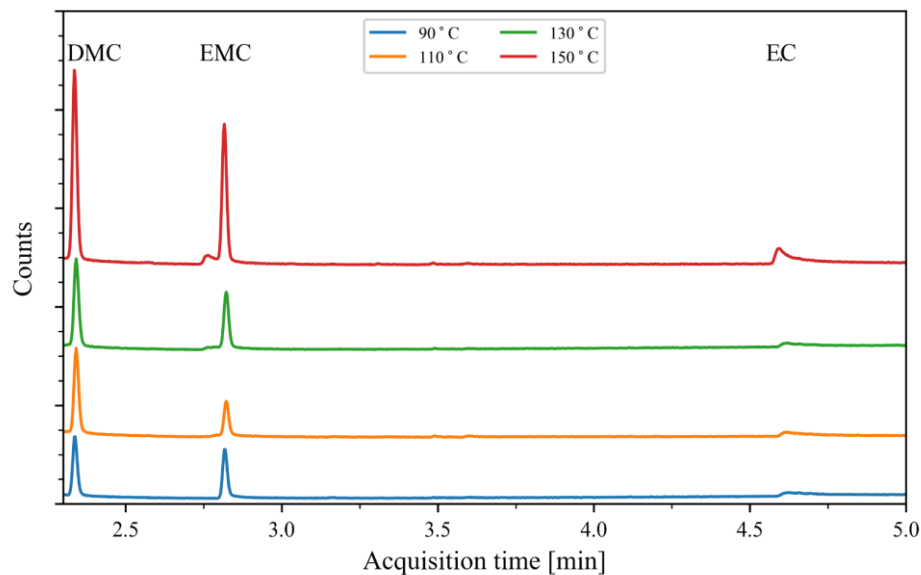


Figure 13. Chromatograms (GC-MS) of the recovered electrolyte at different thermal treatment process temperatures of 90°C, 110°C, 130°C, 150°C.

Approximately 0.3 g (\approx 20-25% of the total weight loss) of crystalline condensate residue was collected from the wall of the quartz tube after the processes, as shown in Figure 14. The composition of the recovered solid phase product was analyzed using ATR-FTIR, XRD, and ICP - OES.

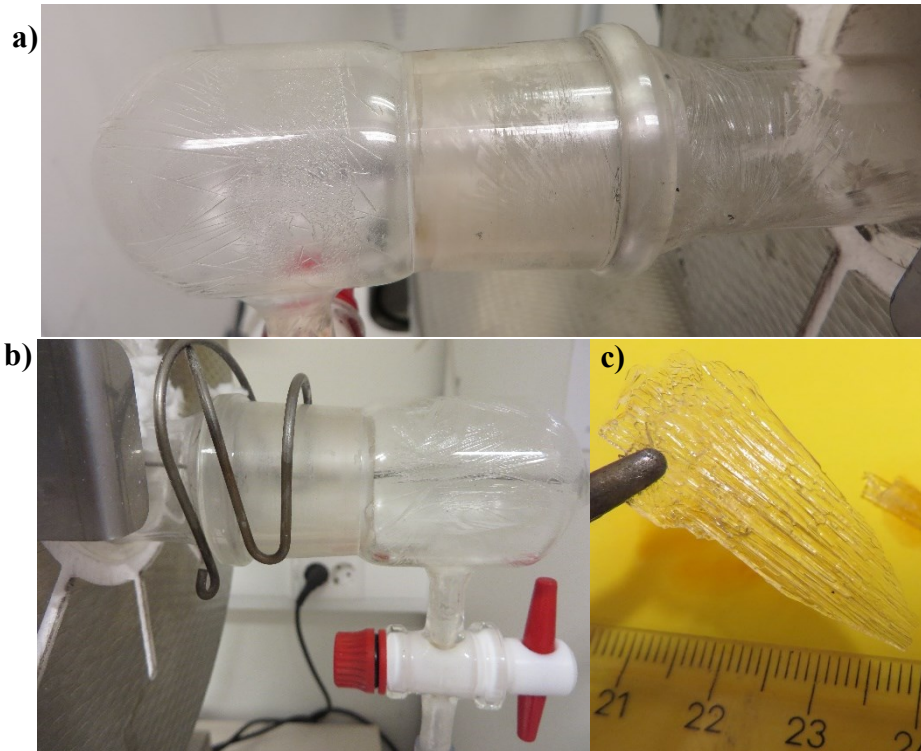


Figure 14. a) and b) Quartz tube wall coated with the condensed solid phase product after the low temperature thermal treatment. c) Zoomed in image of the collected solid phase product.

Figure 15 shows the ATR-FTIR spectra of the recovered crystalline solid phase residue, collected after the low temperature thermal treatment process at 110°C, 130°C, and 150°C and the spectrum of pristine EC in solid phase as a reference. The spectra match the EC reference spectrum at all temperatures. Additionally, minor peaks between 1050 cm^{-1} and 450 cm^{-1} , corresponding to the vibrational modes of POF₃ (a,c) and LiPF₆ (b,d) were observed in the spectra.

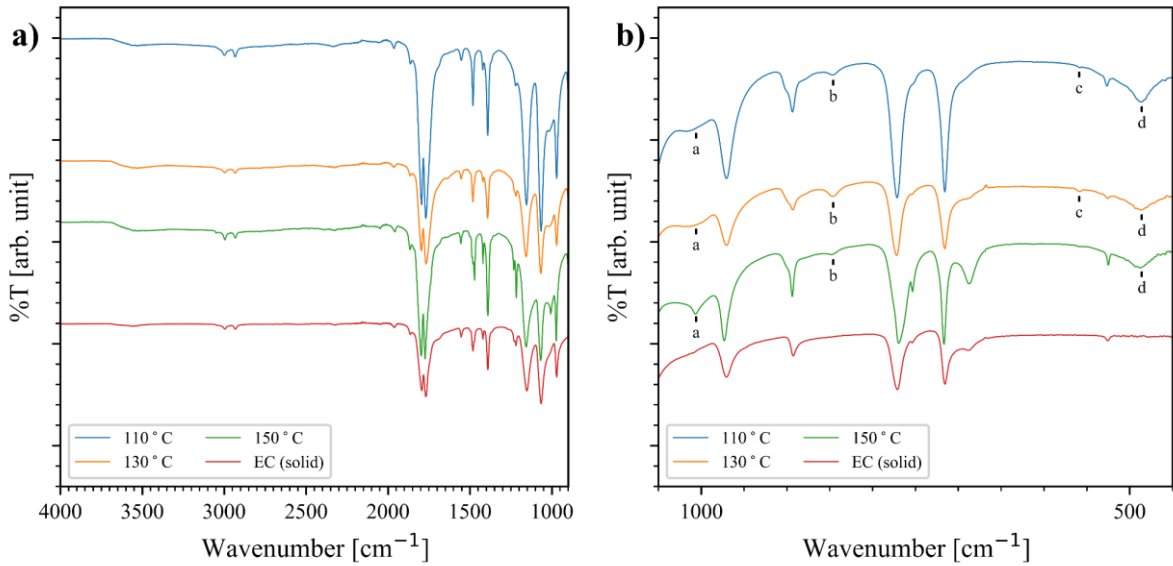


Figure 15. ATR-FTIR spectra between a) 4000-900 cm^{-1} and b) 1050-450 cm^{-1} of the quartz tube residue collected after the low temperature thermal treatment experimental runs at 110°C, 130°C, and 150°C. EC in solid phase is given as a reference.

The XRD diffraction pattern of the recovered solid phase product, recorded in the 2Θ range from 10° to 55° , is plotted in Figure 16. The diffraction peaks match the peaks of EC, which has a monoclinic crystal structure (PDF Card No: 00-008-0768). According to ICP-OES results, elemental impurities of Li (0.8 ppm), Mn (2.3 ppm), Co (0.94 ppm), Cu (1.29 ppm), Ni (0.57 ppm), and Al (0.16 ppm) were detected in recycled EC.

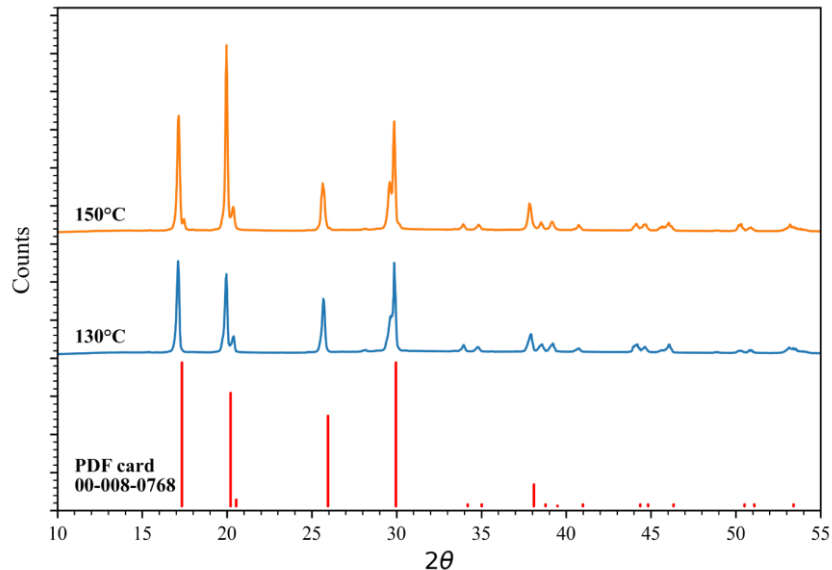


Figure 16. XRD pattern in the range from 10° to 55° 2Θ of the collected solid phase product after the thermal treatment process at 130°C and 150°C.

The process exhaust gas was analyzed using in-situ FTIR throughout the entire experimental period. The recorded FT-IR spectra at various time intervals (1, 15, 30, 60, 90, 120, and 180 minutes) for different process temperatures (90°C , 110°C , 130°C , and 150°C) are plotted in Figure 17. At all temperature conditions, characteristic peaks corresponding to the electrolyte solvents DMC, EMC and EC were observed. Additional peaks corresponding to HF (4000 cm^{-1} to 3600 cm^{-1}) and POF_3 (1428 cm^{-1} , 1416 cm^{-1} , 1404 cm^{-1} , and 991 cm^{-1}) were detected at all temperature conditions [35–37].

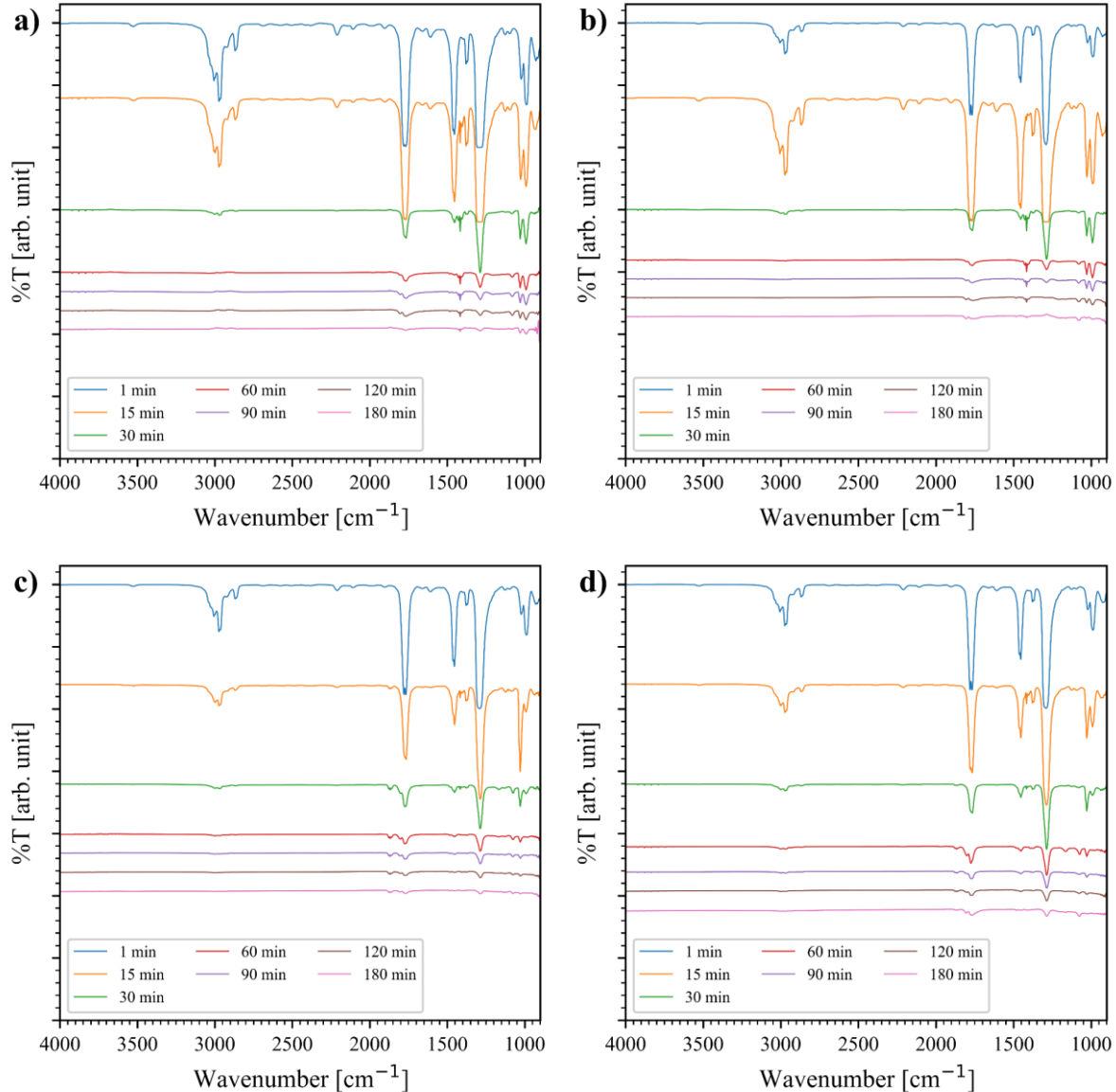


Figure 17. In-Situ FT-IR spectra of the process exhaust gas after 1, 15, 30, 60, 90, 120, and 180 min at a) 90°C , b) 110°C , c) 130°C , and d) 150°C .

The electrolyte solvent separation rate was determined by monitoring the change in the relative absorption intensity of the electrolyte solvents DMC and EMC. Due to their strong peak intensities and high selectivity, the relative absorption intensities of the vibrational peaks at 1780 cm^{-1} (vC=O of DMC) and at 1284 cm^{-1} (vO-C-O of EMC) were tracked throughout the

entire process, as shown in Figure 18. It is important to note that the equilibration time, defined as the period before the sample was introduced to the hot zone of the furnace, is denoted as -5 to 0 minutes.

During the equilibration time relative absorption intensities greater than 74% for the C=O peak of DMC and 90% for the O-C-O peak of EMC were already observed in the FT-IR spectra across all temperature conditions. Once exposed to the process temperatures, an immediate increase to 100% absorption intensity was observed. The relative absorption intensity began to decrease after 40 minutes, eventually stabilizing around 60 minutes for DMC and 80 minutes for the EMC.

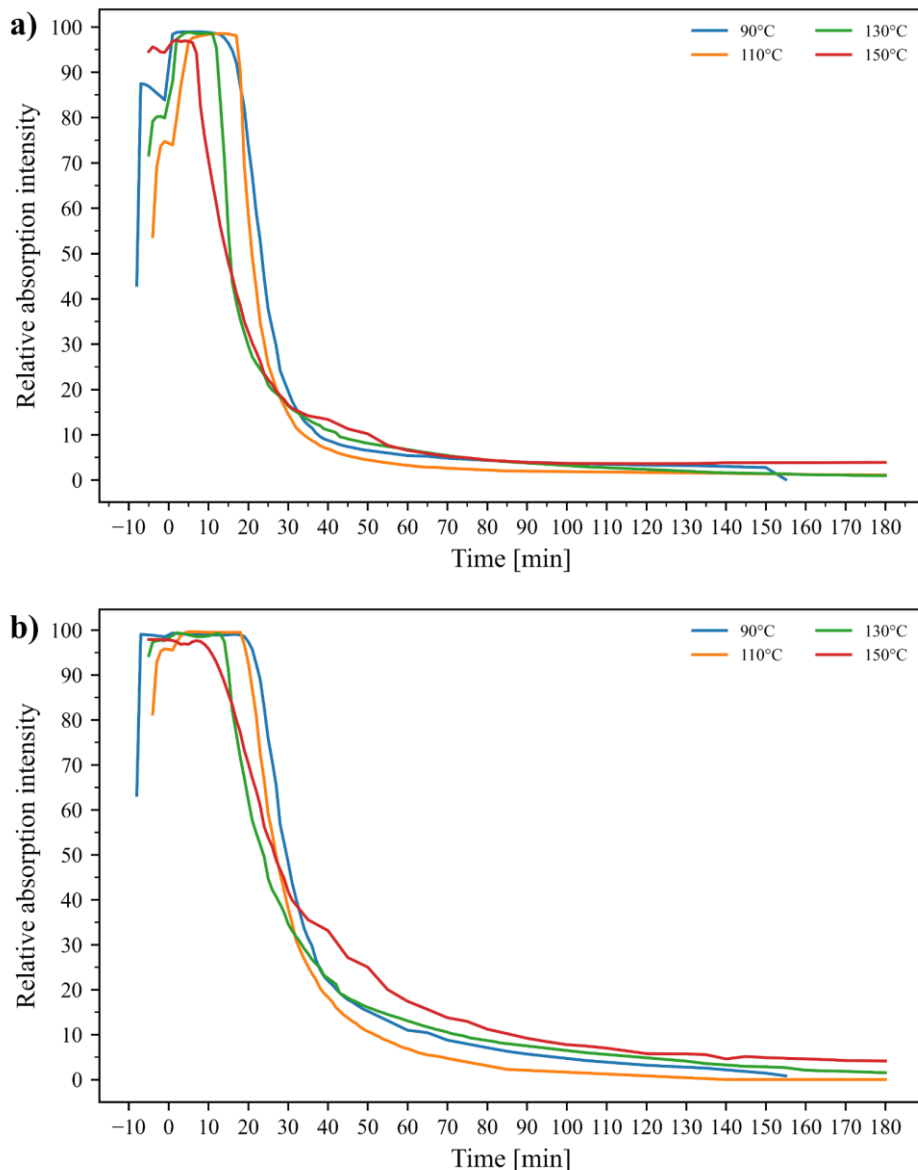


Figure 18. Relative absorption intensity over the thermal treatment process time of 180 minutes of the a) C=O peak of DMC at 1780 cm⁻¹ and b) O-C-O peak of EMC at 1284 cm⁻¹.

The time-dependent changes in relative absorption intensity for the characteristic peaks of HF (3878 cm^{-1}) and POF_3 (1416 cm^{-1}) were plotted over the entire 180-minute process period, as shown in Figure 19. The vibrational peaks of HF and POF_3 appeared simultaneously between 4 and 10 minutes, depending on the process temperature. It is evident that a higher process temperature results in a shorter duration for the hydrolysis degradation of LiPF_6 . At process temperatures of 130°C and 150°C , the relative absorption intensity stabilized at a constant level after a maximum of 70 minutes. At temperatures below 130°C , by contrast, the POF_3 peak continued to decrease without stabilizing throughout the entire process time. The gas washing water was analyzed after the thermal treatment process using IC and the results plotted in Figure 20. Distinct peaks at retention times at 2.8, and 10.8 minutes were observed, and assigned to F^- and PO_4^{3-} .

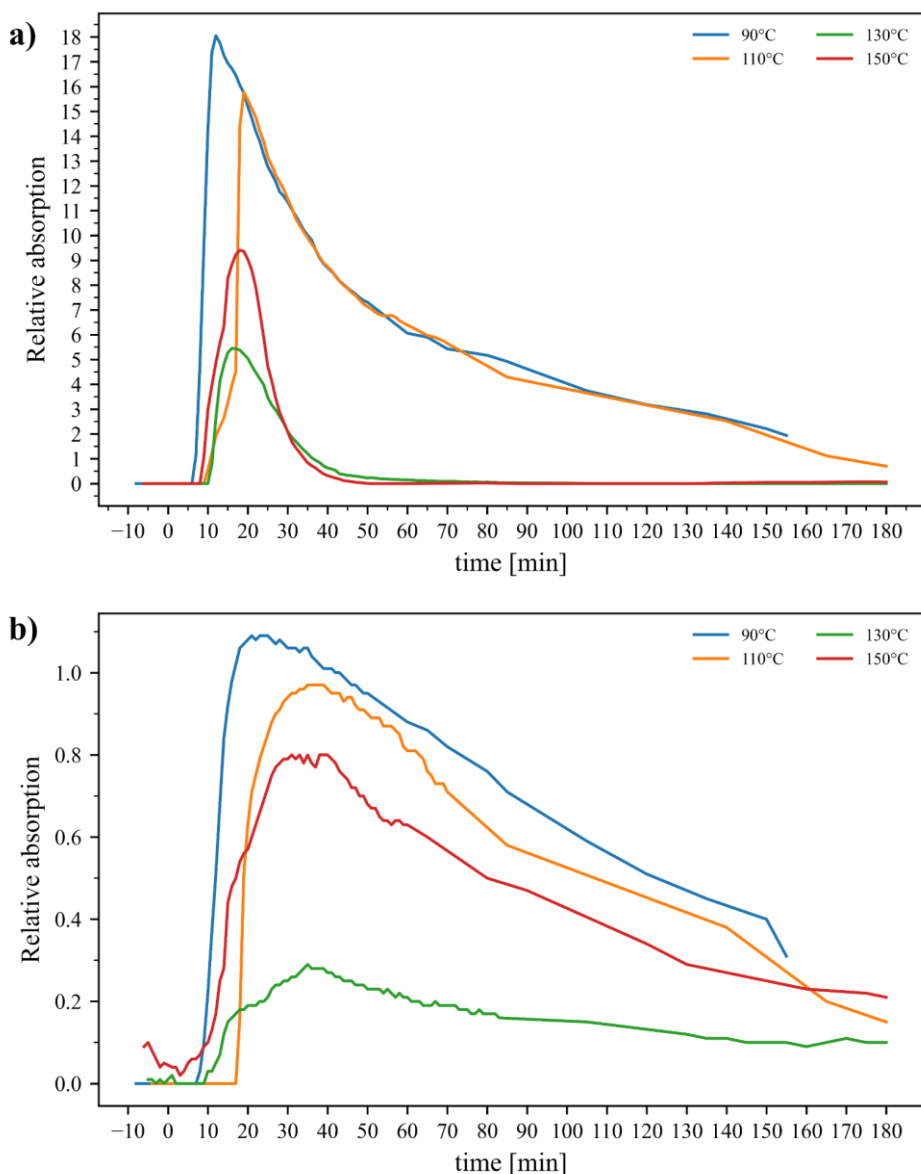


Figure 19. Relative absorption intensity over the entire process time of the characteristic peaks of a) POF_3 at 1416 cm^{-1} , and b) HF at 3878 cm^{-1} .

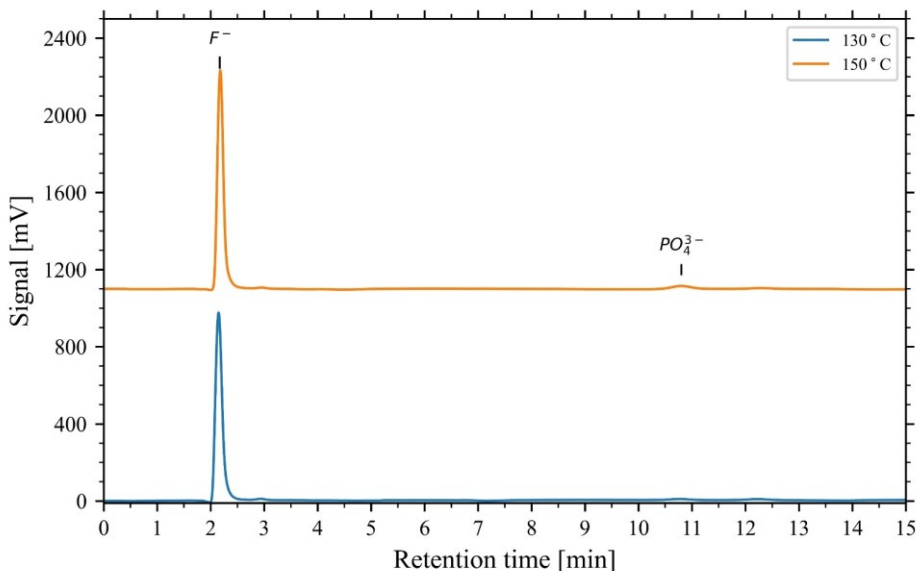


Figure 20. IC chromatograph of the gas washing water at process temperatures of 130°C and 150°C.

5.1.3. Sub-and sc-CO₂ extraction

This section summarizes the results when using scCO₂ to separate the electrolyte solvents from the LiB pouch cells. The effects of pressure (60-120 bar), temperature (15-55°C) and the corresponding CO₂ density on the sample weight loss expressed in weight percentage (wt%) and the electrolyte separation yield (%) are plotted in Figure 21. The electrolyte separation yield was calculated based on the maximum electrolyte separation yield achieved during the low temperature thermal treatment process, which was 13.9 ± 0.1 wt% at 130°C. The total electrolyte weight was then adjusted to 14.2 wt%, accounting for the LiF residues remaining after the decomposition of LiPF₆. 88.2% of the total electrolyte amount was attributed to the electrolyte solvent, equating to 12.5 wt% of the electrode stack. The contribution of LiPF₆ was estimated to be 11.8%, corresponding to 1.7 wt% of the electrode stack.

As shown in Figure 21a, the maximum electrolyte separation yield of 66% (9.4 ± 0.2 wt%) was achieved at 80 bar. Beyond this point, a pressure increase did not further enhance the electrolyte separation yield. In fact, a slight decrease to 64% (9.02 ± 0.07 wt%) at 120 bar was observed. Figure 21b shows that raising the temperature above 29°C resulted in a (linear) decrease in electrolyte separation yield, whereas below 29°C the electrolyte separation efficiency remained rather constant at 66% (9.4 ± 0.2 wt%) within the standard deviation of the triplicates.

Pressure and temperature directly influence the CO₂ density during the extraction process. Figure 21c shows the weight loss and separation yield against the CO₂ density at the different process conditions. The electrolyte separation yield clearly depends on the CO₂ density. The electrolyte separation yield remained relatively constant within the CO₂ density range of 600 kg/m³ to 900 kg/m³. However, below a CO₂ density of 600 kg/m³, the separation yield decreased. The highest electrolyte separation yield of 66% was reached at a CO₂ density of 715 kg/m³.

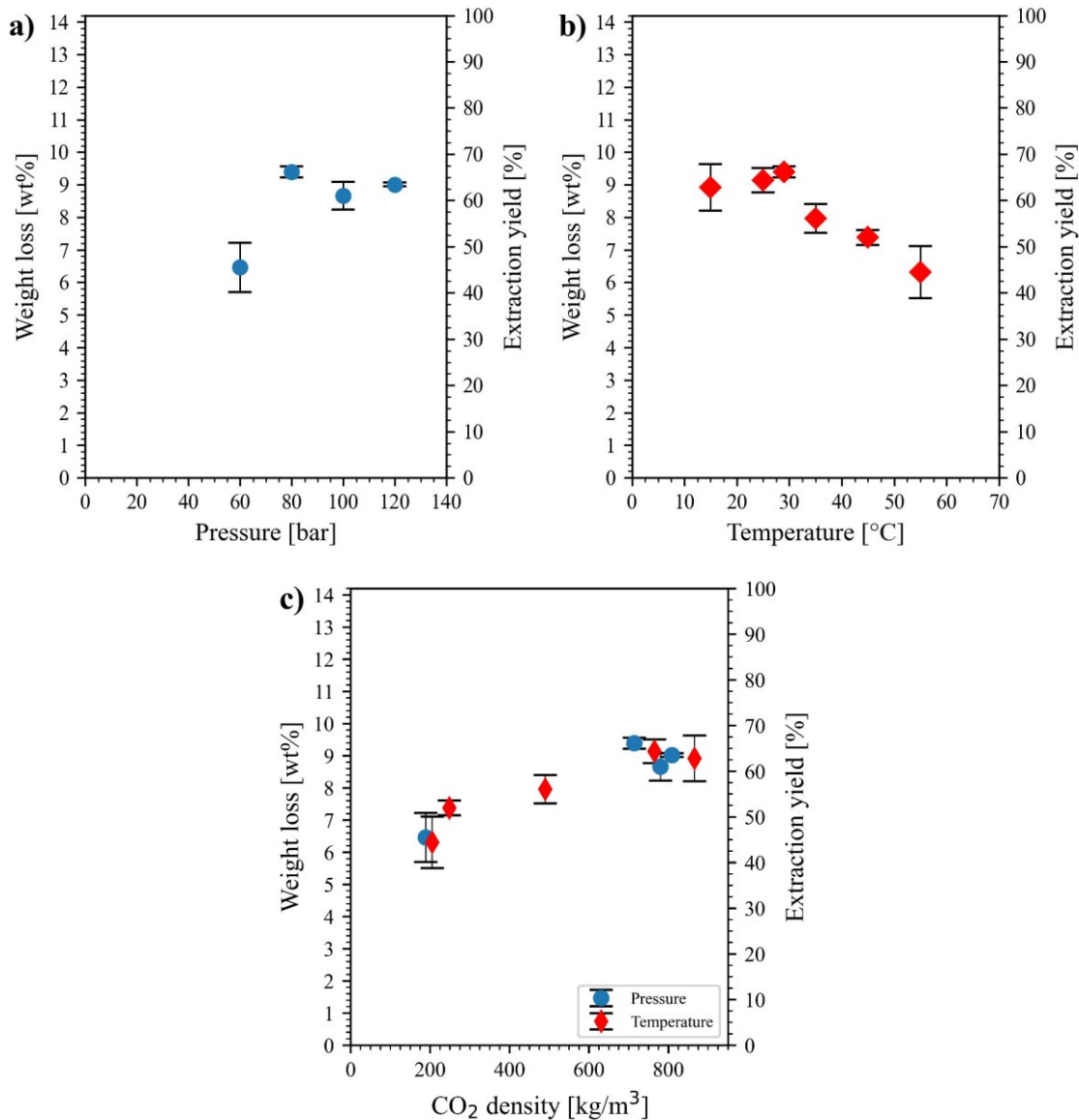


Figure 21. LiB sample weight loss in weight percentage (wt%) and corresponding electrolyte separation efficiency after the sub-and scCO₂ extraction process with different process parameters. a) dependence of pressure at 29°C, b) dependence of temperature at 80 bar, c) dependence of CO₂ density. The uncertainty bars in the plots represent the standard deviations (1σ) of the triplicates at each process condition.

The composition and purity of the collected extracts were analyzed using GC-MS and ICP-OES. The GC-MS chromatographs of the collected extract at the different CO₂ process densities, shown in Figure 22a, reveal peaks at acquisition times of 2.35, 2.93, and 5.31 minutes. Additionally, minor peaks at 3.18, 3.35, 3.63, and 3.85 minutes are highlighted in the focused plot in Figure 22b. The peaks at 2.35, 2.93, and 5.31 minutes correspond to the organic electrolyte solvents DMC, EMC and EC, respectively. The peaks at 3.18, 3.63, and 3.85 minutes were assigned to the electrolyte decomposition products dimethyl

fluorophosphate (DMFP), DEC, and ethyl methyl fluorophosphate (EMFP). The peak at 3.35 minutes was assigned to the electrolyte additive vinylene carbonate (VC).

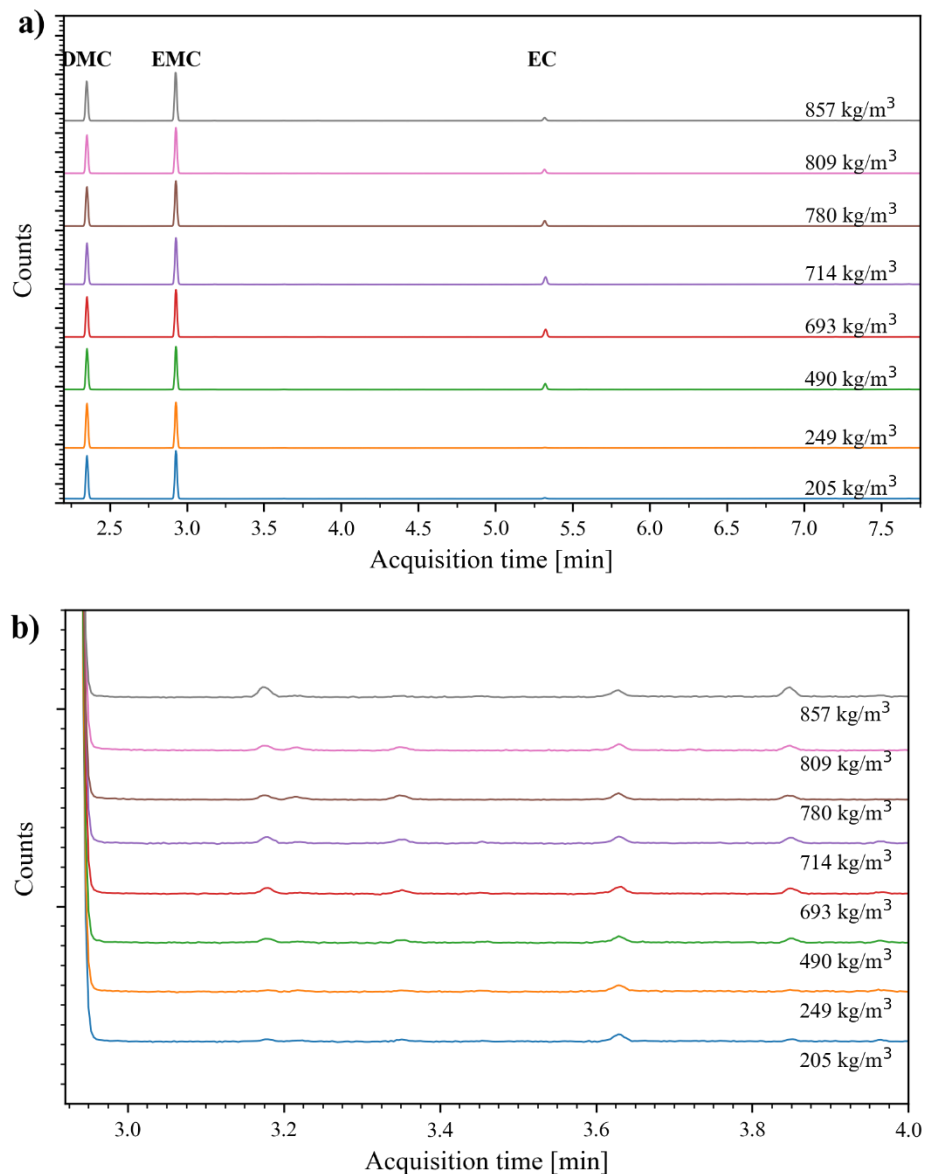


Figure 22. a) GC-MS chromatogram of the collected liquid phase product at various CO_2 densities and (b) focused between 2.9 and 4 minutes.

The semi-quantitative analysis of the collected extract, in relation to the CO_2 density, is shown in Figure 23. The proportion of EC was found to be dependent on the CO_2 density. At densities below 300 kg/m^3 less than 2% of EC was detected in the extract. As the CO_2 density reached 714 kg/m^3 , the share of EC in the extract increased to 9.7%, compared to 3.9% at a CO_2 density of 857 kg/m^3 .

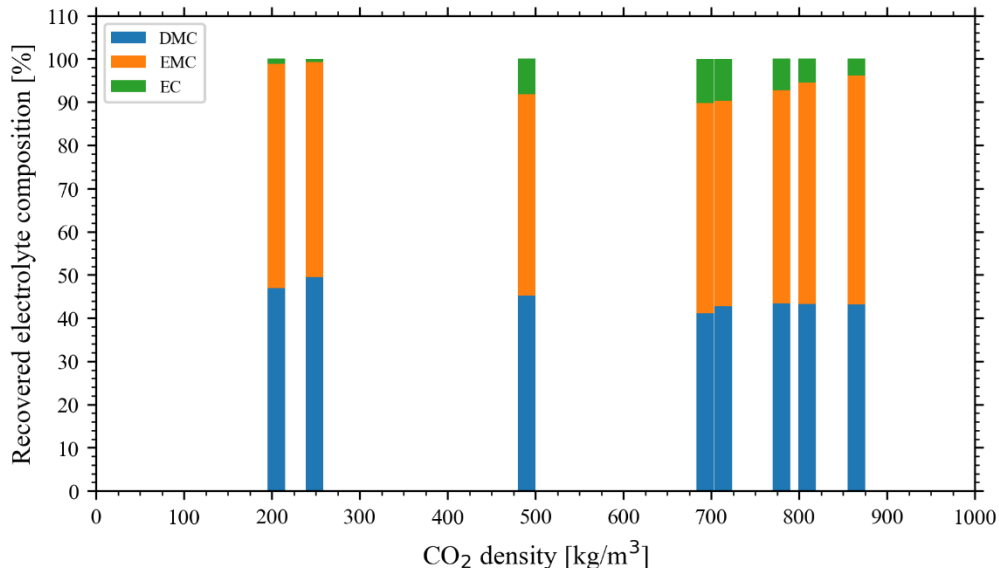


Figure 23. Composition of the collected liquid phase product obtained at various CO₂ process densities based on the GC-MS analysis.

ICP-OES was used to quantify the elemental composition of the extract. P and Al were detected at concentrations of 360 ± 65 mg/L and 5.2 ± 0.4 mg/L, respectively, across all process conditions. Li, in turn, was below the detection limit of the instrument.

The exhaust gas from the cold trap outlet was continuously analyzed using FTIR spectroscopy throughout the entire process. The results for the process conditions yielding a CO₂ density of 715 kg/m³ is plotted in Figure 24a. These conditions were selected process conditions as they provided the highest separation yield. The FTIR spectra revealed strong CO₂ vibration peaks (3728 cm^{-1} , 3704 cm^{-1} , 3624cm^{-1} , 3599 cm^{-1} , 2349 cm^{-1} (broad)), along with peaks corresponding to carbon monoxide (around 2075 cm^{-1}) at all process times. Additionally, vibrational peaks associated with DMC (1780 cm^{-1} (vC=O), 1463 cm^{-1} (CH₃ sym. def.), and 1295 cm^{-1} (v_aO-C-O)) and EMC (1772 cm^{-1} (vC=O), 1378 cm^{-1} (CH₃) and 1370 cm^{-1}) were detected. No vibrational peaks corresponding to gas-phase EC (1876 cm^{-1} , 1868 cm^{-1} , and 1860 cm^{-1}) were observed. Furthermore, vibrational peaks associated with the LiPF₆ decomposition products HF (4000 cm^{-1} to 3600 cm^{-1}) and POF₃ (1428 cm^{-1} , 1416 cm^{-1} , 1404 cm^{-1} and 991 cm^{-1}) were not detected in the cold trap exhaust gas.

The FTIR spectra of the exhaust gas emissions prior to the collection chamber are shown in Figure 24b. In this case, vibrational peaks assigned to EC were detected along with peaks belonging to DMC, and EMC. Again, no vibrational peaks corresponding to HF and POF₃ were observed.

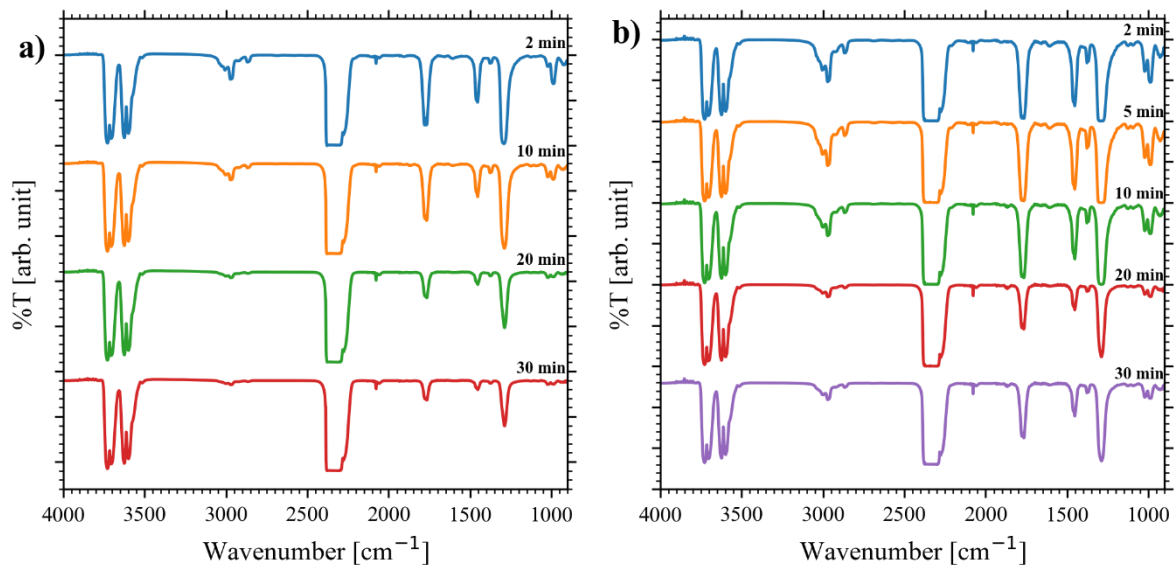
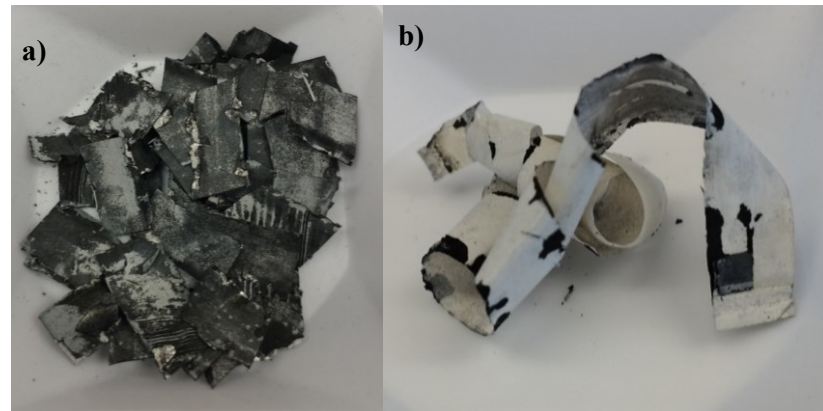


Figure 24. FTIR spectra of the process exhaust gas-emission at various process times with a CO₂ density of 715 kg/m³ a) after and b) before the collection of the extract.

The sample was manually separated into the cathode, anode, and separator materials after the extraction process. On the surface of the cathode and separator material, a white residue was clearly observed as seen in Figure 25. The FTIR peaks of the surface of the cathode and separator material match the vibrational peaks of EC.



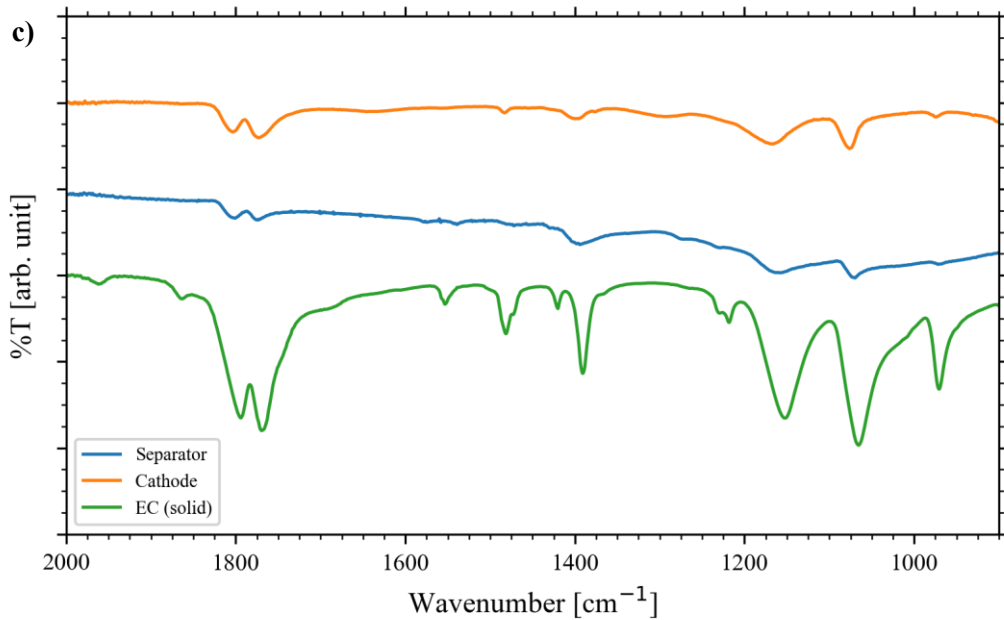


Figure 25. a) Cathode and b) separator material after the extraction process. c) ATR-FTIR spectrum of the surface of the cathode and separator material and EC in solid phase as a reference.

5.2. Solubility of ethylene carbonate in scCO₂

As shown in the previous chapter, the non-polar linear carbonates (DMC, and EMC) can be successfully extracted while the extraction of EC was limited. Thus, to improve the extraction of EC, this section focusses on the solubility of EC in CO₂. Solubility data is necessary to select the pressure and temperature conditions for the scCO₂ extraction process. To extract the compound of choice, the compound needs to be soluble in scCO₂. The solubility of EC in scCO₂ was determined at different pressure conditions (80, 100, 120, 140, and 160 bar) at the isothermal temperature of 40°C and 60°C, respectively. The results are stated in Table 3 and plotted in Figure 26. An increase of EC solubility in scCO₂ was observed in the range from 0.24 g/kg CO₂ to 8.35 g/kg CO₂ when the pressure was increased. Under the same pressure conditions, the determined solubility values were higher at 40°C compared to 60°C.

Table 3. Experimental solubilities of ethylene carbonate in supercritical carbon dioxide based on the results presented in Figure 1 and Figure S2. ^a Uncertainty of the temperature, and pressure was 2°C, and 5 bar, respectively. ^b Density data was taken from the NIST Chemistry WebBook [83]. ^c Slope (g/kg CO₂) of the linear regression. ^d Uncertainties (±) refer to the standard error of the linear regression coefficient.

Temperature ^a (°C)	Pressure ^a (bar)	CO ₂ density ^b (kg/m ³)	Solubility (g/kg CO ₂)	Mole fraction solubility (x10 ⁻³)
40	80	277.9	0.24 ^c ± 0.02 ^d	0.12
	100	628.6	3.5 ± 0.2	1.74
	120	717.8	4.8 ± 0.2	2.37
	140	763.3	6.4 ± 0.3	3.17
	160	794.9	8.4 ± 0.5	4.17
60	80	191.6	0.56 ± 0.09	0.28
	100	289.9	0.50 ± 0.03	0.25
	120	434.4	1.7 ± 0.2	0.86
	140	561.4	3.6 ± 0.3	1.78
	160	637.5	5.5 ± 0.4	2.75

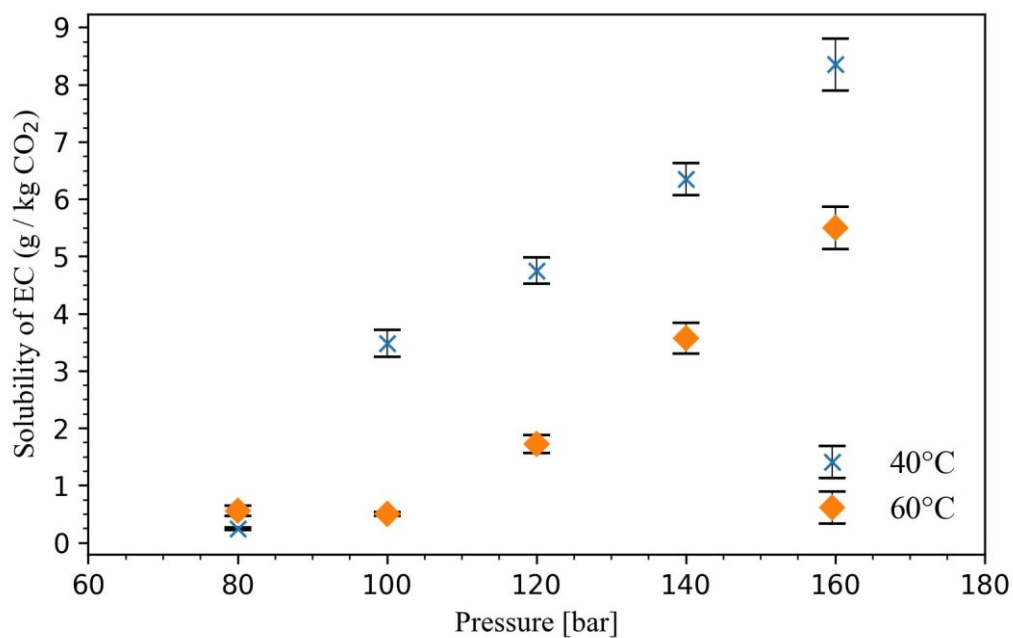


Figure 26. Solubility of EC in scCO₂ at different pressures (80, 100, 120, 140 bar, and 160 bar) at isothermal temperature (40°C, and 60°C) conditions. The uncertainty bars represent the standard error of the linear regression slope coefficient.

The experimental solubility data was fitted to the Chrastil model (Eq. (1)) using the *curve_fit* function in Python. The standard deviation of the parameter k was determined based on the square root of the corresponding diagonal element of the covariance matrix. The fitting parameters are provided in Table 4. The Chrastil model fitted well the solubility data with R^2 -values of 0.9992, and 0.9998, respectively, as shown in Figure 27. The average association number, k, was quite similar (4.3, and 4.0, respectively) at both temperature conditions. Parameter A and B were a magnitude higher at 60°C.

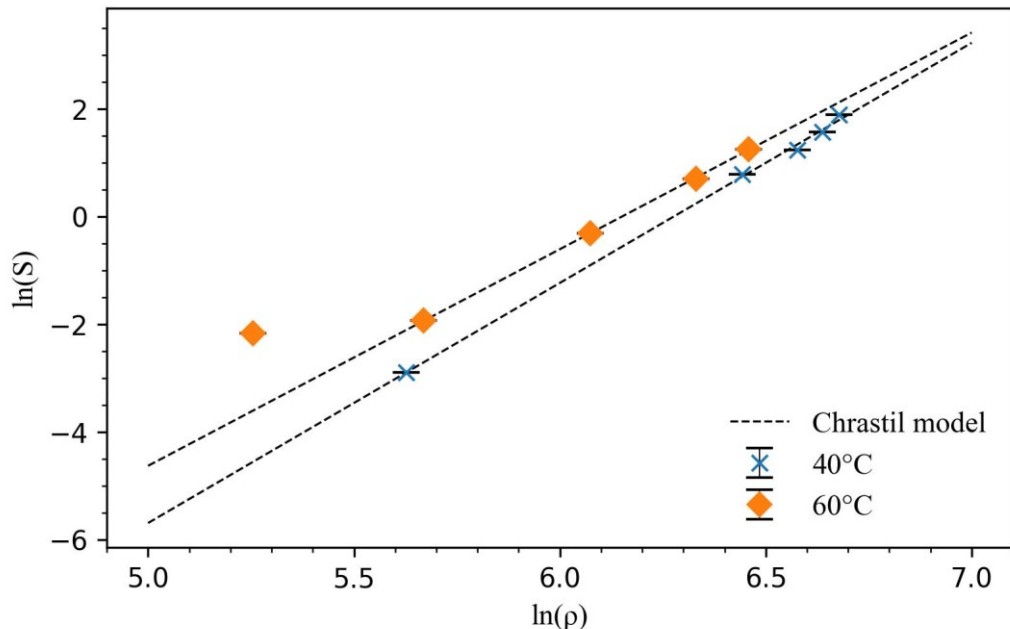


Figure 27. Correlation between the experimental and correlated solubility data using the Chrastil model.

Table 4. Fitting parameters obtained for the Chrastil equation and the R^2 value of the fit.

Temperature (°C)	A	B	k	R^2
40	84329	-296	4.3 ± 0.3	0.9992
60	506275	-1544	4.0 ± 0.4	0.9998

5.3. ScCO₂ extraction behavior of electrolyte solvents from LiB black mass

The LiB black mass used in this section was provided by an industrial partner. The black mass was produced using general pre-treatment steps including pre-shredding, magnetic separation, air separation, vibration separation, and dust recovery to remove casing, separator and electrode materials.

As a first step, the residual electrolyte content in the LiB black mass was analyzed using TGA, GC-MS, and ICP-OES. TGA was used to determine the weight percentage of residual electrolyte based on the mass loss between room temperature and 150°C, which includes solvent removal and LiPF₆ degradation. The mass loss at 150°C was 5.7 ± 0.5 wt%, which corresponds to 57 ± 5 mg of electrolyte per g of black mass as seen in Figure 28. However, the hygroscopic nature of black mass may have caused moisture absorption, potentially affecting the TGA results.

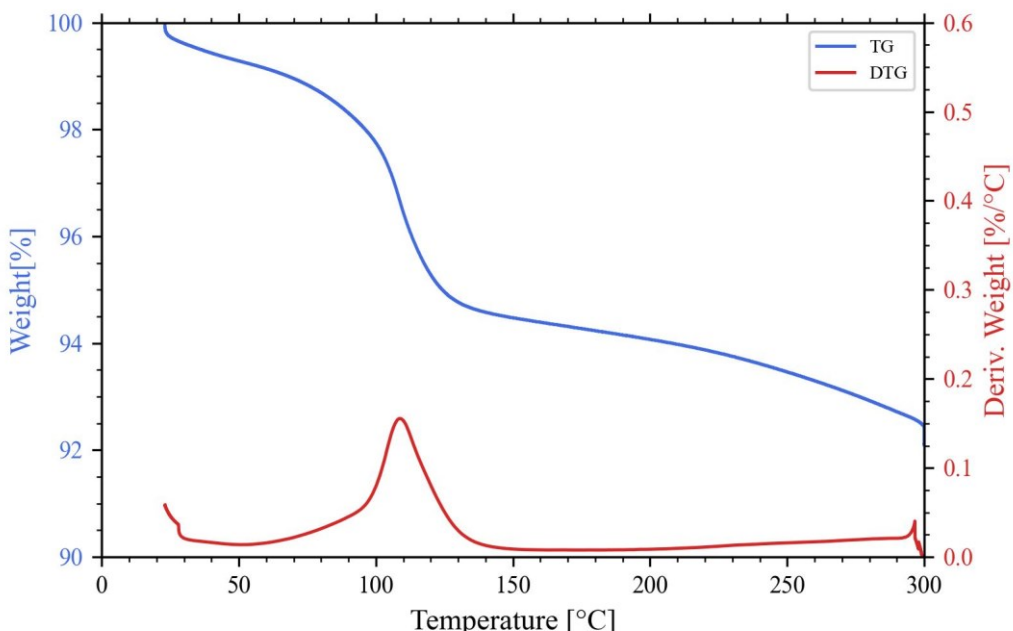


Figure 28. Thermogravimetric (TG, blue) and differentiate thermogravimetric (DTG, red) curves of the initial black mass prior the extraction process.

Acetonitrile was then used to extract the remaining electrolyte solvents in the black mass sample. The solution was analyzed using GC-MS, and ICP-OES. The key compounds in the GC-MS chromatogram were identified as DMC, EMC, DEC, EC, PC, and biphenyl, with their quantities listed in Table 5. It can be observed that mainly non-volatile electrolyte solvents (EC, PC, and biphenyl) remained in the black mass, whereas the volatile fraction (DMC, EMC, and DEC) was low. The content of LiPF₆ was estimated based on the Li (0.71 ± 0.01 mg/g), and P (3.2 ± 0.3 mg/g) content in the solution measured via ICP-OES. The mass ratio between P and Li was slightly higher (4.75) compared to the theoretical mass ratio in LiPF₆. More detailed information about the residual electrolyte characterization can be found in Paper IV.

Table 5. Estimated electrolyte solvent content (mg) per g of black mass of DMC, EMC, DEC, EC, PC and biphenyl based on the GC-MS, and ICP-OES analysis of the acetonitrile extraction. ^a Average of 5 samples. ^b Uncertainty (\pm) is expressed as the standard deviation (1σ) of 5 extraction samples. ‘Other’ corresponds to the differences between quantified compounds and total electrolyte content determined by TGA analysis.

	Content (mg/g)
DMC	0.12 ^a \pm 0.05 ^b
EMC	0.5 \pm 0.1
DEC	0.25 \pm 0.05
PC	1.6 \pm 0.1
Biphenyl	0.6 \pm 0.1
EC	22 \pm 1
LiPF ₆	15.4 \pm 0.3
Other	16 \pm 5

After identifying the residual electrolyte content and composition in the black mass sample, the extraction behaviour of the residual electrolyte components was studied at two different pressure conditions (100 bar, and 140 bar) at 40°C. After the scCO₂ extraction, the extraction yield of the residual content in the black mass was determined using TGA analysis and acetonitrile extraction and the results are stated in Table 6. At 100 bar the volatile electrolyte solvents DMC, EMC, and DEC were extracted with an extraction yield exceeding 99%. The non-volatile but non-polar biphenyl was extracted with 97%. EC, and PC were only partly extracted, reaching an extraction yield of less than 60, and 50%, respectively. However, raising the pressure to 140 bar, the extraction yield of EC, and PC increased to 95%, and 98%, respectively. Additionally, it can be observed that less than 5% of LiPF₆ was extracted at both conditions.

Table 6. Extraction yields for the different electrolyte components obtained at 100 bar and 140 bar at 40°C.

Electrolyte component	Extraction yield (%)	
	@100 bar	@140 bar
DMC	>99	>99
EMC	>99	>99
DEC	>99	>99
PC	<50	>98
Biphenyl	>97	>98
EC	<60	>95
LiPF ₆	<5	<5
Other	>60	>75
Total	>46	>65

The extraction behaviour of DMC, EMC, DEC, PC, and biphenyl at 100 bar, and 140 bar was analyzed in the following. Therefore, the cumulative yield was plotted over the relative passed CO₂ amount as seen in Figure 29, whereas the extraction behaviour of EC is plotted in Figure 30. It can be observed that the extraction behaviour of DMC, EMC, and DEC are rather similar at both pressures, and the cumulative extraction yield levels off after the first sampling point before reaching their maximum yield.

The extraction curve of EC, and PC at 100 bar are linear over the entire extraction period. However, the linear extraction curve can be divided into two parts as the slope decreases slightly after 15 g CO₂/g of black mass. This overlaps with the passed CO₂ amount at which the non-volatile electrolyte solvents (DMC, EMC, and DEC) reached their maximum extraction yield. At 140 bar, the extraction behaviour of EC, and PC cannot be directly linked to the presence of DMC, EMC, and DEC in the extraction chamber. After a linear extraction period, the extraction curve of EC, and PC levels off after approximately 7g CO₂/ g black mass, and 3g CO₂/ g black mass, respectively, before approaching their maximum extraction yield.

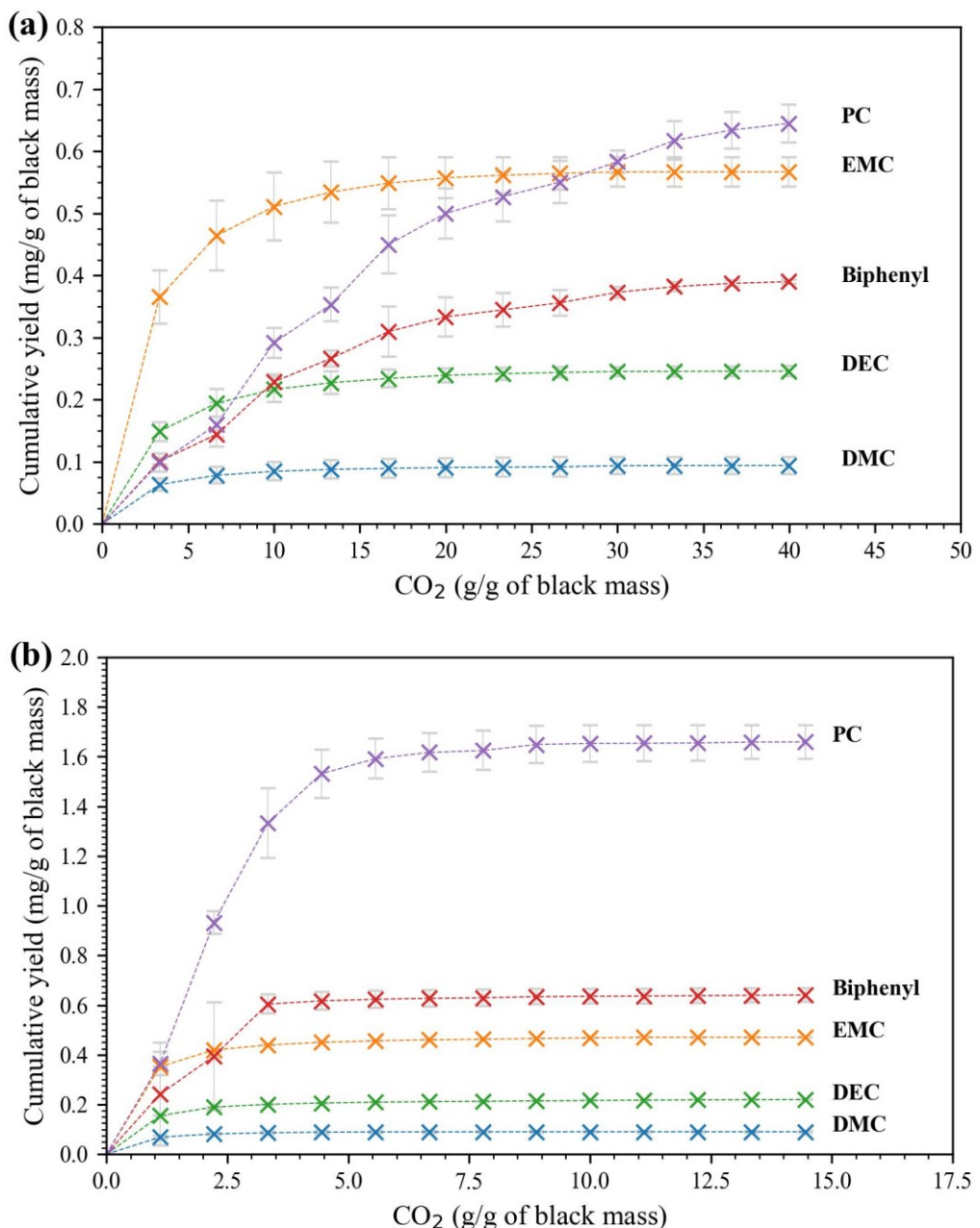


Figure 29. Cumulative extraction curve of DMC, EMC, DEC, biphenyl, and PC at a) 100 bar and 40°C and b) 140 bar and 40°C. The dashed lines in the graphs describe the trend of the extraction curve. The uncertainty bars in the plot represent the standard deviations (1σ) of the triplicates at each measurement.

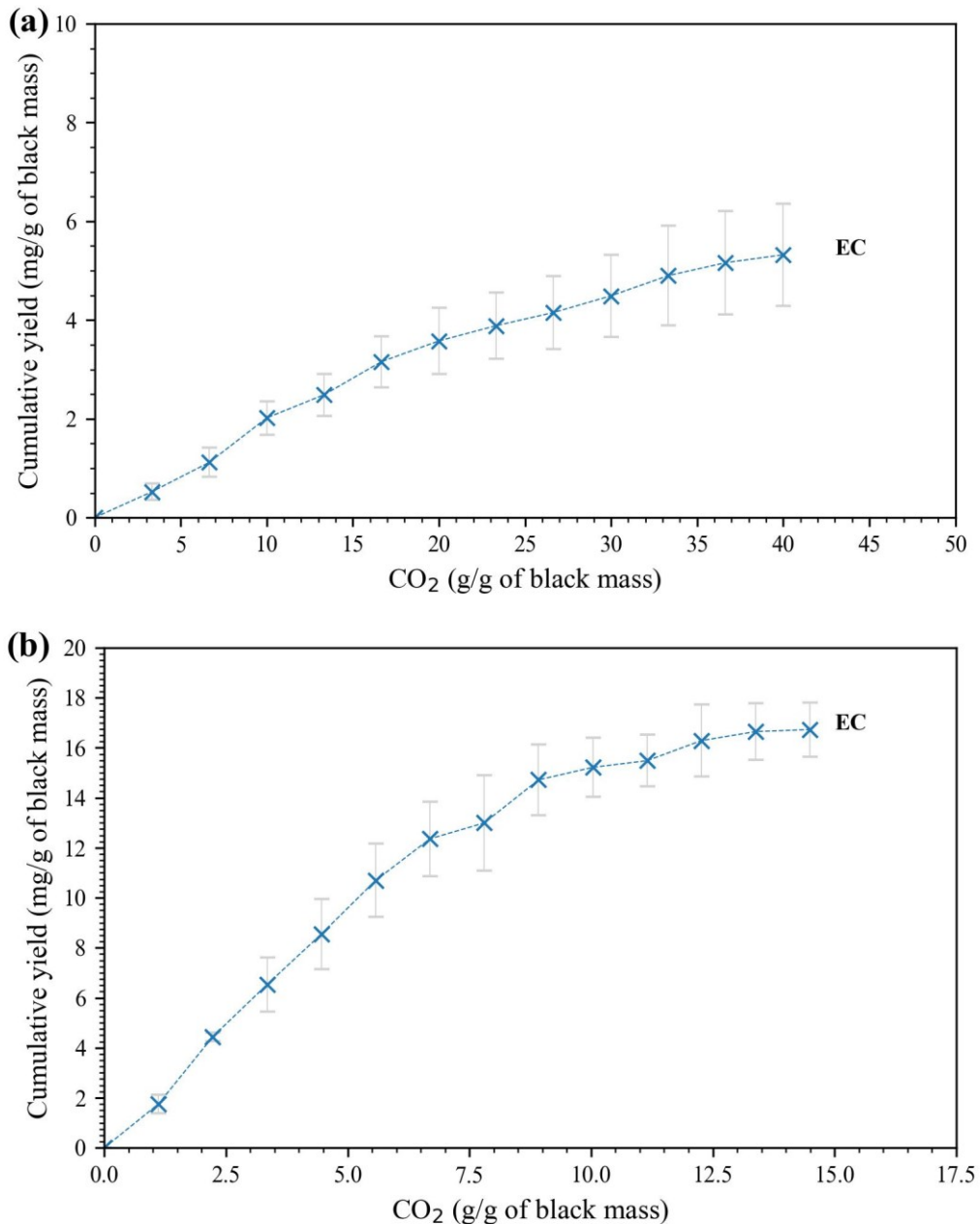


Figure 30. Cumulative extraction curve of EC at a) 100 bar and 40°C and b) 100 bar and 40°C. The dashed lines in the graphs describe the trends of the extraction curves. The uncertainty bars represent the standard deviation (1σ) of the triplicates.

The mass load of the black mass in the extraction chamber was varied (3, 6, and 9g) to check whether the extraction curves of EC, and PC at 140 bar and 40°C represent an equilibrium extraction curve and the corresponding plots are given in Figure 31 [80]. It can be observed that the slope of the linear part of the extraction curves increased with raising mass loads. Also, an overall higher cumulative yield for EC was reached at 9 g compared to 3 g, and 6 g.

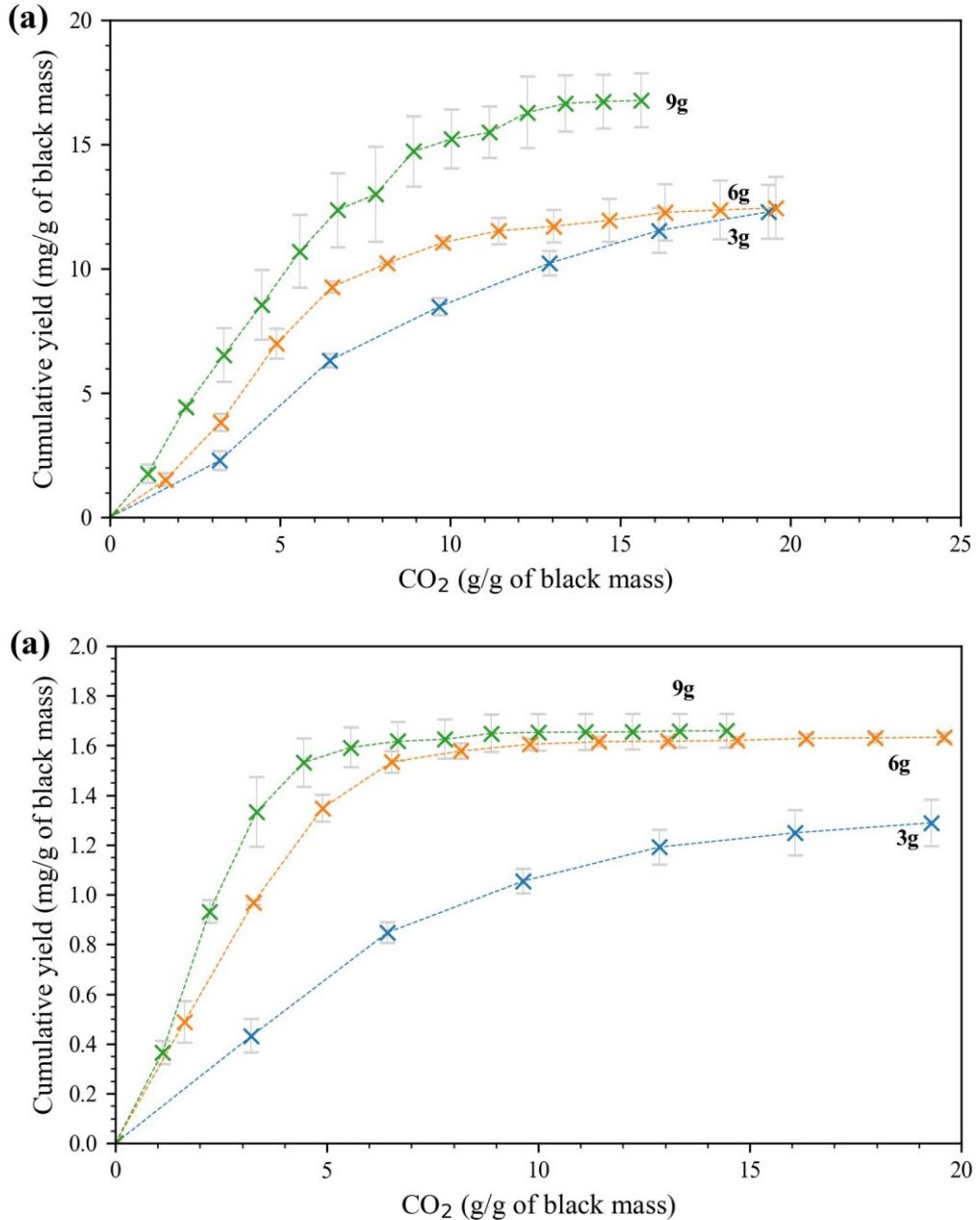


Figure 31. Extraction curves of a) EC and b) PC at different mass loads (3g, 6g, and 9g) of black mass inside the extraction chamber. The uncertainty bars represent the standard deviation (1σ) of the triplicates. The dashed lines indicate the trend of the curves.

The extraction curves of EC, and PC obtained at a mass load of 9 g were fitted using the Type D model equations described in the section 3.3 and the results are plotted in Figure 32. Eq. (11) was used to fit the first straight part of the extraction curve to determine the equilibrium constant y_0 for EC, and PC. The second part of the extraction curve was fitted using Eq. (3) by adjusting the fitting parameters C_1 , and C_2 . The *curve_fit* function included in the Python module *scipy.optimize* was used to determine the optimized model parameters stated in Table 7. The square root of the diagonal element of the covariance matrix corresponding to the fitting parameter was used to determine the standard deviation (1σ).

Eq. (12) was then used to estimate the easily accessible solute fraction, r , from the fitting parameter C_1 , and C_2 , as well as the crossing-point of the two sections of the extraction curve, q_c . The partition coefficient, K , was then estimated using Eq. (11). Finally, Eq. (13) was used to estimate the solid-phase mass transfer coefficient, k_{sa} . The fitting parameters used for the calculations are stated in Table 7 along with the estimated values for r , K , and k_{sa} . The uncertainties for these were calculated from the fitting parameter uncertainties of y_0 , C_1 , and C_2 using the Gaussian error propagation.

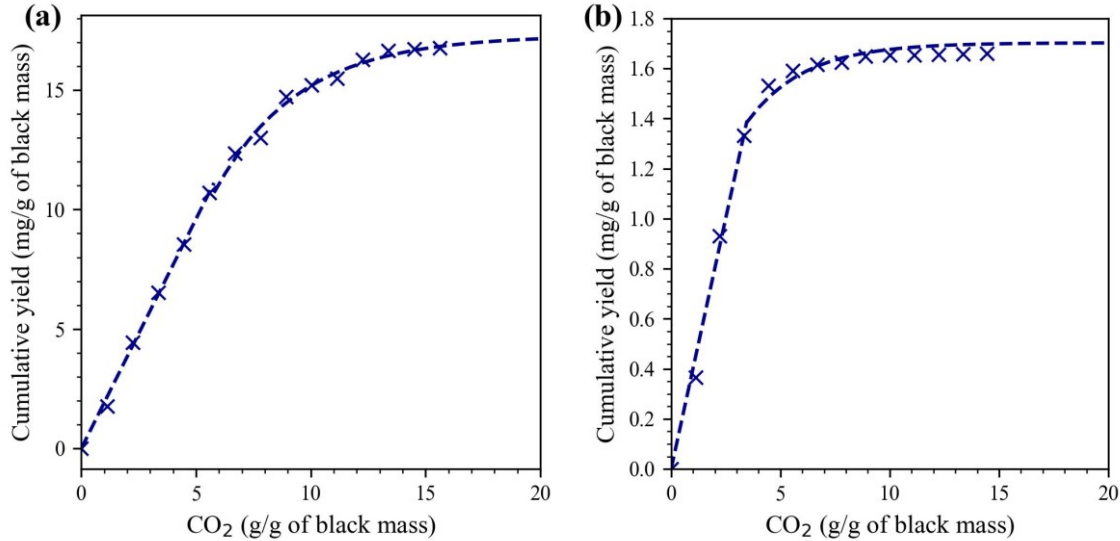


Figure 32. Modelled extraction curve of a) EC, and b) PC at 140 bar and 40°C using the model parameters stated in Table 7.

Table 7. Model parameters used to fit the extraction curves with Type D model suggested by Sovová.

Model parameter	EC	PC
q_c (g CO ₂ /g black mass)	5.78	3.46
y_0 (mg/g CO ₂) ^a	1.92 ± 0.02	0.40 ± 0.03
C_1	1.811 ± 0.299	0.696 ± 0.187
C_2	0.270 ± 0.20	0.380 ± 0.062
r	0.61 ± 0.08	0.81 ± 0.06
K	0.137 ± 0.004	0.34 ± 0.03
k_{sa} (s ⁻¹)	0.089	0.019

6. Discussion

In this chapter, the results presented in the previous chapter will be discussed in three parts. The first part compares the two different processes to recover the electrolyte from spent LiB cells – low temperature thermal treatment and sub-and scCO₂ extraction. The second part discusses the solubility of EC in CO₂. In the last part of the discussion chapter, the extraction behavior of the residual electrolyte solvents from LiB black mass using scCO₂ extraction will be discussed.

6.1. Electrolyte recovery from untreated LiB cells using thermal treatment and scCO₂ extraction

In Part I of the result section two different approaches – low temperature thermal treatment and sc-CO₂ extraction, were used to recover the electrolyte from untreated spent LiB pouch cells. Based on the FTIR and TGA results, the electrolyte composition was based on DMC, EMC, EC, and LiPF₆. First the results of the thermal treatment approach will be discussed, followed by the discussion of the results of the sub-scCO₂ extraction process. Finally, both approaches will be compared with each other.

In the low temperature thermal treatment process, a weight loss of 13.9 ± 0.1 wt% was observed at 130°C after 3 hours. The weight loss of the electrode stack was associated with the amount of electrolyte removed using the corresponding process. An increase in temperature to 150°C did not further enhance the separation of the electrolyte as seen in Figure 12.

The separated electrolyte components were collected in two different phases, solid and liquid phase. The collected liquid product was composed of DMC, EMC, and smaller amounts of EC as revealed by GC-MS analysis plotted in Figure 13. EC, in turn, was mainly recovered as solid condensate from the walls of the quartz tube outside the heating zone of the tube furnace. At this position of the tube furnace, EC crystallized as the temperature was lower than its melting point of 36.5°C. The high melting point of EC allows for its direct separation from other lower melting point electrolyte solvents like DMC, and EMC. However, it can also be a challenge as at room temperature it also might block the pipelines of an industrial plant.

The low temperature thermal treatment process successfully separated the electrolyte solvents (DMC, and EMC) at all process temperatures. This was confirmed by the disappearance of the DMC and EMC emissions in the exhaust gas after 80 minutes at 130°C and 150°C. According to literature, at temperatures above 180°C, DMC, EMC and EC eventually decompose into CO₂, carbon monoxide (CO), ethene (C₂H₄), and dimethyl ether (C₂H₆O) [88]. However, these compounds were not detected in the exhaust gas, indicating that DMC, EMC and EC did not degrade during process.

In the theory section, the degradation mechanism of LiPF₆ at elevated temperatures was described. The analysis of the process exhaust gas revealed that LiPF₆ degradation occurred at all temperature settings, as confirmed by the presence of HF and POF₃. The characteristic peaks of the anhydrous LiPF₆ decomposition product PF₅ at 1018 cm⁻¹ and 946 cm⁻¹ overlap with the vibrational peaks of the organic solvents and therefore difficult to identify with certainty [36]. Nonetheless, the formation of PF₅ during the process cannot be excluded. Time-resolved analysis of the HF and POF₃ peaks in the exhaust gas further indicated that LiPF₆ fully decomposed at process conditions above 130°C after 70 minutes as their peak intensities

plateaued. However, POF_3 peaks were detectable at 90°C, and 110°C throughout the entire process time, suggesting an incomplete decomposition. This observation aligns with literature studies showing a weight loss of LiPF_6 to 17 wt%, the proportion of LiF , at temperatures up to 150°C as measured by TGA [83]. Notably, the standard deviation of the triplicate measurements decreased as the temperature increased, suggesting incomplete degradation of LiPF_6 at process temperatures below 130°C. The moisture/humidity responsible for the hydrolysis of LiPF_6 was likely absorbed into the LiB sample during the cell disassembly, sample preparation, and cell storage at -18°C. The presence of F^- and PO_4^{3-} in the gas washing water reveals that hydrofluoric acid and phosphoric acid were formed after the reaction of HF and POF_3 with H_2O according to equations 2 and 3. Hydrofluoric acid and phosphoric acid can be considered as process by-products and potentially reutilized. However, more research into this is required.

Moving to the results obtained using scCO₂ extraction, it can be observed that the maximum electrolyte extraction yield of 66% was achieved at 80 bar and 29°C. Above 80 bar, the effect of increasing pressure up to 120 bar was minimal. A more pronounced effect on the extraction yield was observed with varying the temperature. Below 29°C, the extraction yield was constant within the uncertainty of the triplicates. In turn, increasing the temperature resulted in a linear decrease in extraction yield. Similar temperature effects were reported by Mu et al. [69] at 70 bar, while using an electrolyte-soaked separator (EC, PC, DMC, EMC) as extraction medium. At 250 bar the extraction yield slightly increased while raising the temperature from 30°C to 50°C as reported by Liu et al. [67].

As described in more detail in section 3.1, the solvation characteristics of scCO₂ are highly related to the process density as the specific solvent-solute interaction probability increases with raising CO₂ density [74]. The observed temperature effect on the extraction yield reflects the dependence on the CO₂ density. The effect of the CO₂ density on the extraction yield is also highlighted in Figure 21. The maximum electrolyte separation yield of 66% was determined at CO₂ densities between 600-900 kg/m³.

Analysis of the collected extract using GC-MS revealed DMC, and EMC as the main constituents, whereas EC was only present in minor amounts (<10%) at all studied conditions. It is worth noting that the extract collection yield was around 60% and the plotted composition in Figure 23 is not representative of the actual extraction composition. In the cold trap exhaust gas, vibrational peaks corresponding to DMC, and EMC were observed, whereas EC peaks were not detected. Thus, it is believed that the actual share of extracted EC was lower than indicated in Figure 23. Mainly DMC, and EMC were extracted from the LiB electrode stack sample at the studied temperature and pressure conditions. As shown in Figure 25 remained in the electrode stack after the extraction process. The findings are in alignment with the study by Grützke et al. [65], which reported that only DMC, and EMC were quantitatively recovered from aged 18650 cells using liquid (60 bar, 25°C), and supercritical (300 bar, 40°C) CO₂, whereas the extraction EC was limited. In contradiction to these results, Liu et al. [67] reported high extraction yields (> 89%) of EC at pressures between 150 and 350 bar and temperatures between 30 and 50°C. In their work, Liu et al. used an ordinary polypropylene separator soaked with electrolyte as an extraction medium. However, in this work the electrolyte was extracted from spent LiB pouch cell electrode stack samples, whereas Grützke et al. used aged 18650 LiB cells. In a different study Grützke et al. [64] reported higher EC extraction yields from a

polyethylene ethylene fleece separator compared to a porous glass fiber separator with a polar surface. This implies that the extraction of EC depends highly on the extraction matrix.

The electrolyte extraction behaviour in this study in respect to temperature and pressure conditions can be correlated to the binary liquid-vapor equilibrium (LVE) phase diagrams of DMC-CO₂ [89–94], EMC-CO₂ [89] published in literature. Extraction conditions are favored at which the solute and solvent exist in a single phase. The LVE phase behavior of both compounds is rather similar. DMC and CO₂ are in a single phase at all temperatures below 40°C, at operating pressures of 80 bar and higher. However, at 80 bar, DMC and CO₂ are in the two-phase region at 45°C, and 55°C. This explains the decrease in extraction yield at these conditions. However, it must be emphasized that electrolyte is a multicomponent mixture, and the phase behavior is likely to be influenced by the other components present in the mixture. Thus, the binary LVE phase diagrams only function as an indication.

Diving into the solvation of the compounds at a molecular level it was observed that at the studied conditions, the acyclic ester carbonates (DMC, EMC) were much better extracted than the cyclic ester carbonate EC. DMC and EMC are both acyclic carbonate esters (non-polar) containing a carbonyl group (C=O) flanked by two alkoxy groups (R-O-). The CO₂ molecules are believed to form stable Lewis acid-base interactions with the carbonyl oxygen, and the ester oxygen as described in 3.1. Both molecules also have methyl groups, which strengthen these interactions through cooperative hydrogen bonding. Besides its higher polarity compared to DMC and EMC, the lower extraction yield of EC might be also explained by the limitation for CO₂ molecules to cluster around the EC molecule to eventually form stable solvation coordination's at the studied pressure conditions. A higher solubility of CO₂ in linear carbonates (DMC, EMC, DEC) compared to cyclic carbonates (EC, PC) at atmospheric pressure was reported in literature [95]. According to literature, the carbonyl group of the EC molecule coordinates extensively with the Li⁺ cation, whereas DMC, and EMC are pushed into the outer solvation sphere [96]. The occupation of the CO₂-philic carbonyl group of the EC molecule may potentially further limit its coordination with the CO₂ molecule and thus its extraction in scCO₂.

Analysis of the exhaust gas and elemental analysis of the collected extract indicate that LiPF₆ did not decompose during the process as vibrational peaks corresponding to HF and POF₃ were not observed in the exhaust gas. Moreover, the amount of phosphorous in the collected extract corresponded to only a trace amount of LiPF₆ (<1.2%) estimated based on a LiPF₆ concentration of 1 M. It is likely that the phosphorous present in the extract originated from electrolyte aging products such as DMFP and EMFP, which were detected in the GC-MS analysis.

The electrolyte extraction yield was lower for the sub-scCO₂ extraction process compared to the thermal treatment process. This is because EC, and LiPF₆ were not recovered at the studied conditions. Despite its lower extraction yield, the biggest advances using scCO₂ extraction compared to thermal treatment are the generated gas emissions during the process. As shown in this section LiPF₆ decomposes during the thermal treatment while producing HF, and POF₃. In turn, LiPF₆ can be potentially recovered intact from LiB waste using scCO₂ extraction as it did not decompose during extraction. This makes scCO₂ extraction a more favourable process compared to thermal treatment as the decomposition of LiPF₆ and the corresponding toxic gas

emissions can be avoided. However, more research is required to increase the extraction yield of EC and LiPF₆.

6.2. Solubility of ethylene carbonate in scCO₂

Section 6.1 showed that the polar electrolyte solvent EC was only extracted in trace amounts at the studied conditions (15 - 55°C, 60 - 140 bar). However, EC contains a CO₂-philic carbonyl bond which promotes the dissolution in CO₂ as discussed in the previous section. Thus, it was believed that by tuning the pressure and temperature conditions, the solubility of EC in scCO₂ can be enhanced and successfully extracted without the support of a co-solvent. Using a co-solvent can have negative effects on the extract as it will be mixed with the co-solvent in the separator. Further steps are then required to separate the co-solvents from the extract to achieve co-solvent free extracts [58].

The solubility of EC in scCO₂ obtained by the gravimetric flow-through method increased from 0.24 g/kg CO₂ to 8.35 g/kg CO₂ while raising the pressure from 80 bar to 160 bar at 40°C. At 60°C, the solubility values of EC were lower under the same pressure conditions. This indicates that the studied pressure range was below the cross-over pressure and the CO₂ density was the dominating factor to dissolve EC [60,74].

The experimental solubility data correlated well to the Chrastil model in the studied pressure range except for the solubility data point corresponding to 80 bar and 60°C. The determined solubility at this point (0.56 g/kg CO₂) was very similar to the solubility determined at 100 bar and 60°C (0.50 g/kg CO₂). Based on their similarity it was believed that the point determined at 80 bar and 60°C was an experimental error. Thus, this point was excluded to fit the Chrastil model to experimental solubility data.

Constant k, representing the average equilibrium association number of the pseudo solvato-complex, was quite similar for both temperatures with 4.28, and 4.02 at 40°C, and 60°C, respectively. This means that on average 4 CO₂ molecules solvate the EC. The constants A and B were a magnitude higher at 60°C compared to 40°C indicating a higher enthalpy of solvation [77].

6.3. ScCO₂ extraction behavior of electrolyte solvents from LiB black mass

The residual electrolyte content in the LiB black mass was determined to be 57 ± 5 mg/g of black mass. The fraction of low volatile solvents (DMC, EMC, DEC) was low compared to the fraction of non-volatile components (EC, PC, biphenyl). In a fresh electrolyte solution, EC is blended with approximately 50-70% of DMC, EMC, and/or DEC [29]. It was assumed that the majority of DMC, EMC, and DEC evaporated due to their volatile nature during the shredding, and physical separation stages to produce the black mass.

Two pressure conditions, 100 bar and 140 bar, at 40°C were compared to extract the electrolyte solvents from the black mass sample. An overall higher extraction yield was observed at 140 bar compared to 100 bar. At 100 bar, DMC, EMC, and DEC were already successfully extracted from the black mass at 100 bar and 40°C exceeding an extraction yield of 99%, respectively. As already pointed out in section 6.1, DMC, and EMC are miscible with CO₂

according to their binary LVE phase diagram [89,90,97]. Thus, the full extraction of these compounds was expected under these conditions. The extraction of EC and PC was limited at 100 bar, with yields less than 60% and 50%, respectively. However, increasing the pressure to 140 bar, while maintaining the same amount of CO₂ per g of black mass, resulted in a significant yield increase for EC and PC, reaching 95% and 98%, respectively. The extraction yield increase of EC at 140 bar compared to 100 bar can be related to the solubility increase at higher pressures as can be observed in section 6.2. The extraction curve for EC at 100 bar remained linear in the studied extraction period of 65 L of CO₂. Thus, the extraction yield can be potentially improved using higher CO₂ throughput and longer extraction times.

Analyzing the extraction curves at 100 bar, it was observed that the volatile non-polar electrolyte solvents (DMC, EMC, and, DEC) already level off after the first sampling point at 3.5 g CO₂/g of black mass. Then, the extraction rate decreased rapidly. The mass transfer of the solutes through the core of the particles towards the particle surface or other mass-transfer-hindering solute-matrix interactions typically slow down the extraction rate in the second part of the extraction curve [80]. As the fraction of volatile solvents was low compared to the fraction of non-volatile solvents, the extraction of the volatile substances likely occurred simultaneously with the extraction of the non-volatile substances [98]. It has been observed that the extraction rate of EC, and PC at 100 bar was dependent on the presence of DMC, EMC, and DEC in the extraction chamber. Thus, it was assumed that these solvents featured as an entrainer for the extraction of biphenyl, EC, and PC at 100 bar.

A similar extraction behavior for DMC, EMC, and DEC was observed at 140 bar. Again, the extraction curve levels off after the first sampling point. The extraction curve of biphenyl was linear until the maximum extraction yield was reached. The linear part, representing the apparent solubility, showed an extraction rate of 0.18 mg/g CO₂, which corresponds to mole fraction of 5.1×10^{-6} . The mole fraction solubility of biphenyl at 40°C has been reported as 8.73×10^{-3} and 1.11×10^{-2} at pressures of 119 bar and 149 bar, respectively [99]. This shows that the apparent solubility was 4 orders of magnitude lower than the solubility values found in literature. The determined apparent solubility of EC was 1.9 mg/g CO₂ and for PC was 0.4 mg/g CO₂. The apparent solubility of EC was lower than the solubility reported in Table 3 (6.4 g/kg CO₂). The lower values of apparent solubility compared to the thermodynamically solubilities reported in literature indicate that solute-matrix interactions dominate the extraction process and that the CO₂ was not saturated during the extraction process [80]. To overcome the solute-matrix interactions, larger residence times are required to achieve equilibrium [98]. The extraction rate of EC at 140 bar was linear until 7.5 g CO₂/g of black mass. While extracting 70% of the EC in the black mass. Then, mass transfer of the solutes from the core of the particle to the particle surface slows down the extraction rate until reaching the maximum extraction yield at less than 15 g CO₂/g of black mass. This indicates that 50% of the consumed CO₂ was required to extract the remaining 30% of EC in the black mass. Thus, a limiting factor for the extraction of EC from LiB waste is the diffusion-controlled mass-transfer. To get an estimate for the solid-phase mass transfer coefficient, the extraction curves of EC, and PC can be modelled using the Sovová model shown in section 3.3.

The mass load of the black mass was varied from 3, 6, to 9 g to investigate whether the extraction curves of EC, and PC are equilibrium extraction curves. This is the case, when the linear part of the extraction curves overlap [80]. The linear part of the extraction curves for 3, 6, and 9 g did not overlap, and the slope ratio for EC was 1.5 from 3 to 6 g, and 1.4 from 6 g

to 9 g. Thus, the extraction curves are not equilibrium extraction curves. The extraction chamber was fully loaded with the black mass at 9 g, and the mass load could not be further increased. Also, the limits of the lowest achievable flowrate were reached, so the lower limit of residence time of CO₂ in the extraction chamber was reached using dynamic extraction. Despite not representing equilibrium extraction curves, the extraction curves of EC, and PC using 9 g of black mass were fitted using the general Sovová model discussed in the section 3.3 to get an estimate of the underlying solid-phase mass-transfer coefficients.

The extraction curves belong to Type D, as the first part of the extraction curve consist only of one straight part, and as described previously, the apparent solubility is lower than the thermodynamic solubility. The easily accessible solute fraction, r, of EC was estimated to be 61%, whereas for PC 81%. The partition coefficient, K, was estimated to be 0.137 for EC, and 0.34 for PC, and the solute-phase mass-transfer coefficient was estimated to be 0.089 s⁻¹ for EC, and 0.019 s⁻¹ for PC.

Despite being polar, EC and PC were successfully extracted using scCO₂ without the addition of a co-solvent. Both compounds are carbonate esters containing a carbonyl group (C=O) flanked by two alkoxy groups (R-O-). As described in section 3.1, the carbonyl oxygen is CO₂-philic, and thus prone to form stable solvation configurations with the carbon atom of the CO₂ molecule via Lewis acid-base interactions. Whereas, the non-polar carbonate esters DMC, EMC, and DEC are miscible in CO₂ at 100 bar and 40°C [89,90,97], the solubility of EC, and PC are relatively low, but still increases with raising pressure as discussed in section 6.2. The better solubility of DMC, EMC, and DEC in CO₂ can be explained due to the presence of the methyl group attached to the alkoxy group. A cooperative hydrogen bonding between the oxygen atom of the CO₂ molecule and H-atom of the methyl group strengthens the interaction of both stable solvation configurations introduced in section 3.1.

In section 6.1, it was observed that the extraction of EC was very limited at 80 bar and 29°C, whereas DMC, EMC, and DEC were successfully extracted due to their miscibility in CO₂ [89,90,97]. The low extraction of EC can be correlated with its low solubility at these conditions. The solubility data in section 6.2 showed that higher pressures are required to dissolve EC in CO₂. The tunable solubility of the polar carbonates EC, and PC in CO₂ with pressure and temperature is predestined for their selective extraction from the LiB waste or fractionation from the non-polar carbonate esters during the collection process [58].

7. Conclusion

The thesis compared two approaches to recycle the electrolyte from LiB waste – low temperature thermal treatment and scCO₂ extraction. Low temperature thermal treatment enables the full separation of the electrolyte solvents DMC, EMC, and EC at 130°C for 80 minutes under N₂ atmosphere. However, using this approach LiPF₆ cannot be recovered intact as it decomposes to LiF, HF, and POF₃ at elevated temperatures. The decomposition leads to toxic gas emissions, which are a potential threat for the work environment and subsequent special treatment of the off-gas is required.

ScCO₂ extraction is favorable to low temperature thermal treatment as it enables the separation of electrolyte solvents from LiB waste with minimal toxic gas emission as no evidence of LiPF₆ degradation was observed. Furthermore, it was shown that the tunable solvation characteristics of scCO₂ can be used to fractionate the key electrolyte solvents based on temperature and pressure conditions. LVE phase diagrams of DMC, EMC, and DEC indicate their miscibility in CO₂ at 80 bar and 29°C. The results presented in this thesis show that 80 bar and 29°C are suitable to extract effectively the non-polar electrolyte components DMC, and EMC from LiB waste. The extraction of the polar electrolyte components, EC, and PC required higher pressure conditions. The limited extraction of EC at 80 bar at various temperatures can be related to its low solubility at these conditions, which was determined to be 0.24 g/kg CO₂. Raising the pressure to 140 bar, increases the solubility of EC in CO₂ to 6.4 g/kg CO₂. At 140 bar and 40°C, the polar electrolyte solvents EC, and PC were successfully extracted from LiB waste using less than 15 g of CO₂/g black mass. The limiting factor in the extraction of the electrolyte solvents, especially for EC, was the diffusion-controlled mass transfer, which dictates the required extraction time and results in a higher CO₂ throughput. The solid-phase mass transfer coefficients of EC, and PC were determined to be 0.089 s⁻¹ and 0.019 s⁻¹, respectively.

Future Work

The research results presented in this thesis show the huge potential to implement scCO₂ extraction to recover the electrolyte from LiB waste. However, a few more points need to be studied.

The results showed the limitation of the scCO₂ extraction on solute-matrix interactions. This slows down the overall extraction process and implies the dependence on residence time of CO₂ in the extraction chamber. Thus, further studies are required to optimize the residence time to acquire more effective electrolyte recycling in terms of CO₂ consumption and extraction time.

The experimental set-up used in this study was limited to 160 bar. Higher pressures can lead to a higher solubility and thus to higher extraction rates. Further experiments to compare the mass-transfer mechanism based on the extraction curves with different pressure and temperature conditions might be useful to optimize the effectiveness of the extraction in terms of CO₂ consumption and extraction time.

The results presented in this thesis proof that the non-polar and polar electrolyte solvents can be successfully extracted from different LiB waste materials. However, LiPF₆ was not extracted at the studied conditions. A co-solvent is required to be able to solubilize LiPF₆ and separate it from the LiB waste. Thus, further investigation must be done to select a potential co-solvent, pressure and temperature conditions.

In this study only lab-scale experiments were conducted. More research is required to optimize the process conditions on larger scales to eventually upscale the process.

After completing the upscaling, a techno-economic analysis of the scCO₂ extraction process is required to investigate the feasibility and cost effectiveness compared to other existing recycling techniques such as conventional solvent extraction and vaporization processes.

Acknowledgments

I would like to begin by expressing my sincere gratitude to Burçak Ebin, my supervisor, for your exceptional mentorship, guidance, and constant support from the very start of this journey. Your insightful feedback, and openness to discussions of all kinds have been incredibly important to my development. The patience and encouragement you've shown, especially during the more challenging phases, have kept me motivated and focused.

I am also grateful to Marina Petranikova, my co-supervisor, for your invaluable feedback and for always being there with words of motivation and reassurance. Your moral support has been incredibly important. Especially during the darker times.

I would also like to extend my gratefulness to Christian Ekberg, whose feedback and constructive criticism throughout the writing process have been essential in improving the quality of my work.

I am also extremely grateful to Séverine Camy for providing me with the opportunity to visit Toulouse, France for a research stay. The experience was incredibly valuable, and I learned a great deal during this brief period, thanks to our insightful discussions. Moreover, the research visit would not have been the same without you, Edoardo Vittorio Pasini. From day one, you made me feel like a part of the research group, and your welcoming attitude greatly enhanced my experience. I deeply appreciate the knowledge you shared and the time you dedicated to helping me out during my visit.

I want to extend my appreciation to my current and past colleagues at NC/IMR, both senior researchers and PhD students. You created a fantastic work environment, and I'm grateful for the help, expertise, and countless lunch discussions, fika breaks, and after-work gatherings. Even though my mind was often wavering around somewhere else, I did enjoy it more than you think.

My deepest gratitude also goes to my friends scattered across Gothenburg, Sweden, Germany, and various parts of the world. You all know who you are. Your friendship has been an incredible source of strength and moral support throughout this entire process. Whether it was offering moral support during moments of doubt, providing much-needed distractions, or broadening my perspective through our meaningful conversations, you have all played an essential role in shaping me to the person I am. Thank you for all the adventures, laughter, and unforgettable memories we've shared.

Last, but by no means least, I am deeply thankful to my family for their unwavering love and support. I could not have undertaken this journey without your constant encouragement. Your belief in me has been a constant source of motivation.

This work was supported by the Swedish Energy Agency Battery Fund Program (Project No:50124-10, P2019-90078), FORMAS – Swedish Research Council for Sustainable Development (Project No: 2021-01699) and Horizon Europe (Project 101069685 — RHINOCEROS). I would also like to acknowledge the Chalmers Material Analysis Laboratory, CMAL, for providing their facilities and assistance for the XRD and SEM characterization.

References.

- [1] N. Nitta, F. Wu, J.T. Lee, G. Yushin, Li-ion battery materials: Present and future, *Mater. Today*. 18 252–264. <https://doi.org/10.1016/j.mattod.2014.10.040>.
- [2] J.M. Tarascon, M. Armand, Issues and challenges facing rechargeable lithium batteries, *Nature*. 414 (2001) 359–367. <https://doi.org/10.1038/35104644>.
- [3] I.E. Agency, Global EV Outlook 2024, (2024).
<https://doi.org/https://www.iea.org/reports/global-ev-outlook-2024>.
- [4] A. Sobianowska-Turek, W. Urbańska, A. Janicka, M. Zawiślak, J. Matla, The Necessity of Recycling of Waste Li-Ion Batteries Used in Electric Vehicles as Objects Posing a Threat to Human Health and the Environment, *Recycling*. 6 (2021) 35. <https://doi.org/10.3390/recycling6020035>.
- [5] N.P. Lebedeva, L. Boon-Brett, Considerations on the Chemical Toxicity of Contemporary Li-Ion Battery Electrolytes and Their Components, *J. Electrochem. Soc.* 163 (2016) A821–A830. <https://doi.org/10.1149/2.0171606jes>.
- [6] A. Nedjalkov, J. Meyer, M. Köhring, A. Doering, M. Angelmahr, S. Dahle, A. Sander, A. Fischer, W. Schade, Toxic Gas Emissions from Damaged Lithium Ion Batteries—Analysis and Safety Enhancement Solution, *Batteries*. 2 (2016) 5. <https://doi.org/10.3390/batteries2010005>.
- [7] F. Larsson, P. Andersson, P. Blomqvist, B.E. Mellander, Toxic fluoride gas emissions from lithium-ion battery fires, *Sci. Rep.* 7 (2017) 1–13. <https://doi.org/10.1038/s41598-017-09784-z>.
- [8] P. Andersson, P. Blomqvist, A. Lorén, F. Larsson, Investigation of fire emissions from Li-ion batteries, n.d.
- [9] F. Arshad, L. Li, K. Amin, E. Fan, N. Manurkar, A. Ahmad, J. Yang, F. Wu, R. Chen, A Comprehensive Review of Advancement in Recycling Anode and Electrolyte from Spent Lithium Ion Batteries, *ACS Sustain. Chem. Eng.* 8 (2020) 13527–13554. <https://doi.org/10.1021/acssuschemeng.0c04940>.
- [10] J.A. Kinnaird, P.A.M. Nex, Critical raw materials, *Routledge Handb. Extr. Ind. Sustain. Dev.* (2022) 13–33. <https://doi.org/10.4324/9781003001317-3>.
- [11] Business Sweden, The Nordic Battery Value Chain, (2023).
- [12] C. of the E.U. European Parliament, Regulation (EU) 2023/1542 of the European Parliament and of the Council of 12 July 2023 concerning batteries and waste batteries, amending Directive 2008/98/EC and Regulation (EU) 2019/1020 and repealing Directive 2006/66/EC, (n.d.). <http://data.europa.eu/eli/reg/2023/1542/oj> (accessed January 13, 2025).
- [13] J. Marshall, D. Gastol, R. Sommerville, B. Middleton, V. Goodship, E. Kendrick, Disassembly of Li Ion Cells—Characterization and Safety Considerations of a Recycling Scheme, *Metals* (Basel). 10 (2020) 773. <https://doi.org/10.3390/met10060773>.
- [14] D. Thompson, C. Hyde, J.M. Hartley, A.P. Abbott, P.A. Anderson, G.D.J. Harper, To shred or not to shred: A comparative techno-economic assessment of lithium ion battery hydrometallurgical recycling retaining value and improving circularity in LIB supply chains, *Resour. Conserv. Recycl.* 175 (2021) 105741. <https://doi.org/10.1016/j.resconrec.2021.105741>.
- [15] F. Diaz, Y. Wang, R. Weyhe, B. Friedrich, Gas generation measurement and evaluation during mechanical processing and thermal treatment of spent Li-ion batteries, *Waste Manag.* 84 (2019) 102–111. <https://doi.org/10.1016/j.wasman.2018.11.029>.
- [16] R. Zhang, X. Shi, O.C. Esan, L. An, Organic Electrolytes Recycling From Spent Lithium-Ion Batteries, *Glob. Challenges*. (2022) 2200050. <https://doi.org/10.1002/gch2.202200050>.
- [17] S. Nowak, M. Winter, The role of sub- and supercritical CO₂ as “processing solvent” for the recycling and sample preparation of lithium ion battery electrolytes, *Molecules*. 22 (2017) 403. <https://doi.org/10.3390/molecules22030403>.

- [18] J. Neumann, M. Petranikova, M. Meeus, J.D. Gamarra, R. Younesi, M. Winter, S. Nowak, Recycling of Lithium-Ion Batteries — Current State of the Art , Circular Economy , and Next Generation Recycling, 2102917 (2022). <https://doi.org/10.1002/aenm.202102917>.
- [19] EUR-Lex, Directive 2006/66/EC of the European Parliament and of the Council of 6 September 2006 on batteries and accumulators and waste batteries and accumulators and repealing Directive 91/157/EEC, Off. J. Eur. Union. L 266 (2006) 1–14.
- [20] D.L. Thompson, J.M. Hartley, S.M. Lambert, M. Shiref, G.D.J. Harper, E. Kendrick, P. Anderson, K.S. Ryder, L. Gaines, A.P. Abbott, The importance of design in lithium ion battery recycling-a critical review, *Green Chem.* 22 (2020) 7585–7603. <https://doi.org/10.1039/d0gc02745f>.
- [21] G. Harper, R. Sommerville, E. Kendrick, L. Driscoll, P. Slater, R. Stolk, A. Walton, P. Christensen, O. Heidrich, S. Lambert, A. Abbott, K. Ryder, L. Gaines, P. Anderson, Recycling lithium-ion batteries from electric vehicles, *Nature*. 575 (2019) 75–86. <https://doi.org/10.1038/s41586-019-1682-5>.
- [22] M. Romare, L. Dahllöf, The Life Cycle Energy Consumption and Greenhouse Gas Emissions from Lithium-Ion Batteries A study with focus on Current Technology and batteries for light-duty vehicles., 2017. <http://www.ivl.se/download/18.5922281715bdaebede9559/1496046218976/C243+The+life+cycle+energy+consumption+and+CO2+emissions+from+lithium+ion+batteries+.pdf>.
- [23] E. Mossali, N. Picone, L. Gentilini, O. Rodríguez, J.M. Pérez, M. Colledani, Lithium-ion batteries towards circular economy: A literature review of opportunities and issues of recycling treatments, *J. Environ. Manage.* 264 (2020) 110500. <https://doi.org/10.1016/j.jenvman.2020.110500>.
- [24] J. Choi, P.J. Kim, A roadmap of battery separator development: Past and future, *Curr. Opin. Electrochem.* 31 (2022) 100858. <https://doi.org/10.1016/j.coelec.2021.100858>.
- [25] M. Li, C. Wang, Z. Chen, K. Xu, J. Lu, New Concepts in Electrolytes, *Chem. Rev.* 120 (2020) 6783–6819. <https://doi.org/10.1021/acs.chemrev.9b00531>.
- [26] Y. Horowitz, C. Schmidt, D. Yoon, L.M. Riegger, L. Katzenmeier, G.M. Bosch, M. Noked, Y. Ein-Eli, J. Janek, W.G. Zeier, C.E. Diesendruck, D. Golodnitsky, Between Liquid and All Solid: A Prospect on Electrolyte Future in Lithium-Ion Batteries for Electric Vehicles, *Energy Technol.* 8 (2020) 2000580. <https://doi.org/10.1002/ente.202000580>.
- [27] K. Xu, Li-ion battery electrolytes, *Nat. Energy.* 6 (2021) 763. <https://doi.org/10.1038/s41560-021-00841-6>.
- [28] K. Xu, Nonaqueous liquid electrolytes for lithium-based rechargeable batteries, *Chem. Rev.* 104 (2004) 4303–4417. <https://doi.org/10.1021/cr030203g>.
- [29] D. Hubble, D.E. Brown, Y. Zhao, C. Fang, J. Lau, B.D. McCloskey, G. Liu, Liquid electrolyte development for low-temperature lithium-ion batteries, *Energy Environ. Sci.* 15 (2022) 550–578. <https://doi.org/10.1039/d1ee01789f>.
- [30] K. Abe, Nonaqueous Electrolytes and Advances in Additives, (2014) 167–207. https://doi.org/10.1007/978-1-4939-0302-3_3.
- [31] European Commission, EU 1272/2008 – Classification, Labelling and Packaging of Substances and Mixtures, Med. Device Guidel. Regul. Handb. (2022) 261–295. https://doi.org/10.1007/978-3-030-91855-2_14.
- [32] C. Ekberg, M. Petranikova, Lithium Batteries Recycling, in: *Lithium Process Chem. Resour. Extr. Batter. Recycl.*, Elsevier Inc., 2015: pp. 233–267. <https://doi.org/10.1016/B978-0-12-801417-2.00007-4>.
- [33] D.M. Werner, T. Mütze, U.A. Peuker, Influence of Cell Opening Methods on Electrolyte Removal during Processing in Lithium-Ion Battery Recycling, *Met.* 2022, Vol. 12, Page 663. 12 (2022) 663. <https://doi.org/10.3390/MET12040663>.
- [34] D.M. Werner, T. Mütze, U.A. Peuker, Influence of Cell Opening Methods on Electrolyte

Removal during Processing in Lithium-Ion Battery Recycling, Metals (Basel). 12 (2022) 663. <https://doi.org/10.3390/met12040663>.

- [35] S. Bertilsson, F. Larsson, M. Furlani, I. Albinsson, B.E. Mellander, Lithium-ion battery electrolyte emissions analyzed by coupled thermogravimetric/Fourier-transform infrared spectroscopy, *J. Power Sources.* 365 (2017) 446–455. <https://doi.org/10.1016/j.jpowsour.2017.08.082>.
- [36] H. Yang, G. V. Zhuang, P.N. Ross, Thermal stability of LiPF₆ salt and Li-ion battery electrolytes containing LiPF₆, *J. Power Sources.* 161 (2006) 573–579. <https://doi.org/10.1016/j.jpowsour.2006.03.058>.
- [37] P. Andersson, P. Blomqvist, A. Lorén, F. Larsson, Using Fourier transform infrared spectroscopy to determine toxic gases in fires with lithium-ion batteries, *Fire Mater.* 40 (2016) 999–1015. <https://doi.org/10.1002/fam.2359>.
- [38] L.D. Kock, M.D.S. Lekgoathi, P.L. Crouse, B.M. Vilakazi, Solid state vibrational spectroscopy of anhydrous lithium hexafluorophosphate (LiPF₆), *J. Mol. Struct.* 1026 (2012) 145–149. <https://doi.org/10.1016/j.molstruc.2012.05.053>.
- [39] B. Ravdel, K.M. Abraham, R. Gitzendanner, J. DiCarlo, B. Lucht, C. Campion, Thermal stability of lithium-ion battery electrolytes, in: *J. Power Sources*, Elsevier, 2003: pp. 805–810. [https://doi.org/10.1016/S0378-7753\(03\)00257-X](https://doi.org/10.1016/S0378-7753(03)00257-X).
- [40] X.G. Teng, F.Q. Li, P.H. Ma, Q. Du Ren, S.Y. Li, Study on thermal decomposition of lithium hexafluorophosphate by TG-FT-IR coupling method, *Thermochim. Acta.* 436 (2005) 30–34. <https://doi.org/10.1016/j.tca.2005.07.004>.
- [41] J. Henschel, J.L. Schwarz, F. Glorius, M. Winter, S. Nowak, Further insights into structural diversity of phosphorus-based decomposition products in lithium ion battery electrolytes via liquid chromatographic techniques hyphenated to ion trap-time-of-flight mass spectrometry, *Anal. Chem.* 91 (2019) 3980–3988. <https://doi.org/10.1021/acs.analchem.8b05229>.
- [42] X. Mönnighoff, A. Friesen, B. Konersmann, F. Horsthemke, M. Grützke, M. Winter, S. Nowak, Supercritical carbon dioxide extraction of electrolyte from spent lithium ion batteries and its characterization by gas chromatography with chemical ionization, *J. Power Sources.* 352 (2017) 56–63. <https://doi.org/10.1016/j.jpowsour.2017.03.114>.
- [43] W. Weber, V. Kraft, M. Grützke, R. Wagner, M. Winter, S. Nowak, Identification of alkylated phosphates by gas chromatography-mass spectrometric investigations with different ionization principles of a thermally aged commercial lithium ion battery electrolyte, *J. Chromatogr. A.* 1394 (2015) 128–136. <https://doi.org/10.1016/j.chroma.2015.03.048>.
- [44] G. Harper, P.A. Anderson, E. Kendrick, W. Mrozik, P. Christensen, S. Lambert, D. Greenwood, P.K. Das, M. Ahmeid, Z. Milojevic, W. Du, D.J.L. Brett, P.R. Shearing, A. Rastegarpanah, R. Solkin, R. Sommerville, A. Zorin, J.L. Durham, A. Abbott, D. Thompson, N. Browning, L. Mehdi, M. Bahri, F. Schnaider-Tontini, D. Nicholls, C. Stallmeister, B. Friedrich, M. Sommerfeld, L.L. Driscoll, A. Jarvis, E.C. Giles, P.R. Slater, V. Echavarri-Bravo, G. Maddalena, L. Horsfall, L. Gaines, Q. Dai, S.J. Jethwa, A.L. Lipson, G.A. Leeke, T.D. Cowell, J.G. Farthing, G. Mariani, A. Smith, Z. Iqbal, R. Golmohammadzadeh, L. Sweeney, V. Goodship, Z. Li, J.S. Edge, L. Lander, V. Nguyen-Tien, R.J.R. Elliott, O. Heidrich, M. Slattery, D. Reed, J. Ahuja, A. Cavoski, R. Lee, E. Driscoll, J. Baker, P.B. Littlewood, I. Styles, S. Mahanty, F. Boons, Roadmap for a sustainable circular economy in lithium-ion and future battery technologies, *J. Phys. Energy.* 5 (2022) 021501. <https://doi.org/10.1088/2515-7655/acaa57>.
- [45] X. Zhong, W. Liu, J. Han, F. Jiao, W. Qin, T. Liu, C. Zhao, Pyrolysis and physical separation for the recovery of spent LiFePO₄ batteries, *Waste Manag.* 89 (2019) 83–93. <https://doi.org/10.1016/j.wasman.2019.03.068>.
- [46] B. Niu, Z. Xu, J. Xiao, Y. Qin, Recycling Hazardous and Valuable Electrolyte in Spent Lithium-Ion Batteries: Urgency, Progress, Challenge, and Viable Approach, *Chem. Rev.* 123 (2023) 8718–8735.

https://doi.org/10.1021/ACS.CHEMREV.3C00174/ASSET/IMAGES/LARGE/CR3C00174_0008.JPG.

- [47] F. Stehmann, C. Bradtmöller, S. Scholl, Separation of the Electrolyte—Thermal Drying, in: Sustain. Prod. Life Cycle Eng. Manag., Springer, 2018: pp. 139–153.
https://doi.org/10.1007/978-3-319-70572-9_8.
- [48] Umweltfreundliches Recycling von Lithium-Ionen-Batterien., (n.d.).
https://www.duesenfeld.com/index_de.html (accessed February 8, 2023).
- [49] R. Xu, S. Lei, T. Wang, C. Yi, W. Sun, Y. Yang, Lithium recovery and solvent reuse from electrolyte of spent lithium-ion battery, Waste Manag. 167 (2023) 135–140.
<https://doi.org/10.1016/J.WASMAN.2023.05.034>.
- [50] S. Lei, W. Sun, Y. Yang, Solvent extraction for recycling of spent lithium-ion batteries, Elsevier B.V., 2022. <https://doi.org/10.1016/j.jhazmat.2021.127654>.
- [51] K. He, Z.Y. Zhang, L. Alai, F.S. Zhang, A green process for exfoliating electrode materials and simultaneously extracting electrolyte from spent lithium-ion batteries, J. Hazard. Mater. 375 (2019) 43–51. <https://doi.org/10.1016/j.jhazmat.2019.03.120>.
- [52] Y. Zhu, Q. Ding, Y. Zhao, J. Ai, Y. Li, Y.C. Cao, Study on the process of harmless treatment of residual electrolyte in battery disassembly, Waste Manag. Res. 38 (2020) 1295–1300.
<https://doi.org/10.1177/0734242X20914752>.
- [53] P. Haas, S. Pfeifer, J. Müller, C. Bradtmöller, S. Scholl, Separation of the Electrolyte—Solvent Extraction, in: Sustain. Prod. Life Cycle Eng. Manag., Springer, 2018: pp. 155–176.
https://doi.org/10.1007/978-3-319-70572-9_9.
- [54] G. Shi, J. Wang, S. Zhang, J. Cheng, X. Shao, Z. Xu, X. Chen, B. Xin, Green regeneration and high-value utilization technology of the electrolyte from spent lithium-ion batteries, Sep. Purif. Technol. 335 (2024) 126144. <https://doi.org/10.1016/J.SEPPUR.2023.126144>.
- [55] H. Du, Y. Kang, C. Li, Y. Zhao, Y. Tian, J. Lu, Z. Chen, N. Gao, Z. Li, J. Wozny, T. Li, L. Wang, N. Tavajohi, F. Kang, B. Li, Recovery of lithium salt from spent lithium-ion battery by less polar solvent wash and water extraction, Carbon Neutralization. 2 (2023) 416–424.
<https://doi.org/10.1002/CNL2.73>.
- [56] S. Lee, Green chemistry and chemical engineering, Part. Technol. Appl. (2016) vii–viii.
<https://doi.org/10.1007/978-1-4939-9060-3>.
- [57] S.P. Nalawade, F. Picchioni, L.P.B.M. Janssen, Supercritical carbon dioxide as a green solvent for processing polymer melts: Processing aspects and applications, Prog. Polym. Sci. 31 (2006) 19–43. <https://doi.org/10.1016/j.progpolymsci.2005.08.002>.
- [58] Ž. Knez, C. Lütge, Product, Process and Plant Design Using Subcritical and Supercritical Fluids for Industrial Application, Prod. Process Plant Des. Using Subcritical Supercrit. Fluids Ind. Appl. (2023) 1–256. <https://doi.org/10.1007/978-3-031-34636-1/COVER>.
- [59] P. Raveendran, Y. Ikushima, S.L. Wallen, Polar attributes of supercritical carbon dioxide, Acc. Chem. Res. 38 (2005) 478–485. <https://doi.org/10.1021/ar040082m>.
- [60] M.D.L. de Castro, M. Valcárcel, M.T. Tena, Analytical Supercritical Fluid Extraction, Springer Berlin Heidelberg, 1994. <https://doi.org/10.1007/978-3-642-78673-0>.
- [61] F.P. Lucien, N.R. Foster, Solubilities of solid mixtures in supercritical carbon dioxide: A review, J. Supercrit. Fluids. 17 (2000) 111–134. [https://doi.org/10.1016/S0896-8446\(99\)00048-0](https://doi.org/10.1016/S0896-8446(99)00048-0).
- [62] K.D. Bartle, T. Boddington, A.A. Clifford, S.B. Hawthorne, The Effect of solubility on the kinetics of dynamic supercritical-fluid extraction, J. Supercrit. Fluids. 5 (1992) 207–212.
[https://doi.org/10.1016/0896-8446\(92\)90009-9](https://doi.org/10.1016/0896-8446(92)90009-9).
- [63] L.S. Daintree, A. Kordikowski, P. York, Separation processes for organic molecules using SCF Technologies, Adv. Drug Deliv. Rev. 60 (2008) 351–372.
<https://doi.org/10.1016/j.addr.2007.03.024>.

- [64] M. Grützke, V. Kraft, W. Weber, C. Wendt, A. Friesen, S. Klamor, M. Winter, S. Nowak, Supercritical carbon dioxide extraction of lithium-ion battery electrolytes, *J. Supercrit. Fluids.* 94 (2014) 216–222. <https://doi.org/10.1016/j.supflu.2014.07.014>.
- [65] M. Grützke, X. Mönnighoff, F. Horsthemke, V. Kraft, M. Winter, S. Nowak, Extraction of lithium-ion battery electrolytes with liquid and supercritical carbon dioxide and additional solvents, *RSC Adv.* 5 (2015) 43209–43217. <https://doi.org/10.1039/c5ra04451k>.
- [66] Y. Liu, D. Mu, R. Zheng, C. Dai, Supercritical CO₂ extraction of organic carbonate-based electrolytes of lithium-ion batteries, *RSC Adv.* 4 (2014) 54525–54531. <https://doi.org/10.1039/c4ra10530c>.
- [67] W.E. Org, Y. Liu, D. Mu, Y. Dai, Q. Ma, R. Zheng, C. Dai, Analysis on Extraction Behaviour of Lithium-ion Battery Electrolyte Solvents in Supercritical CO₂ by Gas Chromatography, *Int. J. Electrochem. Sci.* 11 (2016) 7594–7604. <https://doi.org/10.20964/2016.09.03>.
- [68] Y. Liu, D. Mu, R. Li, Q. Ma, R. Zheng, C. Dai, Purification and Characterization of Reclaimed Electrolytes from Spent Lithium-Ion Batteries, *J. Phys. Chem. C.* 121 (2017) 4181–4187. <https://doi.org/10.1021/acs.jpcc.6b12970>.
- [69] D. Mu, Y. Liu, R. Li, Q. Ma, C. Dai, Transcritical CO₂ extraction of electrolytes for lithium-ion batteries: Optimization of the recycling process and quality-quantity variation, *New J. Chem.* 41 (2017) 7177–7185. <https://doi.org/10.1039/c7nj00771j>.
- [70] S. Sloop, L. Crandon, M. Allen, K. Koetje, L. Reed, L. Gaines, W. Sirisaksoontorn, M. Lerner, A direct recycling case study from a lithium-ion battery recall, *Sustain. Mater. Technol.* 25 (2020) e00152. <https://doi.org/10.1016/j.susmat.2020.e00152>.
- [71] M. Altarsha, F. Ingrosso, M.F. Ruiz-Lopez, A New Glimpse into the CO₂-Philicity of Carbonyl Compounds, *ChemPhysChem.* 13 (2012) 3397–3403. <https://doi.org/10.1002/cphc.201200135>.
- [72] F. Ingrosso, M.F. Ruiz-López, Modeling Solvation in Supercritical CO₂, *ChemPhysChem.* 18 (2017) 2560–2572. <https://doi.org/10.1002/cphc.201700434>.
- [73] D. Kajiya, M. Imanishi, K.I. Saitow, Solvation of Esters and Ketones in Supercritical CO₂, *J. Phys. Chem. B.* 120 (2016) 785–792. <https://doi.org/10.1021/acs.jpcb.5b11740>.
- [74] H.J. Vandenburg, A.A. Clifford, K.D. Bartle, J. Carroll, I. Newton, L.M. Garden, J.R. Dean, C.T. Costley, Analytical extraction of additives from polymers, *Analyst.* 122 (1997) 101R–116R. <https://doi.org/10.1039/a704052k>.
- [75] Y. Fu, J. Schuster, M. Petranikova, B. Ebin, Innovative recycling of organic binders from electric vehicle lithium-ion batteries by supercritical carbon dioxide extraction, *Resour. Conserv. Recycl.* 172 (2021) 105666. <https://doi.org/10.1016/j.resconrec.2021.105666>.
- [76] S. Shimizu, S. Abbott, How Entrainers Enhance Solubility in Supercritical Carbon Dioxide, *J. Phys. Chem. B.* 120 (2016) 3713–3723. <https://doi.org/10.1021/acs.jpcb.6b01380>.
- [77] J. Chrastil, Solubility of solids and liquids in supercritical gases, *J. Phys. Chem.* 86 (1982) 3016–3021. https://doi.org/10.1021/J100212A041/ASSET/J100212A041.FP.PNG_V03.
- [78] J.M. Del Valle, F.A. Urrego, Free solute content and solute-matrix interactions affect apparent solubility and apparent solute content in supercritical CO₂ extractions. A hypothesis paper, *J. Supercrit. Fluids.* 66 (2012) 157–175. <https://doi.org/10.1016/J.SUPFLU.2011.10.006>.
- [79] Z. Huang, X. han Shi, W. juan Jiang, Theoretical models for supercritical fluid extraction, *J. Chromatogr. A.* 1250 (2012) 2–26. <https://doi.org/10.1016/J.CHROMA.2012.04.032>.
- [80] H. Sovová, Mathematical model for supercritical fluid extraction of natural products and extraction curve evaluation, *J. Supercrit. Fluids.* 33 (2005) 35–52. <https://doi.org/10.1016/J.SUPFLU.2004.03.005>.
- [81] S.F. Lux, I.T. Lucas, E. Pollak, S. Passerini, M. Winter, R. Kostecki, The mechanism of HF formation in LiPF₆ based organic carbonate electrolytes, *Electrochim. Commun.* 14 (2012) 47–50. <https://doi.org/10.1016/j.elecom.2011.10.026>.

- [82] V. Kraft, M. Grützke, W. Weber, M. Winter, S. Nowak, Ion chromatography electrospray ionization mass spectrometry method development and investigation of lithium hexafluorophosphate-based organic electrolytes and their thermal decomposition products, *J. Chromatogr. A.* 1354 (2014) 92–100. <https://doi.org/10.1016/j.chroma.2014.05.066>.
- [83] NIST Chemistry WebBook - Thermophysical Properties of Fluid Systems, (n.d.). <https://webbook.nist.gov/chemistry/fluid/> (accessed October 3, 2024).
- [84] C. Peschel, S. van Wickeren, Y. Preibisch, V. Naber, D. Werner, L. Frankenstein, F. Horsthemke, U. Peuker, M. Winter, S. Nowak, Comprehensive Characterization of Shredded Lithium-Ion Battery Recycling Material, *Chem. – A Eur. J.* 28 (2022) e202200485. <https://doi.org/10.1002/CHEM.202200485>.
- [85] H. Bohets, B.J. Van Der Veken, On the conformational behavior of dimethyl carbonate, *Phys. Chem. Chem. Phys.* 1 (1999) 1817–1826. <https://doi.org/10.1039/a901046g>.
- [86] A.K. Das, K. Sunanda, B.N. Rajasekhar, Electronic and vibrational spectroscopy of ethyl methyl carbonate: A comparative experimental and theoretical study, *J. Quant. Spectrosc. Radiat. Transf.* 272 (2021) 107789. <https://doi.org/10.1016/j.jqsrt.2021.107789>.
- [87] B. Fortunato, P. Mirone, G. Fini, Infrared and Raman spectra and vibrational assignment of ethylene carbonate, *Spectrochim. Acta Part A Mol. Spectrosc.* 27 (1971) 1917–1927. [https://doi.org/10.1016/0584-8539\(71\)80245-3](https://doi.org/10.1016/0584-8539(71)80245-3).
- [88] Z. Liao, S. Zhang, Y. Zhao, Z. Qiu, K. Li, D. Han, G. Zhang, T.G. Habetler, Experimental evaluation of thermolysis-driven gas emissions from LiPF₆-carbonate electrolyte used in lithium-ion batteries, *J. Energy Chem.* 49 (2020) 124–135. <https://doi.org/10.1016/j.jecchem.2020.01.030>.
- [89] S.J. Jethwa, L.A. Román-Ramírez, P.A. Anderson, G.A. Leeke, Vapor Equilibrium Data for the Binary Mixtures of Dimethyl Carbonate and Ethyl Methyl Carbonate in Compressed Carbon Dioxide, *Int. J. Thermophys.* 44 (2023) 1–13. <https://doi.org/10.1007/S10765-023-03186-2/FIGURES/4>.
- [90] M.H. Lee, J.H. Yim, J.W. Kang, J.S. Lim, Measurement of VLE data of carbon dioxide + dimethyl carbonate system for the direct synthesis of dimethyl carbonate using supercritical CO₂ and methanol, *Fluid Phase Equilib.* 318 (2012) 77–82. <https://doi.org/10.1016/J.FLUID.2012.01.020>.
- [91] R. Piñero, J. García, M. Sokolova, M.J. Cocero, Modelling of the phase behaviour for the direct synthesis of dimethyl carbonate from CO₂ and methanol at supercritical or near critical conditions, *J. Chem. Thermodyn.* 39 (2007) 536–549. <https://doi.org/10.1016/J.JCT.2006.09.009>.
- [92] S. Camy, J.S. Pic, E. Badens, J.S. Condoret, Fluid phase equilibria of the reacting mixture in the dimethyl carbonate synthesis from supercritical CO₂, *J. Supercrit. Fluids.* 25 (2003) 19–32. [https://doi.org/10.1016/S0896-8446\(02\)00087-6](https://doi.org/10.1016/S0896-8446(02)00087-6).
- [93] F. Bustamante, A.F. Orrego, S. Villegas, A.L. Villa, Modeling of chemical equilibrium and gas phase behavior for the direct synthesis of dimethyl carbonate from CO₂ and methanol, *Ind. Eng. Chem. Res.* 51 (2012) 8945–8956. https://doi.org/10.1021/IE300017R/SUPPL_FILE/IE300017R_SI_001.PDF.
- [94] R.P. Ciccolini, A.C. Madlinger, S.A. Rogers, J.W. Tester, Vapor - Liquid equilibrium data and predictive correlations for the carbon dioxide - Dimethyl carbonate binary mixture, *J. Chem. Eng. Data.* 55 (2010) 2673–2681. https://doi.org/10.1021/JE900948N/SUPPL_FILE/JE900948N_SI_001.PDF.
- [95] M. Anouti, Y. Rodrigue Dougassa, C. Tessier, L. El Ouatani, J. Jacquemin, Low pressure carbon dioxide solubility in pure electrolyte solvents for lithium-ion batteries as a function of temperature. Measurement and prediction, (2012). <https://doi.org/10.1016/j.jct.2012.01.027>.
- [96] Z. Piao, R. Gao, Y. Liu, G. Zhou, H.M. Cheng, A Review on Regulating Li⁺ Solvation Structures in Carbonate Electrolytes for Lithium Metal Batteries, *Adv. Mater.* 35 (2023)

2206009. <https://doi.org/10.1002/ADMA.202206009>.
- [97] C.H. Cheng, Y.P. Chen, Vapor–liquid equilibria of carbon dioxide with isopropyl acetate, diethyl carbonate and ethyl butyrate at elevated pressures, *Fluid Phase Equilib.* 234 (2005) 77–83. <https://doi.org/10.1016/J.FLUID.2005.05.018>.
- [98] H. Sovová, Apparent Solubility of Natural Products Extracted with Near-Critical Carbon Dioxide, *Am. J. Anal. Chem.* 2012 (2012) 958–965. <https://doi.org/10.4236/AJAC.2012.312A127>.
- [99] R.B. Gupta, J.J. Shim, Solubility in supercritical carbon dioxide, *Solubility Supercrit. Carbon Dioxide.* (2006) 1–909. <https://doi.org/10.1201/9781420005998/SOLUBILITY-SUPERCritical-CARBON-DIOXIDE-RAM-GUPTA-JAE-JIN-SHIM>.

